Optical manifestations and collisions of Action Potentials in nerves

DISSERTATION

zur Erlangung des akademischen Grades eines
Doktors der Naturwissenschaften (Dr. rer. nat.)

vorgelegt von

MORITZ SCHLÖTTER

an der

UNIVERSITÄT KONSTANZ
Fachbereich Physik

Konstanz, 2020

Tag der mündlichen Prüfung: 20.11.2020
1. Referent: Prof. Dr. Georg Maret
2. Referent: apl. Prof. Dr. Christoph Kleineidam

Zusammenfassung

Diese Arbeit befasst sich mit elektrischen und optischen Messungen neuronaler Aktivität. Der erste Teil meiner Arbeit beschreibt extrazelluläre elektrische Messungen an kollidierenden Aktionspotentialen (APs) in Regenwurmnerven. Die elektromagnetische Wechselwirkung (ephaptische Kopplung) zwischen APs und ihrer Umgebung ist besonders stark, wenn APs entstehen oder verschwinden (ephaptische Entladung). Ich zeige, dass APs sich auslöschen, wenn sie kollidieren. Dadurch bietet sich eine bisher unentdeckte Möglichkeit, die ephaptische Entladung zu messen. Diese Messungen zeigen, dass die ephaptische Entladung im allgemein akzeptierten Hodgkin-Huxley-Modell um eine ganze Größenordnung unterschätzt wird, während das sehr einfache aber vergleichsweise unbekannte Tasaki-Cable-Modell den Effekt genau wiedergibt. Die Auswirkung auf benachbarte Zellen hängt von deren Position und Orientierung sowie vom Zeitpunkt der APs ab und kann sowohl anregend (exzitatorisch) als auch unterdrückend (inhibitorisch) sein. Ich stelle die Hypothese auf, dass starke ephaptische Entladungen eine grundlegende Eigenschaft von APs und damit eine wesentliche Komponente der interzellulären Kommunikation sind, insbesondere an Synapsen. Außerdem ist zu erwarten, dass wiederholte Entladungen auch morphologische Veränderungen der Zellen bewirken. Diese Prozesse sind jedoch durch elektrische Aufzeichnungen nicht festzustellen.

Im zweiten Teil meiner Arbeit entwickle ich eine neue optische Methode, mit der solche nicht elektrischen Prozesse beobachtet werden können. APs bewirken strukturelle Änderungen und Deformationen und verursachen dadurch ein optisches Signal, das *fast Intrinsic Optical Signal* (fIOS). Das fIOS wird normalerweise entweder in der Depolarisation von transmittiertem Licht oder in Fluktuationen des gestreuten Lichts detektiert. Zunächst untersuche ich die Depolarisation von transmittiertem Licht an elektrisch stimulierten Hummernerven mit einer außerordentlich empfindlichen Methode. Ein fIOS konnte nur unter sehr kleinen Streuwinkeln ($\vartheta > 0.3°$) detektiert werden, jedoch nie in ungestreutem Licht ($\vartheta < 0.2°$). Dieser feine Unterschied wurde mit den bisherigen Messsystemen nicht festgestellt und widerspricht der gängigen Interpretation, dass das fIOS durch eine Änderung der Doppelbrechung entsteht.

Die finalen optischen Experimente nutzen diese Erkenntnis in Kombination mit einem kürzlich von F. Amblard vorgeschlagenen Konzept. Fluktuationen des gestreuten Lichts werden nach dem Prinzip der Vielfachstreuung verstärkt, indem die Probe in einem weißen Hohlraum eingebettet wird. Ich nenne diese Methode *Cavity Amplified Speckle Spectroscopy* (CASS). Mehrere Prototypen wurden entworfen, optimiert und in den elektrophysiologischen Aufbau integriert. Mit CASS kann sogar das fIOS eines einzelnen myelinisierten Axons im trüben Bauchmark des Regenwurms detektiert werden. Zusätzlich zeigt sich ein langsamerer Prozess neuronaler Aktivität, welchen ich *slow* IOS (sIOS) nenne. Ein Zusammenhang zwischen dem sIOS und APs ist klar erkennbar, der Ursprung des sIOS ist jedoch noch nicht geklärt.

Abstract

This work is concerned with electrical and optical measurements of neural activity. The first part of my work describes extracellular electric measurements of colliding Action Potentials (APs) in nerve chords from earthworms. The electromagnetic interaction (ephaptic coupling) between APs and their surroundings is particularly strong when APs are generated or annihilate (ephaptic discharge). I show that APs annihilate when they collide. This offers a previously undiscovered way to measure the ephaptic discharge. These measurements show that the well accepted Hodgkin-Huxley model underestimates the ephaptic discharge by one order of magnitude, while the very simple but comparably unpopular Tasaki-Cable model precisely reproduces the effect. The effect on neighboring cells depends on their position and orientation, as well as the timing of the APs, and can be excitatory or inhibitory. I make the hypothesis that a strong ephaptic discharge is a universal property of APs and therefore a major component of intercellular communication, especially at synapses. It is also to be expected that repeated discharges will cause morphological changes in the cells. However, these processes cannot be observed by electrical recordings.

In the second part of my work, I am developing a new optical method with which such non-electrical processes can be observed. APs cause structural changes and deformations and thereby cause an optical signal, the *fast Intrinsic Optical Signal* (fIOS). The fIOS is usually detected either in the depolarization of transmitted light or in fluctuations of the scattered light. First, I examine the depolarization of transmitted light of electrically stimulated nerve lobster with an extremely sensitive method. An fIOS could only be detected under very small scattering angles ($\vartheta > 0.3°$), but never in unscattered light ($\vartheta < 0.2°$). This subtle difference was not resolved by previous measurement systems and contradicts the common interpretation that the fIOS is caused by a change in the birefringence.

The final optical experiments use this knowledge in combination with a concept recently proposed by F. Amblard. Fluctuations in the scattered light are amplified according to the principle of multiple scattering by embedding the sample in a white cavity. I call this method *Cavity Amplified Speckle Spectroscopy* (CASS). Several prototypes were designed, optimized and integrated into the electrophysiological setup. CASS can even detect the fIOS of a single myelinated axon in the earthworm's turbid ventral nerve chord. In addition, a slower process of neural activity is revealed, which I call *slow* IOS (sIOS). A connection between the sIOS and APs is clearly recognizable, but the origin of the sIOS has not yet been clarified.

Acknowledgments

I want to thank Georg Maret for almost a decade of continuous support and inspiration. He gave me the opportunity to spend years with high-risk experiments, aiming for more than mediocre results. In the last year of this enduring process, we were eventually rewarded. I owe it to his thoughtful leadership, his assistance and strokes of genius, that our approaches were lead to success. Finishing my thesis took longer than expected. I hope these final results compensates for straining his patience, at least to some extent.

I want to thank all colleagues and friends that helped and supported me during this project, but I can only list some of them here. Wolfgang Scheffer provided invaluable support for me from the beginning of my diploma to subsequent work on my thesis. Geoffroy Aubry helped in difficult situations and collaborated with the design and characterization of the optical cavity. Peter Keim has been a constant motivator, I always enjoyed his painfully intelligent criticism. Further, I want to thank Markus Belau, Richard Rau, Herbert Kaiser and Lukas Siedentop, and the whole Maret Group for countless discussions and a great time. I am glad to have met so many bright minds that became close friends, and to learn about light, live and cool experiments.

A special thank is addressed to the biologists that sacrificed quite some time to understand my experimental challenges and who taught me how to overcome those. I thank Gerardo Alvarez and Luc Stoppini for providing insights and equipment to work with living tissue. In discussions with Mahlon Kriebel, I learned crucial tricks to perform electrophysiology.

The final results are the fruit of an intense collaboration with Christoph Kleineidam and Georg Raiser. For many years, they helped to build a bridge between physics and biology. Their complementary ideas and imense knowhow have been absolutely essential. Hopefully the outcome of this longsome process is satisfactory for them. In addition, I want to thank Christoph Kleineidam for his contributions as a referee. His friendship and keen scientific attitude have been fundamental for my work and life as a scientist.

I am deeply thankful to my wife Kristina. While I was absent struggling with seemingly absurd problems she cut back on her own interests to care for our children and to support my work. Without her commitment, this would not have been possible.

Contents

1 Introduction

Neuronal tissue controls the life functions and behavioral reactions of all higher organisms, including mammals. Most of this function is attributed to a network of neurons. Neurons can sense input, transmit signals and thereby communicate with one another or other cells like muscles. By doing so, a network of neurons is capable of computing information [123]. A large network, like a human brain, allows consciousness to enter an otherwise seemingly mindless world [52]. Centuries of scientific effort provides us with fragmented insights into these processes. Despite being inconclusive, these insights are constantly driving scientific, medical and philosophical progress. In my thesis, I aim to contribute to this progress with a novel approach of electric recordings, and by employing a very recently proposed method of optical spectroscopy.

Biological cells are separated from the outside world by a thin membrane. The membrane of neurons has a special function: it is excitable. Normally it is in a resting state, but it can rapidly switch to an excited state. This transition can be triggered by thermal, electrical, chemical or mechanical stimulation, and the transition also influences all of these properties [59, 86, 161, 164, 182, 185]. Neurons transmit pulses of excitation along their axons, these pulses are called Action Potentials (APs). Some axons end very close to neighboring cells, these connections are called synapses. At some synapses the arrival of a pre-synaptic AP excites the post-synaptic cell, while other synapses inhibit the activity of the post-synaptic cell [51].

At the current state of knowledge, this interaction of APs in neuronal networks is thought to be the core of information processing in animals. However, our understanding of excitation, as well as cell-to-cell interaction, is rather fragmented. The transmission of APs along an axon is usually described with an electric cable model, consequently the AP is called an electric pulse. On the other hand, the cell-to-cell communication across synapses is described with a chemical mechanism. So called neurotransmitters are released from the pre-synaptic membrane and affect the post-synaptic membrane. There are various excitatory and inhibitory species of neurotransmitters [107, 178].

Besides the textbook mechanisms of Neurotransmitters, there is another kind of cell-to-cell interaction. Nerve fibers are often close to each other and not perfectly shielded. Thus, a direct electric cross-talk which is called ephaptic coupling must occur [12, 103]. APs create an extracellular electric field in their surroundings, and the spatial inhomogeneities of this field influence neighboring cells [8]. The strength and physiological function of ephaptic coupling may not be clear, but its existence is beyond any doubt. In 1942, Angelique Arvanitaki observed ephaptic coupling and concluded that the generation and annihilation of APs can cause a strong ephaptic discharge and that its effect depends on the geometry of the cells. (e.g. at the end of an axon, a synapse or an artificially blocked region of a nerve) [12]. When two APs propagate towards each other and collide, they also annihilate and discharge [180]. I performed AP collision experiments to study the electric properties of annihilating APs. These experiments provide a unique way of measuring the extracellular electric field with a high spatial resolution. Thereby giving access to the ephaptic discharge of APs, which so far has not been observed otherwise.

The experimental results presented in Chapter 4 challenge the well accepted Hodgkin Huxley model, while supporting a stunningly simple model which was proposed by Tasaki in 2002[184, 191]. I formulate a hypothesis similar to Arvanitaki, and demonstrate that it has the potential to explain various phenomena of cell-to-cell interactions with classical electrodynamics.

Our understanding of neuronal activity is almost entirely based on electric recordings, but neuronal activity is more than a change in the electro-chemical properties of the membrane. Little is known about these non-electric processes because they cannot be detected by electrodes. However, some processes can be observed based on changes in the optical properties. Studying these non-electric changes bears the possibility to provide crucial information about neuronal activity, the underlying mechanisms of excitation and the interplay between electric and non-electric processes. The minute optical changes that accompany APs are called the fast Intrinsic Optical Signal (fIOS) [63, 118, 186, 192]. While neurons of vertebrates are wrapped in layers of fatty cells (myelin) and are therefore hidden in turbidity, neurons of most invertebrates are unmyelinated and were therefore used in previous studies that reported an fIOS.

The experiments in Chapter 5 narrow down the origin of the fIOS by using Lobster neurons. Based on these findings, a novel method to observe the fIOS is developed in Chapter 6. The measurement principle is based on multiple scattering of light which enables an outstandingly sensitive dynamic optical spectroscopy [124, 127]. A progression of this concept has very recently been proposed by Francois Amblard, which I refer to as Cavity Amplified Speckle Spectroscopy (CASS) [75]. The optical signal exhibits novel features of neuronal activity that are not visible in electric recordings.

I report the fIOS and other non-electric signatures of neuronal activity even from single axons and through turbid myelinated tissue.

2 Theory of Light

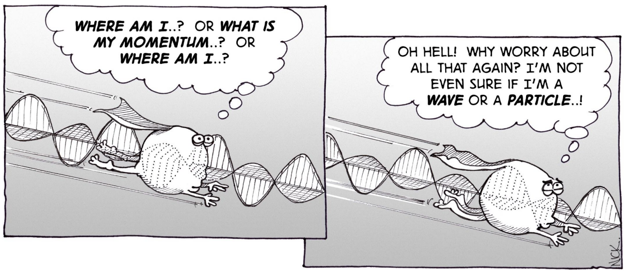

[109]

2.1 Introduction

The experiments presented in Chapter 5 and 6 describe optical changes of nervous tissue. The Intrinsic Optical Signal (IOS) is detected in scattered coherent laser light. In this chapter the theoretical background of the optical experiments is explained. The theory of light scattering is presented on the basis of [205], other notable textbooks are [21, 30, 166]. The theory of multiple scattering is not in textbooks, but is described e.g. in [124, 127, 205].

2.2 Light Scattering

Light is detected as single photons (like discrete particles). However, the transport of these photons is described by an electric field wave. The probability to detect a photon is proportional to the intensity

$$I = \langle E(t)^2 \rangle \ , \tag{2.1}$$

which is the time average of the squared electric field. Let us assume that the incoming light is a monochromatic plane wave with the frequency ω. Its electric field E_{in} at position r and time t is then

$$E_{in}(\mathbf{r}, t) = E_0 e^{i(\mathbf{k}_0 \mathbf{r} - \omega t)} \ , \tag{2.2}$$

with the wavevector $\mathbf{k}$ denoting the direction of propagation. The absolute value of $\mathbf{k}$ in a medium with refractive index n is

$$k = |\mathbf{k}| = \frac{\omega}{c} = \frac{2\pi n}{\lambda_0} \ , \tag{2.3}$$

where λ_0 is the wavelength in vacuum. The real index $n = c/v$ is the ratio between the speed of light in vacuum c and the speed of light inside the medium v. The index can be complex $\underline{n}$ to account for absorption. Spatial fluctuations of the refractive index $n(\mathbf{r})$ are the origin of light scattering. Anisotropic materials give rise to birefringence, then the index $\mathbf{n}$ is a tensor.

2.2.1 Scattering and Absorption Length

When light is transmitted thought a medium, it can be scattered or absorbed. The interaction coefficients and corresponding lengths will be introduced assuming a sample of uniformly distributed identical scatterers. The probability for a photon to be absorbed is described by the absorption cross section

$$\sigma_a = \frac{P_a}{I_0} , \tag{2.4}$$

with the incident intensity I_0 and absorbed power per particle P_a. The absorption coefficient

$$\mu_a = \rho \sigma_a , \tag{2.5}$$

with the number density ρ of absorbing particles [48], adds a complex component to the optical index

$$\underline{n} = n - \tfrac{i}{2k_0} \mu_a . \tag{2.6}$$

The inverse of μ_a is the absorption length

$$l_a = \frac{1}{\mu_a} . \tag{2.7}$$

The incoming intensity I_0 is diminished to

$$I = I_0 \exp(-\mu_a s) \tag{2.8}$$

along its path of length s through the sample. The scattering cross section σ_s, coefficient μ_s and length l_s

$$\sigma_s = \frac{P_s}{I_0} , \quad \mu_s = \rho \sigma_s \quad \text{and} \quad l_s = \frac{1}{\mu_s} \tag{2.9}$$

are introduced similarly to the absorption formalism. The scattering length l_s is the mean free path of a photon traveling through the sample.

In total, the incident beam is diminished by scattering and absorption. The transmitted intensity of the beam

$$I = I_0 \exp(-(\mu_a + \mu_s) s) . \tag{2.10}$$

decreases exponentially with the sample size s and the sum of scattering coefficient μ_s and absorption coefficient μ_a.

2.2.2 Static Scattering

The scattering theory is introduced with regard to individual scattering particles. Single scattering is assumed ($l_s \gg s$). Interaction of the incident radiation with a scattering particle of size a is classified based on the size parameter ka. The concepts introduced here follow the more complete presentations found in [21, 95, 205].

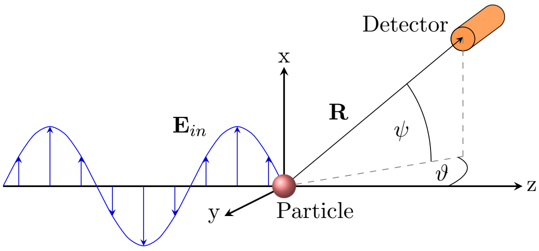

Figure 2.1: A linear polarized wave encounters a scatterer. The detector is located at $\mathbf{R}$. The field $\mathbf{E}_{in}$ defines the scattering plane perpendicular to $\mathbf{E}_{in}$ (here the y-z plane), where ϑ denotes the in-plane scattering angle and ψ the out-of-plane angle.

Figure 2.2: Angle resolved intensity of scattered light from a very small particle. In VV geometry the polarization of the incident and scattered light are perpendicular to the scattering plane ($\psi = 0$) and the denoted scattering angle is ϑ. In HH geometry both polarizations are in plane ($\vartheta = 0$) and the scattering angle is ψ. Unpolarized scattering is the average of all incoming polarizations.

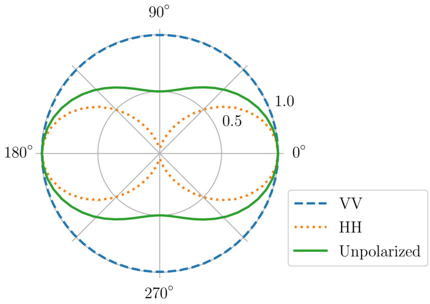

Rayleigh Regime

Rayleigh scattering describes the interaction of light with a very small particle of radius a and volume $V = \frac{4}{3}\pi a^3$, where ($ka \ll 1$). The incoming electric field E_0 (equation 2.2) creates a homogeneous oscillating dipole moment in the volume V. The strength of the dipole is given through its relative permittivity[1] $\epsilon_r = n^2$. This oscillating dipole radiates a field of amplitude

$$E_s(R, \psi, t) = -\frac{k^2}{4\pi} \frac{E_{in}(\mathbf{r}, t)}{R} (\epsilon_r - 1) V \cos\psi \ , \tag{2.11}$$

where ψ is the angle between the plane perpendicular to the electric field vector and the direction of observation [95] (see figure 2.1). Capital R denotes the distance between observer and particle. For linear polarized incoming light, the emitted intensity

$$I_s(\mathbf{R}) = I_s(R, \psi) = \langle E_s(R, \psi, t)^2 \rangle \quad \propto \quad \cos^2(\psi)\, k^4\, a^6 \tag{2.12}$$

strongly depends on a and k but it is also a function of ψ (see figure 2.2).

---

[1] Magnetic effects are neglected

Rayleigh-Debye-Gans Regime

The scattering from small particles can be extended to larger particles of random shape, if the phase shift of the field inside the particle, with respect to the external field, can be neglected. This condition is fulfilled when

$$ka(n-1) \ll 1\,, \tag{2.13}$$

where a is the long half axis of an anisotropic particle or the radius of a sphere. Then the amplitude of the scattered field at position $\mathbf{R}$ is the coherent sum of non-interacting Rayleigh elements

$$E_s(\mathbf{R},t) = \int_V dE_s(\mathbf{R},t)\,. \tag{2.14}$$

In a more general scattering formalism this approach is known as the first Born approximation. The individual path length difference to the detector

$$\Delta r = \frac{\mathbf{k}_0\mathbf{r} - \mathbf{k}_s\mathbf{r}}{k} \tag{2.15}$$

causes a corresponding phase shift $\Delta\phi$. With the definition of the scattering vector (see figure 2.3, left)

$$\mathbf{q} = \mathbf{k}_0 - \mathbf{k}_s \quad \text{and} \quad |\mathbf{q}| = |\mathbf{k}_0 - \mathbf{k}_s| = \frac{4\pi n}{\lambda}\sin\left(\frac{\vartheta}{2}\right)\,, \tag{2.16}$$

the phase shift can be expressed as

$$\Delta\phi = -\mathbf{q}\mathbf{r}\,. \tag{2.17}$$

With equation 2.17, the scattered field (eq. 2.14) is expressed as

$$E(\mathbf{R}) = -\frac{E_{in}}{R}\underbrace{\int_V \frac{k^2}{4\pi}(\epsilon_r(r)-1)e^{-i\mathbf{q}\mathbf{r}}d^3r}_{b(\mathbf{q})}\,, \tag{2.18}$$

where b is the scattering length, a value proportional to the Fourier transform of spatial inhomogeneities of the dielectric constant. The form factor,

$$P(\mathbf{q}) = \frac{\langle|b(\mathbf{q})|^2\rangle}{\langle|b(0)|^2\rangle}\,, \tag{2.19}$$

is the normalized average scattering intensity. It is a measure of the particles size.

Dispersion of Particles

In a ensemble of N particles, the scattered fields add up at the detector. Similar to the extension of point dipoles to small particles (eq. 2.18), the coherent sum

$$E_s(\mathbf{R},t) = -\frac{E_{in}}{R}\sum_{j=1}^{N} e^{-i\mathbf{q}\mathbf{r}_j}b_j(\mathbf{q}) \tag{2.20}$$

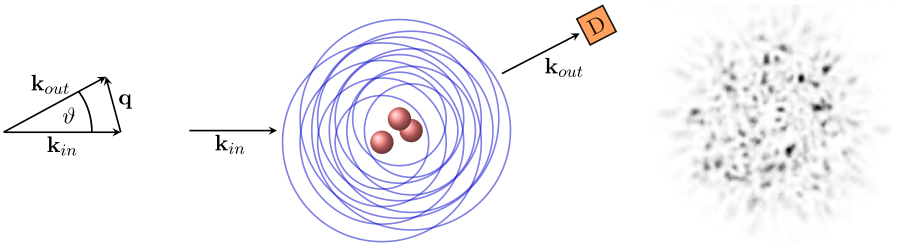

Figure 2.3: (left) The scattering vector $\mathbf{q}$ is defined as the difference between the incoming $\mathbf{k}_{in}$ and the detected $\mathbf{k}_{out}$ pointing vector. (middle) Interference pattern created by three scattering points. The scattered photons with $\mathbf{k} \parallel \mathbf{k}_{out}$ arrive at the detector (D). The random positions of scattering particles leads to a random distribution of constructive and destructive interference, called a speckle pattern. (right) Photograph of a speckle pattern.

of N particles at positions r_j is calculated. If pre-factors are neglected, the detected intensity is

$$\langle I_s(\mathbf{q})\rangle = \sum_{j=1}^{N}\sum_{k=1}^{N}\langle b_j(\mathbf{q})b_k^{\star}(\mathbf{q})e^{-iq(\mathbf{R}_j-\mathbf{R}_k)}\rangle \ . \tag{2.21}$$

An ensemble of spherical or unaligned particles is isotropic. If the particles are all identical, and the ensemble is isotropic the scattering length is $b_j(\mathbf{q}) = b(q)$. With the definition 2.19 the detected intensity from equation 2.21 can be written as

$$\langle I_s(q)\rangle = b^2(0)P(q)\sum_{j=1}^{N}\sum_{k=1}^{N}\langle e^{-iq(\mathbf{R}_j-\mathbf{R}_k)}\rangle \tag{2.22}$$

$$= Nb^2(0)P(q)S(q) \tag{2.23}$$

Here, $S(q)$ is the structure factor, accounting for spatial correlations between the particles. If the structure is periodic in space, the structure factor will recite the periodicity in $\mathbf{q}$-space: The scattering pattern of a crystal contains sharp ordered peaks (Bragg Peaks). In random media, the random positions generate a grainy far field pattern called a speckle (see fig 2.3, right).

Speckle imaging is a key method in this thesis. For this purpose an estimation of the size of one speckle spot is desired. The largest variation of the phase in equation 2.22 is determined by the particles j, k with the greatest distance to each other. The maximal distance is given by the size of the scattering volume L_V. Therefore, the variation of the phase is given by

$$\Delta\phi = \Delta q L_V \ . \tag{2.24}$$

The correlation is lost when $\Delta\phi \approx 2\pi$. Using the definition of the scattering vector (eq. 2.16), the angular spread $\Delta\vartheta$ of one speckle spot can be estimated to

$$\Delta\vartheta \approx \frac{\Delta q}{k} = \frac{\lambda}{L_V} \ . \tag{2.25}$$

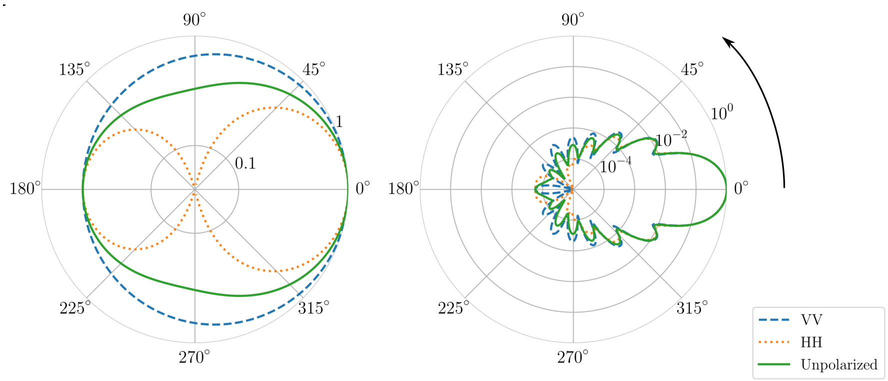

Figure 2.4: Mie scattering formfactor for large (left $x = 1$) and very large (right $x = 10$) particles. The scattering angle ϑ is indicated by the arc. Forward scattering increases drastically with increasing size parameter x.

Mie scattering

Scattering from particles comparable or larger than the wavelength requires a more uphill analytical treatment. For spheres of radius a, the important dimension is the size parameter $x = ka$. The general problem

$$\mathbf{E}(\mathbf{R}) = \tfrac{1}{R} \begin{pmatrix} \underline{S}_2 & \underline{S}_3 \\ \underline{S}_4 & \underline{S}_1 \end{pmatrix} \mathbf{E}_{in} \tag{2.26}$$

is expressed using complex scattering amplitudes $\underline{S}(\vartheta, \psi, x, \underline{n})$[95]. At the particle surface, the solution of the Maxwell equations for the electric field is expressed as an infinite sum of vector spherical harmonics. For spherical objects, the non-diagonal terms vanish $\underline{S}_3 = \underline{S}_4 = 0$. There are different numeric algorithms to calculate the Mie solution, many are based on Bohren and Huffman [25]. In this thesis the calculation of scattering functions is performed using the python package *miepython*[154] which is based on the algorithm provided by Wiscombe [201]. The solutions are heavily angle dependent, with increasing particle size, the forward scattering dominates the form factor more and more (see figure 2.4).

2.2.3 Dynamic Scattering

The far field that arrives at the detector is given in equation 2.21. It depends on the position $\mathbf{R}_j$ of each particle. Any movement of particles changes the phase (equation 2.17) and therefore the detected intensity. The resulting fluctuations of the speckle provide valuable information about the dynamics in the sample. In order to analyze these fluctuations, the autocorrelation function is calculated. The field autocorrelation function

$$g_1(\tau) = \frac{\langle E(t)E(t+\tau)\rangle}{\langle E(t)^2\rangle} \ , \tag{2.27}$$

where $\langle\rangle$ denotes the average over time t, is applied to the analytically derived field equation 2.20. Since the autocorrelation will be normalized, all pre-factors are neglected. Which leads to

$$g_1(q,\tau) = \frac{\sum_j \langle b_j(q,t) b_j^\star(q,t+\tau) e^{-i\mathbf{q}(\mathbf{R}_j(t)-\mathbf{R}_j(t+\tau))}\rangle}{\sum_j \langle b_j(q,t) b_j^\star(q,t)\rangle} \,. \tag{2.28}$$

For identical particles, all b_j are equal, then the autocorrelation function

$$g_1(q,\tau) = \langle e^{-i\mathbf{q}\Delta\mathbf{R}(\tau)}\rangle \tag{2.29}$$

solely depends on the displacement $\Delta\mathbf{R}(\tau)$ projected on $\mathbf{q}$ [205]. For a diffusive random-walk motion $\Delta R(\tau)$ is isotropic and gaussian distributed, the mean squared displacement

$$\langle \Delta R(\tau)^2 \rangle = 6D\tau \tag{2.30}$$

is a function of the diffusion coefficient D of the particle [205]. Combining eq. 2.30 and eq. 2.29 produces the simple expression

$$g_1(q,\tau) = e^{-q^2 D\tau} \,. \tag{2.31}$$

For spherical particles the Stokes-Einstein relation

$$D = \frac{k_B T}{6\pi\eta a} \tag{2.32}$$

yields the hydrodynamic radius a as a function of D, which is used for particle sizing in single scattering experiments (Section 6.3.2).

Data analysis

In a Dynamic Light Scattering experiment, a photodetector is connected to a hardware correlator that calculates the intensity autocorrelation function

$$g_2(\tau) = \frac{\langle I(t) I(t+\tau)\rangle}{\langle I(t)\rangle^2} \,. \tag{2.33}$$

The theoretical connection between the measured g_2 and the previously derived g_1 (eq. 2.44) is given by the Siegert Relation

$$g_2(\tau) = 1 + \beta |g_1(\tau)|^2 \,, \tag{2.34}$$

where β is the intercept [21]. The measured function converges when the measuring time is large compared to the observed timescales. Then the intercept β is the inverse of the number of detected speckle modes $\beta = 1/M$. By using a single mode fiber and polarization filter, β should be close to one. However, the Siegert relation 2.34 is only valid when the *time* average of the measurement is equal to the *ensemble* average. This is the case for particles in Brownian motion, where every particle moves arbitrarily far. Then all possible realizations of positions $\mathbf{R_j}$ occur with time and the measurement is said to be *ergodic*. In a gel or bulk biological tissue, constrains on the thermal diffusion can cause a non-ergodic measurement[205]. The phase is not randomized completely. As a consequence, the normalization of the correlation function is ill-posed. Measuring an average correlation function requires additional concepts (see e.g.[155]).

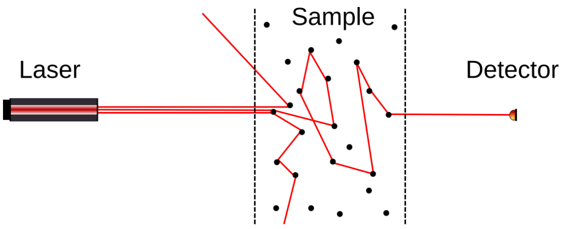

Figure 2.5: Sketch of a path for multiple light scattering. Coherent laser light is pointed onto a turbid sample. Inside the Sample, the photon transport is a random walk (diffusion). Light leaves the Sample in all directions, some paths end at the detector.

2.2.4 Diffusing Wave Spectroscopy

So far it is assumed that each detected photon is scattered exactly once. This situation is easily achievable in dilute suspensions, where the number density of particles can be adjusted accordingly. However, most natural materials are strongly scattering, and this is also true for neuronal tissue. Diffusing Wave Spectroscopy (DWS) allows to measure the dynamics in such systems. In a turbid sample, the mean free path l_s (eq. 2.9) is smaller than the sample size. A photon is scattered many times along its path through the sample and there are many possible paths, see figure 2.5. The length of a path p with N scattering events

$$s_p = \sum_{i=1}^{N} |r_{i+1} - r_i| \tag{2.35}$$

leads to the final phase

$$\phi_p = k_0 s_p = \sum_{i=1}^{N} k_i \cdot (r_{i+1} - r_i) \ , \tag{2.36}$$

where k_i is the wavevector after the i-th scattering event. The amplitude at the detector is the coherent sum of the fields E_p from all paths [30]

$$E(t) = \sum_p E_p e^{i\phi_p(t)} \ . \tag{2.37}$$

The number of paths and scattering events is very large. Therefore the total phase at the detector is a random variable and the autocorrelation function (eq. 2.27) of the detected field (eq. 2.37) can be expressed using the central limit theorem [30]

$$g_1(\tau) = \sum_p P(p) e^{-\langle \Delta\phi_p^2(\tau)\rangle/2} \ . \tag{2.38}$$

The displacements of scatterers along the path lead to the phase shift

$$\Delta\phi_p(\tau) = \sum_{i=1}^{N} \vec{q}_i \cdot \Delta\vec{r}_i(\tau) \ . \tag{2.39}$$

Assuming independent scattering events, the expression

$$\left\langle \Delta\phi_p^2(\tau) \right\rangle = N \left\langle (\vec{q}_i \cdot \vec{r}_i(\tau))^2 \right\rangle = \frac{1}{3} N \left\langle q_i^2 \right\rangle \left\langle r_i^2(\tau) \right\rangle , \tag{2.40}$$

is found. The average squared scattering vector $\langle q^2 \rangle$ is an average over q, weighted with the formfactor of the scatterer. The important length scale in a DWS experiment is the transport mean free path

$$l^\star = \frac{l_s}{\langle 1 - \cos\vartheta \rangle} \tag{2.41}$$

where ϑ is the scattering angle and $\langle\rangle$ denotes the average over many scattering events [30]. It is the length scale over which the direction of propagation is randomized. When the sample is large, the light transport is diffusive and the photons perform a random walk with the step length $l^\star$. For small particles $l^\star \approx l_s$ whereas large particles randomize the direction of the light only after multiple scattering events and $l^\star > l_s$. With the definition of $l^\star$ from equation 2.41, $\langle q^2 \rangle$ simplifies to [127]

$$\left\langle q^2 \right\rangle = \left\langle (2k_0 \sin(\vartheta/2))^2 \right\rangle = 2k_0^2 \left\langle 1 - \cos(\vartheta) \right\rangle = 2k_0^2 \frac{l}{l^\star} \tag{2.42}$$

Combining eq. 2.42 and eq.2.40 yields

$$\left\langle \Delta\phi_p^2(\tau) \right\rangle = \frac{2}{3} k_0^2 \left\langle \Delta r_i^2(\tau) \right\rangle \frac{s}{l^\star} . \tag{2.43}$$

Since this equation depends on the path length, the sum over individual paths can be exchanged by an integral over path lengths. With the path length distribution $P(s)$ the transition to the continuum limes yields the final expression [127]

$$g_1(\tau) = \int_0^\infty P(s) e^{-\frac{1}{3} k_0^2 \left\langle \Delta r^2(\tau) \right\rangle \frac{s}{l^\star}} ds . \tag{2.44}$$

Compared to single scattering, instead of the scattering angle ϑ, the decorrelation scale with $s/l^\star$. A quantitative analysis requires knowledge of the path length distribution $P(s)$. Explicit equations have been derived for many geometries [124]. The solution for transmission and backscattering geometries are presented in the following.

In transmission geometry, a sample of size L is placed between the illuminating light source and the detector. The maximum of the path length distribution is around $\hat{s} \approx L^2/(4l^\star)$. The distribution is asymmetric, there exist very long paths, but no path shorter then L. The effective *average* path length can be approximated by $\hat{s}/2$ and the path length distribution replaced by a delta function at this value. Then the field autocorrelation function is [199]

$$g_1(\tau) = \exp\left(-\left(\tfrac{L}{l^\star}\right)^2 k^2 \langle \Delta r^2(\tau) \rangle \right) . \tag{2.45}$$

When light source and detector are on the same side of the sample, the geometry is referred to as backscattering. For a semi-infinite sample the field autocorrelation function is approximated as [167]

$$g_1(\tau) = \exp\left(-\gamma \sqrt{k^2 \langle \Delta r^2(\tau) \rangle} \right) . \tag{2.46}$$

With $\gamma = \frac{z_0}{l^\star} + \frac{2}{3}$ where z_0 represents the depth where the photon transport starts to be diffusive. From this point on, the information about the incoming direction of the light is lost hence the distribution of propagation directions is isotropic. The analytic derivation of z_0 is complex, it depends on incoming and detected polarization as well as scattering anisotropy $\langle 1 - \cos(\vartheta) \rangle$. The exact parameters are usually not known. To still be able to analyze the result, one can use the simplification $z_0 \approx l^\star$ and $\gamma \approx 2$ [152].

By performing transmission and backscattering experiments, precise measurements of $l^\star$ and the mean squared displacement are possible. Analog to the single scattering data analysis, one can calculate the diffusion coefficient and hydrodynamic radius (using equation 2.30 and 2.32). DWS can detect very small displacements since the sensitivity increases with the path length.

2.3 Birefringence

When light is transmitted through an anisotropic medium, the index of refraction depends on the orientation of the polarization. As a result, the polarization state is modified which is called birefringence [27, 48]. Information about the microscopic structure and alignment of proteins or particles are gained by measuring the birefringence. Biological structures, like alpha helices or collagen fibers build up highly anisotropic and therefore birefringent tissue. Many proteins, viruses and polymers have been analyzed via measurements of birefringence [64, 65, 128].

The optical index depends on the orientation of the polarization and the optical axis of an anisotropic molecule. In uniaxial materials a single direction specifies the orientation, and a rotation around this axis does not change the optical properties. Then the birefringence is described by an index ellipsoid with the index parallel $n_{\parallel}$ and perpendicular to its axis $n_{\perp}$.

2.3.1 Transmission experiment

Birefringence can be detected by an increased transmission when a sample is placed between crossed polarizers. A general introduction to the measurement principle is given in e.g. [34, 48], and the experimental geometry is depicted in figure 2.6 Without loss of generality, the incoming wave is described by two components. These are perpendicular and parallel to the optical axis of the sample

$$E_{\parallel} = \frac{1}{\sqrt{2}} E_0 \cos(\omega t - \Delta\phi/2) \qquad \text{and} \qquad E_{\perp} = \frac{1}{\sqrt{2}} E_0 \cos(\omega t + \Delta\phi/2)\ , \tag{2.47}$$

where $\Delta\phi$ is the phase shift between those two waves. The difference in indices

$$\Delta n = n_{\parallel} - n_{\perp} \tag{2.48}$$

slows down one component of the wave with respect to the other. When the incoming light is linear polarized $\Delta\phi = 0$. The resulting retardance

$$R = \Delta n \cdot L \tag{2.49}$$

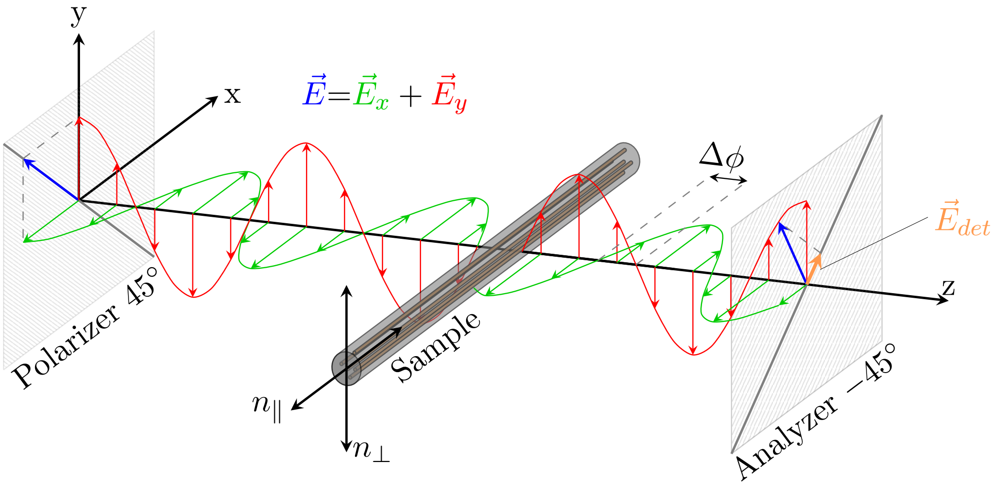

Figure 2.6: Basic principle of a birefringence measurement. The incoming wave (left) is expressed via its x and y components. It passes a linear polarizer, tilted by 45°. The second polarizer (Analyzer) is crossed to the first one (at −45°) so the incident light is blocked. While penetrating the sample, the x component feels the index $n_\parallel > n_\perp$. As a consequence, it is retarded by $\Delta\phi$. The superposition of the x and y component is no longer linear, but elliptic (see figure 2.7, left). Therefore, a part of the wave $\mathbf{E}_{\text{det}}$ can pass the analyzer.

generates an ellipsoidal polarization (see figure 2.7, left). The resulting phase shift is

$$\Delta\phi = \frac{2\pi}{\lambda} R\,. \tag{2.50}$$

A linear polarized beam penetrates the sample and is detected after passing a polarization filter.

The phase of the detected light is analyzed by the use of polarization filter (analyzer) that is crossed to the incoming polarization (see figure 2.6). The analyzer is penetrated by

$$\begin{aligned} E_{\text{det}} &= \frac{1}{2}\left[\cos\left(\omega t - \Delta\phi/2\right) - \cos\left(\omega t + \Delta\phi/2\right)\right] & (2.51)\\ &= E_0 \sin\left(\Delta\phi/2\right)\sin\left(\omega t\right) \ . & (2.52)\end{aligned}$$

With $I \propto E^2$ the transmittance becomes

$$T = \frac{I_{\text{det}}}{I_0} = \sin^2\left(\Delta\phi/2\right) \ . \tag{2.53}$$

Dichroism

The absorption coefficient can depend on polarization, which is called dichroism. Depending on the measurement principle this effect can be hard to distinguish from birefringence. Like birefringence, dichroism arises from anisotropic microscopic structures.

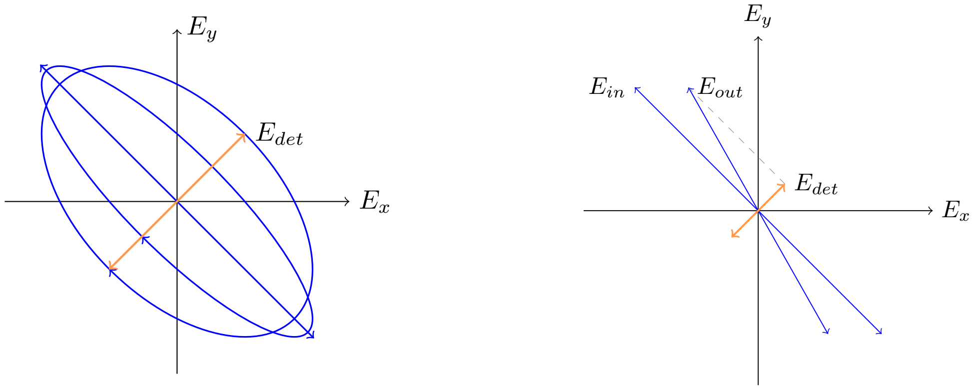

Figure 2.7: (left) Polarization states for different phase shifts $\Delta\phi$, caused by retardance. The component that is perpendicular to the incoming light E_{det} can pass the analyzer and is detected. (right) The modulation of polarization resulting from dichroism. This also results in a field E_{det} that passes the analyzer.

When one component of linear polarized light is diminished, the polarization direction is tilted (see figure 2.7, right). The polarization state remains linear, but incorporates components perpendicular to the incoming wave.

2.3.2 Measuring Birefringence using Modulated Light

When $\Delta\phi$ is small the signal is proportional to the squared retardance $\Delta\phi^2$. The resulting difficulty in measuring weak birefringent samples can be overcome by the use of photoelastic modulator (PEM) in combination with a Lock-In amplifier (this method is described e.g. in [125, 126, 128]). The PEM is a piezoelectric crystal, where an AC voltage is applied at the mechanical resonant frequency ω of the crystal. Its optical axis is perpendicular to the beamline and aligned at 0°, while the crossed polarizers are aligned at ±45°. The PEM generates an oscillating retardance

$$\Delta\phi_{PEM} = a\sin\left(\omega t\right) \ , \tag{2.54}$$

with frequency ω and amplitude a. Hence the transmittance becomes

$$\begin{aligned} T &= \frac{1}{2}\left[1 - \cos\left(\Delta\phi_S + \Delta\phi_{PEM}\right)\right] & (2.55)\\ &= \frac{1}{2}\left[1 - \cos\left(\Delta\phi_S\right)\cos\left(\Delta\phi_{PEM}\right) + \sin\left(\Delta\phi_S\right)\sin\left(\Delta\phi_{PEM}\right)\right] \ . & (2.56)\end{aligned}$$

Since $\Delta\phi_S \ll 1$ the transmittance is approximated as

$$T \approx \frac{1}{2}\left[1 - \cos\left(\Delta\phi_{PEM}\right) + \Delta\phi_S\sin\left(\Delta\phi_{PEM}\right)\right] \ . \tag{2.57}$$

$\Delta\phi_{PEM}$ oscillates at frequency ω. The fundamental frequency of the cosine term is at 2ω whereas the sine contributes at ω. As $\Delta\phi_S$ is of interest, only the frequency ω is measured. This is achieved with the use of the Lock-In amplifier. Hence the rear sine term in 2.57 is expanded to

$$\sin(\Delta\phi_{PEM}) = \sin\left(a\sin(\omega t)\right) \tag{2.58}$$

$$\approx a\sin(\omega t) - \frac{a^3}{6}\sin^3(\omega t) + \frac{a^5}{120}\sin^5(\omega t) \tag{2.59}$$

Powers of sine also contain the fundamental frequency. These components need to be derived with the use of the trigonometric relations

$$\sin^3\theta = \frac{3\sin\theta - \sin(3\theta)}{4} \quad \text{and} \quad \sin^5\theta = \frac{10\sin\theta - 5\sin(3\theta) + \sin(5\theta)}{16}\,. \tag{2.60}$$

The resulting amplitude at the frequency of interest

$$\sin\left(a\sin(\omega t)\right)\Big|_{\omega} \approx \left(a - \frac{a^3}{8} + \frac{a^5}{192}\right)\sin(\omega t) \tag{2.61}$$

finally leads to the transmittance at the fundamental frequency

$$T\Big|_{\omega} \approx \frac{\Delta\phi_S}{2}\left(a - \frac{a^3}{8} + \frac{a^5}{192}\right)\sin(\omega t)\,. \tag{2.62}$$

The key advantage is that the signal $T\big|_{\omega}$ is linear proportional to $\Delta\phi_S$. This increases the sensitivity by orders of magnitude and also enables the determination of the sign. The linear relation in equation 2.62 is used to calibrate the measurement via

$$\Delta\phi_S = I_{\omega}\cdot\xi\,, \tag{2.63}$$

where ξ is the calibration factor and I_{ω} the detected signal. The value of ξ depends on optical parameters like laser power, modulation amplitude and detection efficiency. The samples absorption and scattering (see equation 2.10) diminishes the signal, therefore ξ. With a well calibrated birefringent optical element (e.g. Babinet Soleil compensator) ξ can be measured with high precision.

3 Theory of electrophysiology

> With four parameters I can fit an elephant, and with five I can make him wiggle his trunk.
>
> *(John von Neumann)*

3.1 Introduction

This chapter summarizes different theoretical concepts to describe neuronal signaling. Neurons communicate with each other by transmitting, distinct pulses known as Action Potentials (AP). They can be detected by a spike in the electric potential using e.g. intracellular or extracellular electrodes. Besides the electric manifestation of the Action Potential, there are optical [14, 39, 62, 115, 118, 186, 203], thermal [161, 188] and mechanical [59, 63, 85, 101, 188] changes of the cell membrane. Many models have been derived to describe Action Potentials [78, 83, 90, 98, 139, 163–165, 172, 173, 179, 182, 183].

The most notable signal of the AP is unquestionable the electric one, thus a purely electric framework is presented first, alternative models are presented in Section 3.3. The passive electric properties of a nerve fiber are well described by the electric cable theory [90, 144, 191]. Reproducing Action Potentials requires an additional non-linear response of the membrane properties. This non-linearity may be given by the famous Hodgkin-Huxley (HH) model [91, 97], or by the Tasaki Cable (TC) model [184, 191].

The HH model is based on ion-specific voltage gated channels that control the electric conductivity of the membrane. It adds many time dependent differential equations with more than 20 parameters to the cable equation. Most of the HH parameters can not be

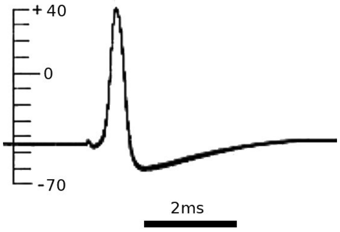

Figure 3.1: First recording of an intracellular Action Potential. The spike is around 100 mV in amplitude and followed by a brief undershoot. (modified from [89]).

measured directly, but are used to fit the model to experimental data. It is presented in Section 3.2.3. In contrast to this, the Tasaki Cable (TC) model adds just two parameters to the passive cable equation. The TC model may be seen as a radical simplification of the HH model, jet it reproduces the generation, propagation *and* annihilation of APs. The important aspects of AP propagation are consequences of the cable model and do not depend on the details of the non-linearity (e.g. channels).

3.2 Electric cable theory

3.2.1 Tasaki cable model

The following description of the cable-model is mainly a summary of the model as proposed by Tasaki, which is referred to as TC model [184, 191]. The TC model explains the generation, propagation and annihilation of APs, and the argumentation is also valid for the HH model. In a cable model, the membrane is represented by a linear chain of compartments (see figure 3.2), each having a resting potential E_r, resistance ρ_m and capacity c_m, as well as an inner resistivity r_i[90, 144, 162, 191]. These values are expressed per length, thus ρ_m is in $\Omega\,\mathrm{m}$, r_i in $\Omega\,\mathrm{m}^{-1}$ and c_m in $\mathrm{F}\,\mathrm{m}^{-1}$. Which leads to the second-order partial differential equation

$$c_m \frac{\partial V(x,t)}{\partial t} + \frac{1}{\rho_m}(V(x,t) - E_r) = \frac{1}{r_i}\frac{\partial^2 V(x,t)}{\partial x^2} \ , \tag{3.1}$$

with the internal resistance r_i and the membrane potential $V(x,t)$. The characteristic properties of a passive membrane are a time constant τ and a passive length constant λ

$$\tau = \rho_m c_m \quad \text{and} \quad \lambda = \sqrt{\rho_m / r_i} \tag{3.2}$$

are derived. The process of transmission is a consequence of the boundary between the resting and the active section of the nerve [191]. In the active region, the membrane strives towards the *action* potential E_a (or $E_r^\star$) and the corresponding values of resistance and capacity are asterisked ($\rho_m^\star$, $c_m^\star$). The AP is a localized, traveling pulse, that retains its shape. If the observer follows the AP with the propagation velocity v, the membrane potential $V(x,t)$ is stationary $V(X)$. Thus the transformation $X = x - vt$ reduces the cable equation 3.1 to the ordinary differential equation

$$\frac{1}{r_i}\frac{d^2V(X)}{dX^2} + c_m v \frac{dV(X)}{dX} - \frac{1}{\rho_m}(V(X) - E_r) = 0 \tag{3.3}$$

for the resting section, and

$$\frac{1}{r_i}\frac{d^2V(X)}{dX^2} + c_m^\star v \frac{dV(X)}{dX} - \frac{1}{\rho_m^\star}(V(X) - E_a) = 0 \tag{3.4}$$

for the active section. Those equations have analytical solutions. The center of the AP (X=0) is defined as the position where $V(X) = E_{1/2} = (E_a + E_r)/2$, then the solutions

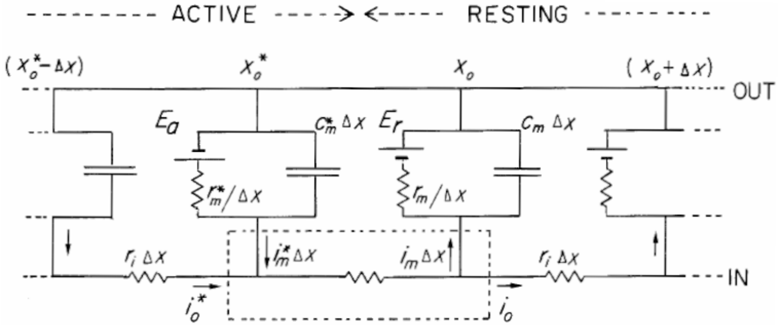

Figure 3.2: Electrical network representing an active nerve fiber. The equilibrium potential in the resting region is E_r, in the active region it is E_a. The membrane resistance ρ_m and capacity c_m change when the nerve is activated, as indicated by the asterisk symbols (from [191]).

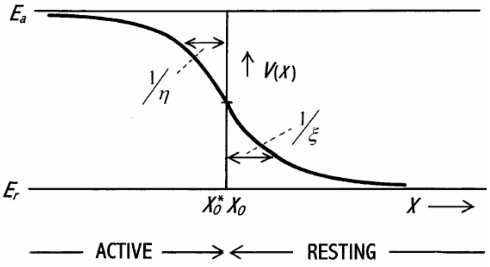

Figure 3.3: Profile of the membrane potential $V(X)$ of the AP in the TC model. The membrane potential rapidly jumps up from the resting potential E_r to the potential of the active section E_a, the width of the rising phase is given by the length parameters ξ^{-1} and η^{-1}. (from [191])

for the active and resting section are

$$V(X>0) = E_r + (E_{1/2} - E_r)\,e^{-X\xi} \text{ and} \tag{3.5}$$

$$V(X<0) = E_a - (E_a - E_{1/2})\,e^{X\eta}\ , \tag{3.6}$$

with the space parameters ξ and η [191], as is shown in Figure 3.3. These parameters define the width of the boundary. It is then found that the solution is symmetric with respect to the boundary at $X=0$ with

$$\xi^{-1} = \eta^{-1} = \sqrt{2\rho_m^\star/r_i}\ . \tag{3.7}$$

The total width of the rising phase of the AP is then $\lambda^\star = 2\xi^{-1}$, which is the width of the AP in the TC model. For the classical squid axon, $\lambda^\star$ is around 2 mm. This active length can be compared to the passive length constant $\lambda = \sqrt{\rho_m/r_i} \approx 7\,\text{mm}$. The exact solution for the velocity is given in [191]. Under the assumption $\rho_m^\star \ll \rho_m$ and $c_m^\star \approx c_m$, the simple approximation

$$v \approx \frac{1}{c_m \sqrt{2 r_i \rho_m^\star}} \tag{3.8}$$

is found. Typical physiological parameters of a squid axon are $c_m = 8\,\mu\mathrm{F\,cm^{-1}}$, $r_i = 29\,\mathrm{k\Omega\,cm^{-1}}$ and $\rho_m^\star = 175\,\Omega\,\mathrm{cm}$ [191][1]. The subsequent conduction velocity $v \approx 24\,\mathrm{m\,s^{-1}}$ is in good agreement the experimentally observed value. This simple concept explains the generation, propagation and termination of APs with very few parameters, that are directly determined in experiments. Assumptions about the microscopic details of the electrochemical processes are not required [191].

3.2.2 The semipermeable membrane

This section describes the physics of semipermeable membranes on the basis of [141]. The resulting equations are the inspiration for the HH model, which is presented in Section 3.2.3.

Equilibrium

In a closed cell or vesicle, the existence of permeant and impermeant species of ions creates a finite voltage V_m across the membrane. In thermal equilibrium the concentration distribution $c(r)$ of any permeable ions will obey the Boltzmann principle

$$c(r) \propto \exp\left(-\frac{E(r)}{k_B T}\right) , \tag{3.9}$$

with the potential energy $E(r)$ at position r. If we assume ions of single charge $E(r) = eV(r)$, and only distinguish between the outside and inside of the axon, the ratio of concentration

$$\frac{c_{in}}{c_{out}} = \exp\left(-\frac{e}{k_B T}(V_{out} - V_{in})\right) \tag{3.10}$$

can be solved for the membrane voltage $V_m = V_{in} - V_{out}$. This produces

$$V_m = \frac{k_B T}{e} \ln\left(\frac{c_{in}}{c_{out}}\right) , \tag{3.11}$$

called the Nernst equation [141]. In a living cell there may be many important ions. For simplicity only Na^+, K^+ and Cl^- are considered here. All ionic species are subject to the same electrostatic potential V_m. If all ions are permeant, their Nernst Potential is equal (see eq. 3.11) and therefore their concentration ratio

$$\frac{c_{out,\mathrm{Na}^+}}{c_{in,\mathrm{Na}^+}} = \frac{c_{out,\mathrm{K}^+}}{c_{in,\mathrm{K}^+}} = \frac{c_{in,\mathrm{Cl}^-}}{c_{out,\mathrm{Cl}^-}} \tag{3.12}$$

is also equal. In the extracellular medium the ion concentration is around $c_{out,\mathrm{Na}^+} = 140\mathrm{mM}$, $c_{out,\mathrm{K}^+} = 10\mathrm{mM}$ and $c_{out,\mathrm{Cl}^-} = 150\mathrm{mM}$. However any not permeant charge will

---

[1] Calculated for an axon of diameter 0.4 mm

not obey the Nernst relation. In a cell there are additional proteins and nucleic acids that carry a net negative charge. The trapped charge density is around $\rho = 125\mathrm{mM}e$. If we demand charge neutrality inside the cell, we get

$$c_{in,\mathrm{Na}^+} + c_{in,\mathrm{K}^+} + c_{in,\mathrm{Cl}^-} + \frac{\rho}{e} = 0 \; . \tag{3.13}$$

Combining equation 3.12 with 3.13 and the given values for c_{out} and ρ results in

$$V_m \approx -10\,\mathrm{mV} \; , \tag{3.14}$$

which is the membrane potential in thermal equilibrium, also called Donnan potential [141].

Non-Equilibrium

Life requires free energy, which is stored in an non-equilibrium resting state. The membrane voltage of a living cell is not near the Donnan equilibrium potential, the cell would be dead if it was. In this non-equilibrium state, every species of ions i has its own Nernst Potential, and contributes to the total membrane current by

$$I_i = g_i \left(V - V_i^{Nernst} \right) \; , \tag{3.15}$$

with their individual conductances g_i and Nernst Potentials V_i^{Nernst}. A molecular motor (ATPase) hydrolyzes ATP and uses the spare free energy to perform ion pumping to maintain the resting state. The pumped current has to compensate the ohmic leakage of each ion i, so that the net current

$$I_{total} = I_i^{pump} \sum_i I_i \tag{3.16}$$

is zero. The actual membrane voltage is $V_m \approx -60\,\mathrm{mV}$ and measurements of the intracellular ion concentration deliver a estimation of the Nernst Potentials [141]

$$V_{\mathrm{Na}+} \approx 54\,\mathrm{mV} \; , \quad V_{\mathrm{K}+} \approx -75\,\mathrm{mV} \quad \text{and} \quad V_{\mathrm{Cl}-} \approx -59\,\mathrm{mV} \; . \tag{3.17}$$

The cell maintains this state of high free energy while avoiding large mechanical pressure. This is achieved by performing a coupled transport of sodium out and potassium into the cell. The enzyme ATPase hydrolyzes ATP and swaps 3 Na^+ ions for 2 K^+ ions each cycle, thus $j_{\mathrm{K}+} = \frac{-2}{3} j_{\mathrm{Na}+}$. The resulting resting membrane potential in the resting state is consequently

$$V_m = \frac{2 g_{\mathrm{Na}^+} V_{\mathrm{Na}^+}^{Nernst} + 3 g_{\mathrm{K}^+} V_{\mathrm{K}^+}^{Nernst}}{2 g_{\mathrm{K}^+} + 3 g_{\mathrm{Na}^+}} \; . \tag{3.18}$$

Each ion species of ions can be seen as a battery with a specific potential, and the total potential is a function of the specific permeabilities [141]. While these equations look simple, the electrochemical effects are not always trivial, even if they are given by the Nernst equation [196]

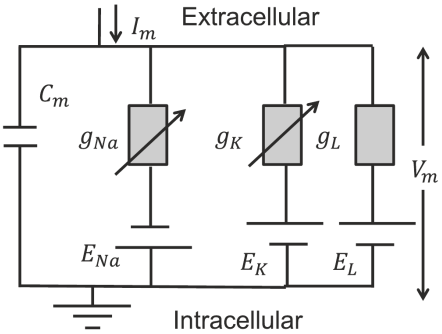

Figure 3.4: Equivalent circuit for the original Hodgkin Huxley model. The membrane is represented by a capacitor C_m that experiences the membrane voltage V_m. The ion current is modeled via charged capacitors, representing the Nernst Potential and variable resistors (from [164]).

3.2.3 Hodgkin Huxley Model

The electrochemical potential that arises from the difference between specific Nernst Potentials and the resting potential (eq. 3.18) across the membrane can be described by charged capacitors. Hodgkin and Huxley (HH) postulated that voltage gated ion channels are selective to different ion species. The resulting membrane permeability for specific ions i (where i is either Na, K or l) is coupled to the local electric field [90]. The current I_l represents unspecific ohmic leakage of other ions (mainly Cl^-), it drives the cell towards the Donnan equilibrium (eq. 3.14). The membrane is represented by an equivalent circuit shown in figure 3.4. All ion channels are wired in parallel and the total current through the membrane

$$I = \underbrace{C_m \frac{dV}{dt}}_{I_C} + I_{\mathrm{Na}^+} + I_{\mathrm{K}^+} + I_{\mathrm{l}} \tag{3.19}$$

is the sum of capacitive current I_C and ionic currents I_i.

The response of the ionic conductances $g_i(V_m, t)$ are time dependent functions of the membrane voltage V_m. They build the core of the HH model and are obtained by fitting the model to experimental data. The physical basis for these expressions lies in the assumption of two states of conduction, regulated through Boltzmann factors [141]. Later, microscopic Patch-clamp recordings indicated two discrete values of conductivity, which were interpreted as single channels being either *open* or *closed* [11]. The macroscopic conductivity is dictated by the fraction of channels that are opened. In a two state system, the channels obey a Boltzmann distribution

$$P_{\mathrm{open}} = \frac{1}{1 + \exp \Delta F / k_b T} , \tag{3.20}$$

where ΔF is the free energy difference between open and closed state [141]. Figure 3.5 suggests an electrostatic energy in the form $\Delta F_1 = qVl/d$ with the membrane thickness

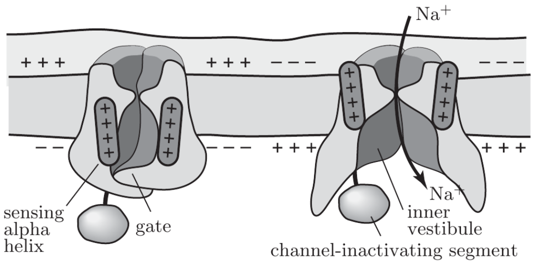

Figure 3.5: Hypothetical function of voltage gated channels. A charged alpha helix is embedded in the protein and senses the local field. Variations in the membrane potential can facilitate a conformational change and consequently allow or block the permeation of specific ions (from [141]).

d, the effective sum of charges on the alpha helix q and its transversal displacement l. When the free energy is expressed as a sum of a constant ΔF_0 and a voltage dependent $\Delta F_1(V)$ the probabilities can be expressed as

$$P_{\text{open}}(V) \propto \frac{1}{1+\exp(a+bV)} \tag{3.21}$$

with two unknown parameters a and b [141]. Expression 3.21 can be seen as the basis for transfer rates (eq.3.24) that control the current. Ionic conductances g_i are expressed in terms of their maximal conductance $\bar{g}_i$

$$g_{\text{Na}^+} = \bar{g}_{\text{Na}^+} m^3 h \ , \quad g_{\text{K}^+} = \bar{g}_{\text{K}^+} n^4 \quad \text{and} \quad g_{\text{l}} = \bar{g}_l \ . \tag{3.22}$$

The time dependent expressions n, m, h are dimensionless abstractions of ion ratio and range from 0 to 1. Its exponents can be interpreted as the amount of particles involved in an ion permeation event. Only the conductance of the leakage channel is time independent. The conductance of sodium is a two-stage process, involving the fast close-open transition as well as an additional inactivation. The second process involves a channel-inactivating segment (see figure 3.5). Its slower dynamics is reflected through the additional parameter h. The values n, m, h correspond to the individual transfer rates α and β through

$$\begin{aligned} \frac{dn}{dt} &= \alpha_n(V_m)(1-n) - \beta_n(V_m)n \ , \\ \frac{dm}{dt} &= \alpha_m(V_m)(1-m) - \beta_m(V_m)m \quad \text{and} \\ \frac{dh}{dt} &= \alpha_h(V_m)(1-h) - \beta_h(V_m)h \ . \end{aligned} \tag{3.23}$$

The original set of transfer functions provided by Hodgkin and Huxley are

$$\begin{aligned} \alpha_n' &= \frac{0.01(10-V_m')}{\exp\left(\frac{10-V_m'}{10}\right)-1} & \beta_n' &= 0.125\exp\left(\frac{-V_m'}{80}\right) \\ \alpha_m' &= \frac{0.1(25-V_m')}{\exp\left(\frac{25-V_m'}{10}\right)-1} & \beta_m' &= 4\exp\left(\frac{-V_m'}{18}\right) \\ \alpha_h' &= 0.07\exp\left(\frac{-V_m'}{20}\right) & \beta_h' &= \frac{1}{\exp\left(\frac{30-V_m'}{10}\right)+1} \end{aligned} \tag{3.24}$$

with the abbreviations $V_m' = V_m/1\,\mathrm{mV}$ and $\alpha' = \alpha/1\,\mathrm{kHz}$ [90]. These parameters describe an excitable point-cell. Stimulation above threshold will generate a spike in the membrane potential that matches the Action Potential as shown in figure 3.1. In rapid succession to the stimulus the sodium channels open and a fast inward current depolarizes the cell. Then the sodium channels are inactivated and potassium conductivity increases. The outward potassium current repolarizes the cells interior, bringing it back to its resting value. A delayed closing of the potassium channels produces a brief undershoot, referred to as hyperpolarization. The whole process is based on dissipative ohmic currents, driven by individual electrochemical potentials. The HH model does not address the question where the energy is coming from.

Most nerves, especially mammalian neurons are much more complicated. Dozens of different ion species have to be considered. Appropriate modifications can be made, but may require numerous additional parameters to measure or fit.

The HH Action Potential

The HH equations can only be solved numerically. There are two canonical cases: a single compartment, and propagation on long cable. A single compartment may represent a small cell, or an axon where a long electrode shortens the cable properties. Historically, this has been referred to as the “membrane” AP [90]. When the membrane is triggered to change from the resting to the active state, this causes fluxes of ions across the membrane. These ions remain localized close to the membrane and contribute to the capacitive charging of the membrane (see circuit diagram 3.4). The total current $I_C = I_m$ is the derivation of the voltage. Accordingly I_C spikes at the steep rising phase of the voltage V_m, where the fast sodium current is not yet compensated by outflowing potassium (see figure3.6).

To calculate a propagating AP the HH expressions for the ionic conductances are inserted in the cable equation 3.1. Numerical treatment of the proposed equations is not straight forward. There exist a number of approximations that reduce the numerical effort. Especially for large populations, rather crude simplifications like the *integrate and fire* model dominate the scientific literature.

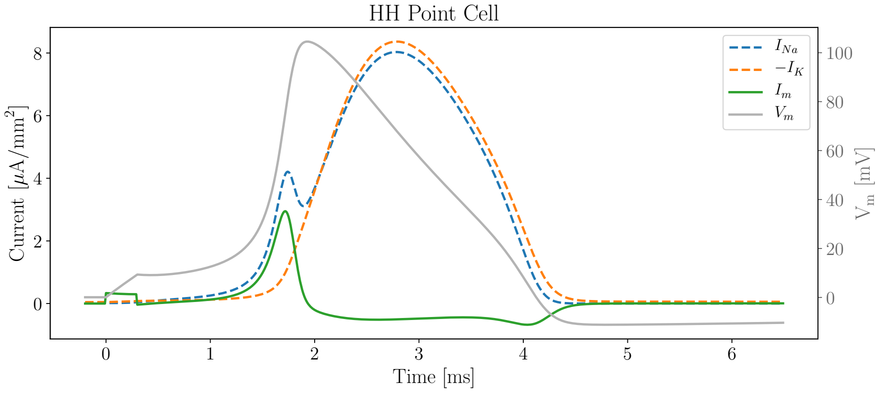

Figure 3.6: Simulated current components and membrane potential in a single Hodgkin-Huxley compartment. The stimulating current injection is visible at 0 ms to 0.3 ms. The membrane current is the sum of the ionic currents $I_{Na} + I_K = I_m$.

A personal review of historical criticism of the HH model

The HH model is inspired by the Nernst equation (or Goldman equation), it is not derived from these equations. The Authors had to introduce quite a few terms that have no physical basis. The model was found *after a good deal of trial and error*[2] [97], and the authors said that it is not an explanation, but an empirical description of the Action Potential. In their original publication they write:

> An equally satisfactory description of the voltage clamp data could no doubt have been achieved with equations of very different form, which would probably have been equally successful in predicting the electrical behaviour of the membrane. [...] *the success of the equations is no evidence in favour of the mechanism* of permeability change that we tentatively had in mind when formulating them.
>
> (HH [90], italics added)

While Hodgkin said that they just followed the lead of Kenneth Cole [42], he seemed not to have enjoyed Cole's critique:

> I infuriated Hodgkin by counting the number of ad hoc analytical forms and numerical values in their equations. (Kenneth Cole [42])

Cole published one of the first reports about limitations of the HH model and referred to it as the abominable notch, other named it the Cole-Moore delay [45]. They observed that the potassium current is delayed after a stimulus when the membrane potential is artificially kept below the resting potential prior to the stimulus. A better fit of the HH

---

[2] The calculations were done by hand and a single propagating Action Potential took weeks to calculate. With the trial and error approach, the scientists were kept busy for more than a year.

equations is possible by increasing the exponent of the gating variable n in eq.3.22 from 4 to 25 (even 700 in some cases).

> This difference can certainly be resolved by modification of already rather arbitrary assumptions. (Kenneth Cole [45])

Almost 20 Years later Cole reviewed the discussion with:

> The 'abominable notch' was still with us. Moore, Taylor, and I spent a couple of years on it-spurred on by Frankenhauser and Hodgkin, who ignored it, and by Tasaki and collaborators, who insisted that all good axons showed it. (Who wants to work on less than the best?) (Kenneth Cole [42])

The Cole-Moore delay remains unexplained [93, 96], just like the many other limitations of the Hodgkin Huxley model [17, 24, 43, 50, 58, 83, 97, 138, 185, 189]. Certainly the HH model has been very successful and contributed to decades of research.

> It should be emphasized in this connection that the success of this theory does not depend on the legitimacy of the assumptions made to derive the formal mathematical Eqs. (…). The success derives essentially from the applicability of Kirchhoffs law to the proposed equivalent circuit. (Tasaki [185])

Still the HH model and its mechanistic interpretation is often seen as a bare fact in the vast majority of the literature.

> I'm …worried you may be pushing some of your channel arguments pretty far.
>
> (Cole in a letter to Hille [47])

3.3 Non-electric properties of Action Potentials

> Physicists always have a habit of taking the simplest example of any phenomenon and calling it *physics* leaving the more complicated examples to become the concern of other fields ...
>
> *(Richard Feynman [56])*

3.3.1 The soliton

Action Potentials are quasi-stationary localized phenomena, they travel without changing their shape. Similar wave phenomena are found in many systems ranging from waves in shallow water to light pulses in fiber communication systems and are referred to as soliton (see e.g. [23]). The definition of a soliton is:

- Solitons are stationary. They move at constant speed without changing their shape.
- Solitons are localized. The analytical solution must vanish at $x \to \pm\infty$.

By this definition, the AP is a soliton. In some cases solitons are considered to penetrate each other when they meet head-on. However, APs do not penetrate but collide and annihilate [180]. Solitary mechanical pulses appear in non-linear and dispersive media. Such pulses can also collide and annihilate, it depends on the particular system [173].

Some non-electric theories of Action Potentials and membranes in general are presented in the following section.

3.3.2 Heat exchange and mechanical displacements

The AP is accompanied by a reversible heat exchange [161, 172, 188] as well as shortening and thickening of the nerve [59, 182, 190]. When current is injected into a nerve, the resting potential is restored by an outward current through the membrane. This creates heat because of the ohmic resistance of the membrane. A sub threshold pulse creates heat that dissipates as expected. In contrast, the observed cooling rate that accommodates an Action Potential is much faster than expected from dissipation [1, 28, 161, 187, 188]. This thermal response is in phase with the electric signal (see fig. 3.7, left). A rapid cooling can be explained by a fast decrease of pressure. The Action Potential is also accompanied by a small transversal displacement and longitudinal shortening. The transversal movement coincides with the electric Action Potential [188]. In figure 3.7 (right) the traces of this displacement are shown.

3.3.3 Theory of a cation-exchange coupled transition

Neuronal membranes can be excited by rising the extracellular sodium/calcium ratio $\langle Na^{+}\rangle/\langle Ca^{2+}\rangle$ [98, 182]. While approaching the critical value, increasing fluctuations of the membrane potential arise (see figure 3.8). Very close to the transition to excitation,

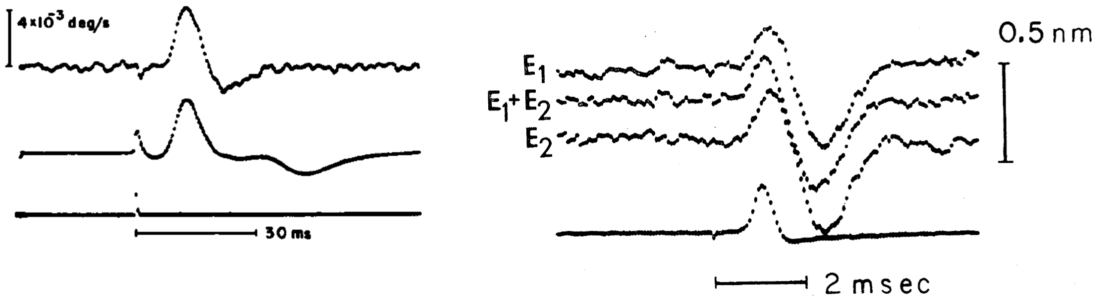

Figure 3.7: (**left**) The thermal response (upper trace) of an Action Potential. The electric signal is shown below. An AP is accompanied by a release and re-absorption of heat. (from [188]) (**right**) Transient transversal surface displacement of a nerve. Recorded for single sided (E_1 and E_2) and dual sided ($E_1 + E_2$) stimulation. The electric response is shown at the bottom. (from [190]).

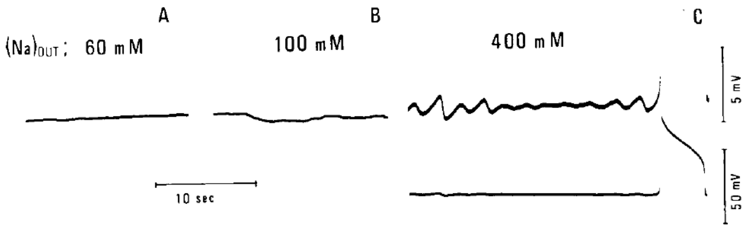

Figure 3.8: Time course of the membrane potential of a giant squid axon for varying ion ratio $\langle Na^+\rangle/\langle Ca^{2+}\rangle$. The sodium concentration is increased from left to right (A to C). An AP is triggered at the end of recording (C). Large fluctuations of the membrane potential are observed before the transition occurs (C, upper trace). (from [98]).

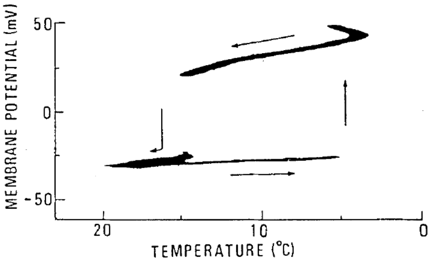

Figure 3.9: The membrane potential of a giant squid axon, internally perfused with a Na-salt solution. Cyclic temperature variation reveals a hysteresis for the transition between resting and active state (from [182]).

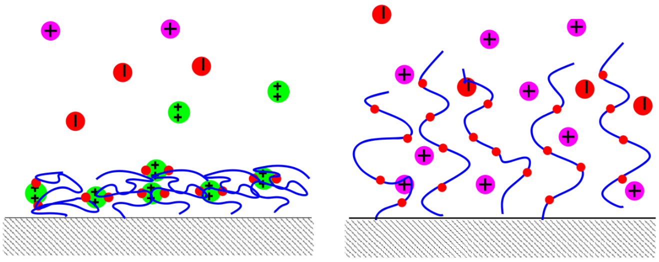

Figure 3.10: Effect of divalent ions on polyelectrolytes on a surface. (left) In a calcium rich environment, the attractive force dominates and the gel is in a dense cross-linked state. (right) Swollen state in the absence of calcium (from [140]).

giant fluctuations can be interpreted as an evidence for critical phenomena [98]. Analog to the ion ratio the variation of temperature can induce an abrupt voltage change. The membrane potential instantaneously jumps up around 70 mV when giant squid axons are cooled below a critical value. Rewarming the sample reverses the process and restores the resting potential. The transition switches between two stable states and a hysteresis is observed. Tasaki's Theory accounts for these observations based on fibrous proteins anchored at the cell membrane [182]. The idea is that these polyelectrolytes form a thin gel layer as depicted in figure 3.10. The steric repulsion and the electrostatic force between the negatively charged sites of the strands tend to expand the gel. The presence of a divalent ion, however, introduces an attractive force. It binds to multiple sites of the strands. When this force dominates, the structure collapses. This dense electrostatic cross linked gel is present in the resting state and the conformational change is coupled to a divalent-monovalent cation exchange. The temperature dependence of this transition can be described with the LeChatelier-Braun Principle [55, 104, 147]. When a transition is triggered, the release of calcium in the first phase of the AP is exothermic (see figure 3.9). Therefore, a decrease in temperature will favor the exited state, as observed in figure3.9. The discontinuous transition is coupled to a divalent-monovalent cation exchange. Similar mechanisms have been found in biological systems [79, 82, 132]

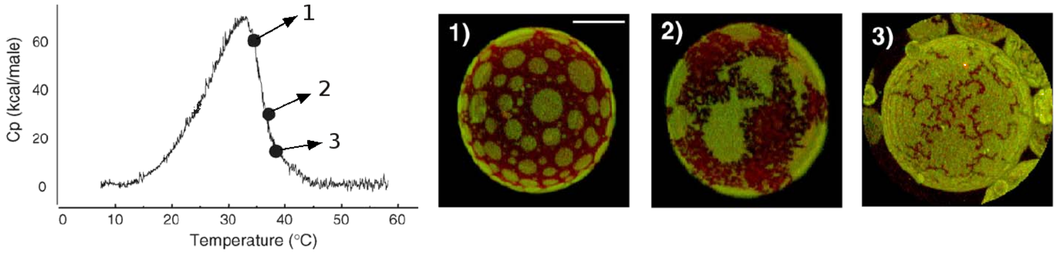

Figure 3.11: (left) Heat capacitance of surfactant membranes. (right) Corresponding false color image generated from two photon fluorescence of *LAURDAN* labeled giant unilamellar vesicles. The darker color indicates the gel phase, it coexists with a fluid phase [16].

and more recently in artificial systems [137, 140, 156]. The propagation of the AP is explained with the Tasaki Cable theory, Section 3.2.1.

3.3.4 Acoustic Solitary Pulse

The physics of acoustic solitons is introduced with observations in artificial systems. Then a wave equation is derived on the basis of the Heimburg-Jackson Theory [83, 114].

The main component of a cell membrane is the lipid bilayer. Such membranes have non-linear acoustic properties and in principle solitary pulses can occur [139]. Solitons have been shown in artificial membrane systems, and the underlying physics can be explored [173–175]. The lipid membranes of these systems can appear in different phases, a gel and a fluid phase. The non-linear response that is required by solitons is found in the vicinity of such a transition. Lipid phase transitions can be observed particularly impressive in Giant Unilamellar Vesicles (GUV) by the use of optical labels. The fluorescent *LAURDAN* probes align with the lipids, and their emission depends on the phase of the lipid membrane. The coexistence of gel-fluid phases and transitions is presented in figure 3.11. The gelation temperature is just below body temperature, and is also identified in the heat capacitance profile in figure 3.11 (left).

Shrivastava et al. used the opto-mechanical coupling of FRET molecules to observe solitons in a lipid interface[172–174]. The FRET signal strongly depends on the distance and mutual alignment of acceptor and donor molecules embedded in the membrane. A large DPPC[3] monolayer was prepared on a Langmuir-Blodgett trough. They inserted a razor blade attached to a piezoelectric element to induce mechanical perturbations (a mechanical stimulation) and measured the FRET intensity 1 cm away from the razor blade [175]. In vicinity of a phase transition, a solitary wave propagates along the membrane. Its shape almost perfectly matches the membrane potential during an Action Potential.

---

[3] Dipalmitoylphosphatidylcholine (DPPC) is a phospholipid and an important pulmonary surfactant.

Heimburg-Jackson model

In the Heimburg Jackson model, the AP is considered as an acoustic pulse that travels along the membrane. A wave equation is derived from first principles and solitary solutions are found. There is no direct coupling of this mechanism to the membrane potential, but a piezo effect or alike can explain the electric spike, which is described thereafter.

The sound propagation in elastic media depends on density ρ and compressibility κ. The compressibility of a membrane close to phase transition decreases with increasing density. The wave equation is expressed using the area density difference $\Delta\rho_A = \rho_A - \rho_{A,fluid}$ as

$$\frac{\partial^2 \Delta\rho_A}{\partial t^2} = \frac{\partial}{\partial x}\left(v^2 \frac{\partial \Delta\rho_A}{\partial x}\right) - h\frac{\partial^4 \Delta\rho_A}{\partial x^4}\ , \tag{3.25}$$

where h is a free parameter regulating the dispersion. The squared velocity

$$v^2 = \frac{1}{\rho^A \kappa_S^A} \approx v_0^2 + p\Delta\rho^A + q(\Delta\rho^A)^2 \tag{3.26}$$

is a function of isentropic area compressibility κ_S^A and area density ρ^A, it can be approximated by a taylor series. The isentropic compressibility, as required in equation 3.26, will be derived from the heat capacitance profile in the following. The heat capacitance c_p of artificial and biological membranes has been measured experimentally via constant pressure calorimetry [83].

The heat capacitance profile from DPPC vesicles is shown in figure 3.12 (upper left). The membrane possesses isothermal compressibilities of area κ_T^A and volume κ_T^V. Those values and the heat capacitance c_p are linked to fluctuations in area A, volume V and enthalpy H via

$$c_p = \frac{\langle H^2\rangle - \langle H\rangle^2}{RT^2}\ , \quad \kappa_T^V = \frac{\langle V^2\rangle - \langle V\rangle^2}{\langle V\rangle RT}\ , \quad \kappa_T^A = \frac{\langle A^2\rangle - \langle A\rangle^2}{\langle A\rangle RT}\ . \tag{3.27}$$

It was found experimentally, that for a wide variety of lipids and biological membranes the melting transition obeys

$$\Delta V(T) = \gamma_V \Delta H(T)\ , \quad \gamma_V = 7.8\times 10^{-4}\,\mathrm{cm^3/J} \quad \text{and} \tag{3.28}$$

$$\Delta A(T) = \gamma_A \Delta H(T)\ , \quad \gamma_A = 8.9\times 10^{3}\,\mathrm{cm^2/J}\ . \tag{3.29}$$

This enables a calculation of the elastic constants

$$\kappa_T^V = \kappa_{T,0}^V + \frac{\gamma_V^2 T}{\langle V\rangle}\Delta c_p \kappa_T^A \quad \text{and} \quad \kappa_T^A = \kappa_{T,0}^A + \frac{\gamma_A^2 T}{\langle A\rangle}\Delta c_p \tag{3.30}$$

from the heat capacitance. Finally Maxwell's relation can be used to calculate the isentropic compressibilities

$$\kappa_S^A = \kappa_T^A - \frac{T}{\langle A\rangle c_p}\left(\frac{dA}{dT}\right)_P^2\ . \tag{3.31}$$

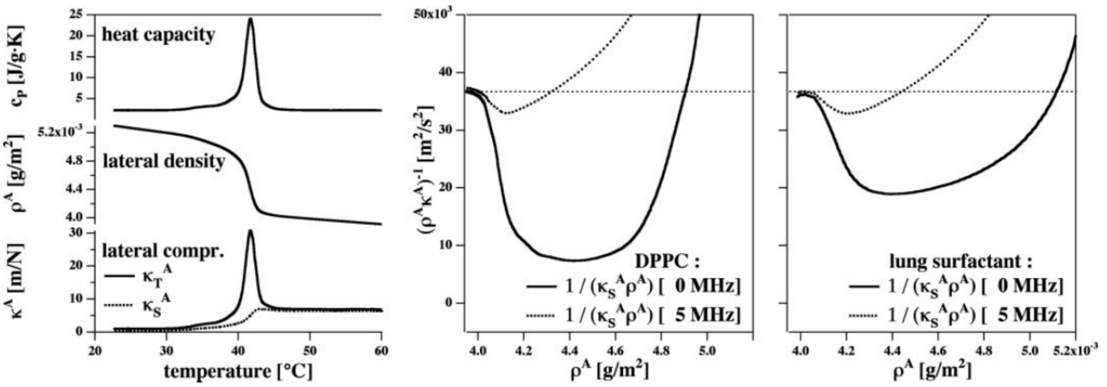

Figure 3.12: (left) Experimental data for the heat capacitance profile c_p of DPPC vesicles. The derived mechanic quantities are plotted below. (middle and right) Squared sound velocity as a function of lateral density for the low frequency case (bold line) and measured in a 5 MHz ultrasonic experiment. For higher frequencies the compressibility decreases, therefore the sound velocity is increased. The parameter h in the wave equation 3.25 introduces these dispersive effects to the theory (from [83]).

From c_p (fig. 3.12 upper left) and equation 3.31 the changes in lateral compressibilities are estimated. These expressions allow the calculation of the squared speed of sound (eq. 3.26) in the low-frequency limit. The data shown in figure 3.12 is approximated using equation 3.26 with

$$v_0^2 = 176.6\,\mathrm{m\,s^{-1}}\ , \quad p = -16.6\frac{c_0^2}{\rho_0^A} \quad \text{and} \quad q = 79.5\frac{c_0^2}{(\rho_0^A)^2}\ . \tag{3.32}$$

The desired solutions are pulses traveling with constant speed and shape $z = x - vt$. Furthermore, the pulses are localized $\Delta\rho^A(|z| \to \infty) = 0$. With these restrictions, the wave equation 3.25 can be solved numerically and analytically [114, 164]. The remaining free parameter h solely scales the width of the pulse. A value of $h = 2\,\mathrm{m^4/s^2}$ produces a decent pulse width of a few centimeters. Depending on their amplitude, the pulse travel between the maximal speed v_0 and a minimal speed

$$v_{\min} = \sqrt{v_0^2 - \frac{p^2}{6q}}\ . \tag{3.33}$$

This minimum speed corresponds to the maximal change in density

$$\Delta\rho_{\max}^A = \frac{|p|}{q}\ . \tag{3.34}$$

Possible soliton profiles are shown in figure 3.13. For DPPC vesicles, the soliton of maximal amplitude propagates with $v_{\min} = 115\,\mathrm{m\,s^{-1}}$. The soliton model can directly explain changes in membrane thickness and length. Heat release and re-absorption is also an intrinsic property.

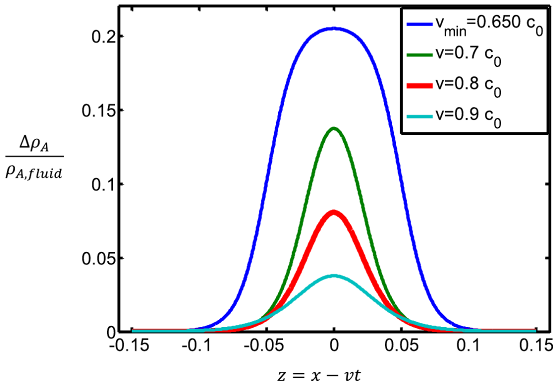

Figure 3.13: Acoustic soliton profiles calculated from the parameters for DPPC membranes. The y-axis denotes relative changes in the area density, and the x-axis denotes the position in a coordinate system that moves with the pulse at the respective velocity v. The soliton with the maximal amplitude propagates with the minimal velocity. With decreasing amplitude, the velocity increases. (from [164]).

Electro-mechanic coupling

The voltage spike of a mechanic Action Potential can be described by piezoelectric effects in the cell membrane [10]. A change in membrane area dA gives rise to a piezoelectric potential

$$V_{piezo} = f_{piezo} dA \; , \tag{3.35}$$

where f_{piezo} is the piezoelectric constant. For an acoustic soliton, the effect is estimated in the range of 10 mV[164] or 50 mV[10].

Changes in the curvature of a liquid crystalline structure can induce a flexoelectric potential [150]. Furthermore, bending can also change the capacity which also induces potential changes, this is covered in the sonophore model. The direct flexoelectricity is outlined first, then the sonophore model is briefly introduced. Flexoelectricity is related to the piezoelectric effect, but instead of the area (in eq. 3.35) a change in curvature $d\zeta$ induces the potential [150]

$$V_{flexo} = \frac{f^D_{flexo}}{\epsilon_0} d\zeta \; . \tag{3.36}$$

The direct flexoelectric coefficient f^D_{flexo} has been measured for locust muscle membranes and rat astrocytes [164]

$$f^D_{flexo,muscle} = 2.5 \times 10^{-18}\,\mathrm{C} \quad \text{and} \quad f^D_{flexo,astrocyte} \approx 1 \times 10^{-20}\,\mathrm{C} \, . \tag{3.37}$$

The geometric changes from bending also change the capacity of the membrane. The total flexoelectric current is the sum of the direct current from equation 3.36 and a capacitive term

$$I_{flexo} = c_m \frac{f^D_{flexo}}{\epsilon_0} \frac{d\zeta}{dt} + (V + V_{flexo}) \frac{\partial c_m}{\partial \zeta} \frac{d\zeta}{dt} \, . \tag{3.38}$$

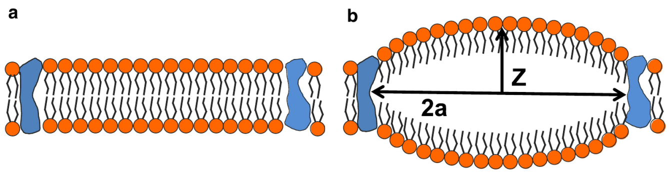

Figure 3.14: Excitation in the NICE model. (a) A lipid bilayer containing membrane proteins. (b) A cavitation is pinned between the membrane proteins which results in local bending (modified from [164]).

The direct effect could enable cells or artificial membranes to sense bending. On the other hand, mechanical changes could arise from the inverse flexoelectric effect, where the curvature

$$\zeta = \frac{f^R_{flexo}}{DK_B}V \tag{3.39}$$

depends on the membrane potential V. Here D is the thickness of the membrane, K_B is its bending modulus and f^R_{flexo} is the inverse flexoelectric coefficient. In this case the membrane behaves like an actuator. These effects could play a role in the displacements that accompany an Action Potential [164]. It can also be applied to the HH theory ([151]) to account for mechanical changes.

Sonophore model Ultrasound can excite neurons [70, 164]. This observation motivated the formulation of the bilayer sonophore model, describing the acoustic modulation of a cell membrane [113]. It predicts the formation of nanobubbles in the intramembrane space at high frequencies ($\approx 1\,\mathrm{MHz}$). The oscillations effectuate mechanic changes like curvature, density and subsequently the capacity of the membrane (see figure 3.14). The capacity change induces a corresponding piezoelectric effect. The bilayer sonophore model yields an expression for the capacitance c_m as a function of curvature. In the HH model, the otherwise constant capacitance can be extended with

$$I_C = V\frac{dc_m}{dt}\,. \tag{3.40}$$

This current is also present in the total flexoelectric current mentioned above (equation 3.38). Equation 3.40 admits functional interaction between the membrane potential and ultrasound. The NICE model combines the HH model with the sonophore model[153]. It can be used to explain acoustic neuromodulation [164].

3.3.5 Action Waves and more

El Hady et al. proposed surface waves that accompany the electric AP[78]. These *Action Waves* explain the displacement as driven by electrostatic forces. Potential energy is stored in the elastic deformation of the membrane, and kinetic energy is transmitted in the intracellular fluid. The Action Wave can also feed back and influence the electrical properties of the AP [78]. More related theories have been proposed recently [138, 165].

4 Collisions and electric interactions of Action Potentials

4.1 Introduction

Action Potentials are signals that run along nerve fibers. When Action Potentials (APs) collide, they annihilate [180, 181]. Such a collision creates a specific extracellular electric potential distribution. The following section provides a detailed description of colliding APs, and demonstrates how such measurements give access to otherwise hidden features of APs.

Direct electric interactions between adjacent neurons are called ephaptic coupling. Such interactions do not require direct connections between the cells, e.g. gap junctions or synapses. However, the effect is especially increased at these tight connections. It is a well known phenomena that must exist independent of other possible mechanisms (e.g. neurotransmitter) [12, 44, 71, 92, 106, 110]. I define the ephaptic discharge Ψ (Psi) to describe the resulting electric effect of colliding APs upon neighboring cells.

The following experiments show that the ephaptic discharge Ψ of colliding Action Potentials is one order of magnitude larger than predicted by the well accepted Hodgkin-Huxley (HH [90, 134, 136]) Model. Another model, the Tasaki Cable (TC [184, 191]) predicts the ephaptic discharge very well. The TC model uses just one free parameter, that adjusts the propagation velocity and is therefore well determined (cf. HH with more than 20 free parameters). To capture the experimental results in more detail, I derived a simple neuron model which I call the Relaxing Cable (RC) model. The RC model is based on the TC model and is fitted to the experimental data by using two parameters. The first parameter adjusts the propagation velocity (as in the TC model), and the second parameter is the relaxation time τ which is directly accessed from the collision experiment. The RC model reproduces all features of the generation, propagation and collision of APs. Most importantly, the predicted ephaptic discharge of both models (TC and RC) matches the collision experiments.

The ephaptic discharge is tightly related to the activating function used to describe e.g. the influence of extracellular electrodes [71, 135, 158, 159]. My hypothesis is that the ephaptic discharge Ψ is controlling the activity, and possibly even plasticity, as a general mechanism in neuronal tissue. The model predicts drastic ephaptic effects not only at collisions, but also at fiber endings e.g. synapses. The proposed framework can explain why the interaction can cause an excitatory or inhibitory effect, depending on the geometry of the connection, and on the timing of Action Potentials.

In addition to ephaptic discharge Ψ and relaxation time τ, the collision experiment yields the characteristic length $\lambda^{\star}$. In contrast to the commonly used λ_0, which is solely a property of the resting nerve, $\lambda^\star$ is a property of the Action Potential [184, 191].

4.2 The origin and effect of extracellular fields

In the following section, analytical expressions are derived to calculate ephaptic coupling. The resulting relations are derived from classical electrostatics (Cable Model, embedded in an Ohmic volume conductor) and are therefore well known. In many textbooks, the cable theory is presented hand in hand with the slightly obfuscating equations of the HH model. A fair description of APs, their extracellular fields and ephaptic interactions does not require such a detailed model of the excitable membrane. The here presented derivation takes particular care to avoid unnecessary assumptions. It is valid for all models that are based on the cable model (e.g. HH model), but it is derived based on the Tasaki Cable (TC) model.

The excitable membrane in the Tasaki Cable model

The Tasaki Cable model is an astonishingly simple approach to describe propagating Action Potentials (APs) [184, 191]. The properties of the membrane may by summarized by the following:

The biological membrane in the resting state has an equilibrium potential of $-100\,\mathrm{mV}$ and a very low conductivity of around $0\,\mathrm{S\,m^{-2}}$ to $10\,\mathrm{S\,m^{-2}}$. If the potential is increased to $-50\,\mathrm{mV}$, the membrane undergoes an immediate transition to the excited state. Then the equilibrium potential is $0\,\mathrm{mV}$ and the resistivity decreases to a value $g^\star$, which determines the propagation velocity and $\lambda^\star$.

Shielding of the electric potential

Before diving into the physics of extracellular fields, a couple of naming conventions are addressed. The quantity that is measured and retrieved from the simulations is the extracellular potential $V_e(\mathbf{r})$ at point $\mathbf{r}$, with respect to a reference voltage. The electric potential is given in the unit volts. The electric field is the derivative of the potential with respect to space, therefore it is given in volts per meter. The term Action Potential addresses a phenomenon, not a potential in the physical meaning. Often the extracellular potential $V_e(\mathbf{r})$ is referred to as the Local Field Potential (LFP), which is a particularly misleading term. A field is not a potential, but the gradient (its derivative with respect to space) of a potential.

The extracellular potential V_e does not originate from the trans-membrane potential V_m itself, because V_m is shielded [18] due to the rather high electrolyte concentration in the extra- and intracellular space. The medium that surrounds neurons contains diverse ions, electrolytes and polyelectrolytes. All charged objects, like cells, accumulate opposite charges around them. As a result, electric fields are shielded on a very short length scale, referred to as the Debye Length λ_D. In physiological conditions, λ_D is around $1\,\mathrm{nm}$ [87]. The membrane potential V_m of a cell in the resting state is around $-70\,\mathrm{mV}$, while the membrane thickness is in the order of $5\,\mathrm{nm}$. The corresponding electric field

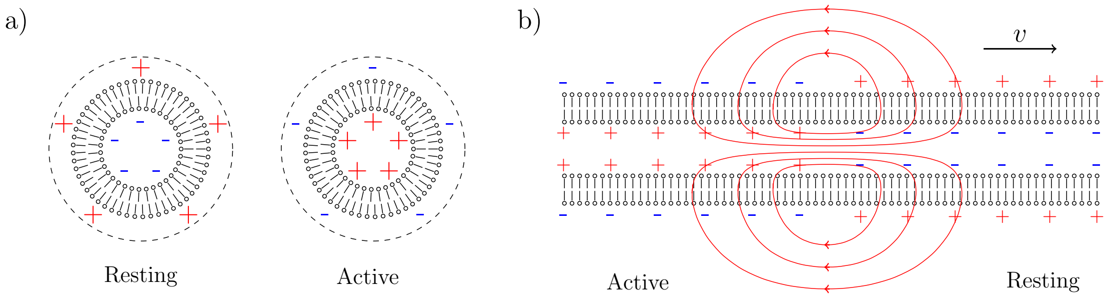

Figure 4.1: **(a)** Symbolic representation of a small cell. The interior is negatively charged in the resting state (left), as indicated by the minus signs. Positive charges accumulate on the outside of the membrane and shield the extracellular field within $\lambda_D \approx 1\,\mathrm{nm}$. In the active state, the electric potential changes its sign but it is still confined. **(b)**. Representation of a nerve fiber, where an Action Potential is traveling from left to right. The boundary between the active and resting state induces an internal current. Since the current flows in a closed loop, there is an external return current that corresponds to a resistive voltage drop along its lines. (The current density across the membrane is j_m in figure 4.2)

across the membrane (including the Debye layer) is therefore around $10^7\,\mathrm{V/m}$! However, this field can not reach into the extracellular medium. It is relentlessly confined within a few nanometer (see figure 4.1 a).

Propagating Action Potentials

The extracellular field arises from a macroscopic extracellular current and corresponds to the resistive voltage drop along the current flow lines [19, 31, 38, 84, 120, 160] The extracellular electric field is a feature of the way Action Potentials propagate. The Action Potential retains its shape and velocity while it propagates, if the axon is assumed to be long and homogeneous. In an inertial frame that moves with the AP, the process is stationary. In front of the AP, the membrane is in the resting state where the trans membrane potential is $V_m = -70\,\mathrm{mV}$. The beginning phase of an AP involves a rapid transition of the membrane potential, up to $30\,\mathrm{mV}$. Since the process is traveling, the rapid temporal change of the membrane potential $V_m(t)$ represents a steep spatial gradient of the potential $V_m(x)$ inside the fiber. Therefore, there is a strong intracellular axial electric field $E_{axial}(x) = \mathrm{d}V_m/\,\mathrm{d}x$. This internal field induces an axial current

$$I_{axial}(x) = \frac{\pi b^2}{\rho_i}\,E_{axial}(x) = \frac{\pi b^2}{\rho_i}\,\frac{\mathrm{d}}{\mathrm{d}x}V_m(x) \tag{4.1}$$

where ρ_i is the specific resistance of the intracellular fluid and b is the radius of the axon [191]. Consider a section $\mathrm{d}x$, than I_{axial} charges up the next section of the axon and drives the propagation of the Action Potential. In this moving frame, the current

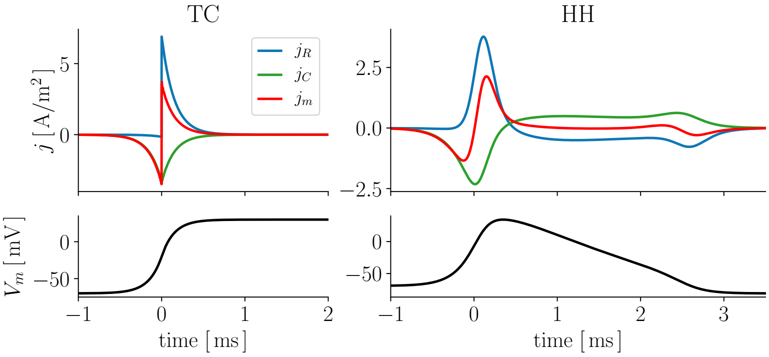

Figure 4.2: Membrane current density j and potential V_m during AP propagation. The resistive j_R, capacitive j_C and total $j_m = j_R + j_C$ current densities are shown in the upper panels. The lower panels show the corresponding membrane potential V_m, according to the Tasaki Cable (TC) model and the Hodgkin Huxley (HH) model, respectively.

flows in a closed loop (see Figure 4.1 b). At each section, a fraction $i_m(x)$ (in $\mathrm{A\,m^{-1}}$) of the internal current leaves the axon and returns outside the fiber. Conservation of charges requires that the total membrane current i_m is the change of the inner current I_{axial} [184, 191], accordingly

$$2\pi b\, j_m(x) = \frac{\mathrm{d}}{\mathrm{d}x} I_{axial}(x) = \frac{\pi b^2}{\rho_i} \frac{\mathrm{d}^2}{\mathrm{d}x^2} V_m(x)\,. \tag{4.2}$$

The second derivative of V_m, which is the concavity of V_m, is proportional to the total membrane current i_m. In the Cable model (see Section 3.1), this total current consists of a capacitive and a resistive current component. For the HH and TC model, the respective current components are shown in Figure 4.2. The current profile $j_m(x)$ along the Action Potential is a dipole and the relevant length scale for the Action Potential is the width of this dipole. It is the width of the steep rising phase of the membrane potential (bottom traces in figure 4.2). The TC theory yields an analytical expression for this width and it is referred to as the active length constant $\lambda^\star$. A fair approximation is given by (eq. 3.7)

$$\lambda^\star = 2\sqrt{\frac{b}{\rho_i\, g_m^\star}}\,, \tag{4.3}$$

where b is the axon radius and $g_m^\star$ is the conductivity (per area) of the membrane in the active state. For the classical giant squid axon, the parameters are $\rho_i = 36\,\Omega\,\mathrm{cm}$, $b = 200\,\mu\mathrm{m}$ and $g_m^\star = 450\,\Omega^{-1}\,\mathrm{m}^{-2}$ [191], in that case $\lambda^\star = 2.2\,\mathrm{mm}$. The active length $\lambda^\star$ is formally similar to the well known passive length constant λ_0. However, $\lambda^\star$ is a function of the membrane conductivity in the active state $g_m^\star$ while λ_0 corresponds to the value in the resting state[1] g_m [184, 191].

---

[1] In a HH model [90], the resistivity in the resting state is mainly caused by the unspecific leakage of the membrane g_l. Other channels are closed and therefore do not contribute much. On the other

The important point is that the current source density j_m (given by eq.4.2) is roughly a dipole with a length $\lambda^\star$ (given by eq. 4.3). This current j_m distributes in the extracellular space which has a specific conductivity $\sigma \approx 0.3\,\mathrm{S\,m^{-1}}$ (or resistivity $\rho = \sigma^{-1}$). The extracellular potential is a result of the resistive voltage drop along the field lines of j_m. It is given by Ohms Law, here the Debye shielding is irrelevant. The exact calculation of the extracellular potential $V_e(r)$ requires knowledge of the spatial distribution of active current sources $j_m(r)$ and the specific conductivity $\sigma(\mathbf{r})$ of the surrounding medium. A simplified standard model of the extracellular medium is the homogeneous, isotropic and purely ohmic volume conductor. Magnetic effects are also neglected and consequently Maxwell's equations reduce to the Laplace equation

$$\nabla^2 V_e = 0\ , \tag{4.4}$$

which may be visualized by a continuous flow of an incompressible fluid. Note that equation 4.4 is somewhat related to equation 4.2. The current source density in the extracellular medium is zero (eq. 4.4), while the current source density of an axon is the membrane current density. The Laplace equation (eq. 4.4) is a linear partial differential equation. Therefore the principle of superposition applies, and the solution to any given distribution of current sources can be expressed as a sum of point sources. The fundamental solution is the potential that arises from a single point source of current I_0. In an isotropic medium the current spreads evenly in all directions. Thus the solution is one dimensional and only depends on the distance r, not on the position $\mathbf{r}$. At a distance r, the current density is diluted to

$$j_0(r) = \frac{I_0}{4\pi r^2}\ , \tag{4.5}$$

it is weighted inverse to the area of a corresponding sphere [92, 120, 135]. Ohms law in continuum form reads

$$\mathbf{j} = \sigma \mathbf{E}, \tag{4.6}$$

where in the one dimensional case $\mathbf{j}_0(\mathbf{r}) = j_0(r)$ and $\mathbf{E}_0(\mathbf{r}) = E_0(r) = \mathrm{d}V_0(r)/\mathrm{d}r$. The extracellular potential $V_0(r)$ of a point source is found by integrating the electric field $E_0(r)$

$$V_0(r) = \int_r^\infty E_0(r')\,\mathrm{d}r' = \frac{I_0}{4\pi\sigma}\frac{1}{r}\ . \tag{4.7}$$

A general solution to equation 4.4 is then expressed as a sum of fundamental solutions (eq. 4.7). If the membrane current density $j_m(\mathbf{r})$ of an arbitrary membrane Ω is known, the resulting extracellular potential is given by [121]

$$V_e(\mathbf{r}) = \frac{1}{4\pi\sigma} \int\limits_{\mathbf{r}'\in\,\Omega} \frac{j_m(\mathbf{r}')}{|\mathbf{r}-\mathbf{r}'|}\,\mathrm{d}\mathbf{r}'\ . \tag{4.8}$$

---

hand, when the membrane is above threshold, other channels open (g_K, g_{Na}) and g_l is negligible. The properties (velocity and collision width etc.) of the AP barely change when the leaking channel is removed from the HH model, but λ_0 more than triples. Both quantities, λ_0 and $\lambda^\star$ are similar functions of the radius b and the inner resistivity ρ_i of an axon. If those values are changed, the effect on λ_0 and $\lambda^\star$ is proportional.

Figure 4.3: Extracellular potential of a propagating AP, using the Hodgkin Huxley model (HH) and the Tasaki model (TC). All traces are calculated using equation 4.9 at different distances d. The scalebar for the middle and bottom traces is 0.5 mV, and the upper scalebar is 0.05 mV. Increasing the distance d causes a decrease and smoothing of the waveform. The bar on the right represents the axon and the dot above it denotes the position of the measuring electrode.

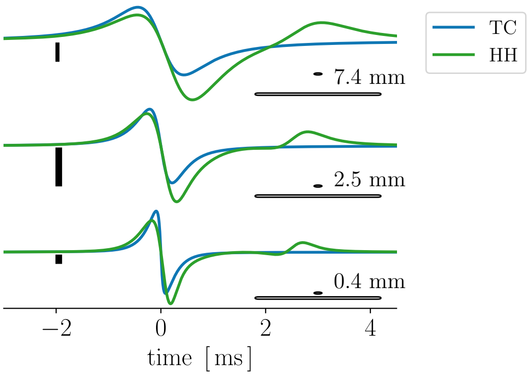

A straight axon has a cylindrical symmetry, thus the extracellular potential depends on the position along the axon x and the lateral distance d. Without loss of generality, the current is described by a line source that spans from x_0 to x_1 at the center of the axon $(d = 0)$. The current density $i_m(x)$ is given by equation 4.2, which leads to

$$V_e(x,d) = \frac{1}{4\pi\sigma} \int_{x_0}^{x_1} \frac{2\pi b\, j_m(x')}{\sqrt{(x-x')^2 + d^2}}\, \mathrm{d}x' \;. \tag{4.9}$$

The integral in equation 4.9 performs a spatial averaging. With increasing distance d the signal is diminished and smoothed, as shown in Figure 4.3. Inversion of equation 4.9 leads to an ill-posed problem. Therefore a direct calculation of i_m from a measurement of V_e is usually not possible. However, when APs collide, a large piece of the axon is activated synchronously. If the measuring electrode is close to the collision site, V_e is virtually proportional to i_m. The observation of collisions thereby enables a unique way to compare measurements of the extracellular potential with neuron models.

Ephaptic coupling

There is a cross-talk between adjacent neurons, that is caused by extracellular electric potential V_e. Electric coupling between cables in a resistive medium is a well understood phenomena. In the context of nerves, it is often referred to as ephaptic coupling [9, 12, 103, 168, 170].

> A subthreshold effect of an action potential on an adjacent fibre must be expected [...] (Katz, 1940 [106])

Calculating the magnitude of the effect does require system-specific parameters that need to be estimated (e.g. the extracellular resistivity distribution). The existence of this coupling, however, is indispensable. The experimental evidence of this kind of interaction and the formalism are well established [44, 69, 92, 106]. I refer exclusively to the effect that is given by equation 4.10 as ephaptic coupling, which is a straightforward and unambiguous definition [71, 92, 135, 159]. [2]

Consider a resting axon (receiver) that is located at the x-axis, and a nearby active axon (sender) that carries an AP. The sender creates an extracellular potential $V_e(\mathbf{r})$, according to equation 4.9. This potential superimposes to the membrane potential $V_m(x)$ of the receiver. An axial current is induced (analog to 4.1), and the corresponding ephaptic membrane current follows [71, 92, 106] (analog to 4.2) with

$$2\pi b\, j_e(x) = \frac{\mathrm{d}}{\mathrm{d}x} I_{axial,e}(x) = \frac{\pi b^2}{\rho_i} \frac{\mathrm{d}^2}{\mathrm{d}x^2} V_e(x)\,. \tag{4.10}$$

The influence of the AP upon its neighbors is determined by the spatial profile of the extracellular potential $V_e(x)$ along the receiving fiber. Namely, it is the concavity of the potential along the receiving fiber. A positive concavity acts excitatory, if strong enough it generates an AP in a resting fiber. A negative concavity on the other hand acts inhibitory, it suppresses the generation of APs [71, 92, 106]. In the case of parallel fibers, an Action Potential causes in initial negative concavity, that is followed by an identical negative concavity. When two APs travel next to each other, the lagging AP is accelerated, while the leading AP is decelerated. As a result, the APs synchronize [106, 170].

The focus of this work is the ephaptic effect of colliding APs. They may collide with another AP, or at the end of a fiber. Therefore, i define the ephaptic discharge

$$\Psi(x) = \int \frac{\mathrm{d}^2 V_e(x,t)}{\mathrm{d}x^2}\, \mathrm{d}t\,, \tag{4.11}$$

which is the integral (in time) over the local concavity (at a fixed position and orientation). The units of Ψ are $\mathrm{V\,s/m^2}$ (wich is equivalent to tesla T). The influence of the ephaptic discharge Ψ upon the membrane potential of adjacent fibers can be estimated by

$$\delta V_\Psi = \frac{b}{2\rho_i c_m}\, \Psi\,, \tag{4.12}$$

similar to the powerful *activating function* in [159]. The “perfect” AP (on an infinite straight fiber) has a symmetric rising phase and therefore cause exactly zero ephaptic discharge [44]. This symmetry is broken when the AP reaches the end of an axon (the axon terminal), or when Action Potentials collide. The following study demonstrates that, while the APs on these fibers disappear they cause a significant ephaptic discharge Ψ in the surrounding tissue [12].

4.3 Methods

Dissection

The experiments in this chapter were performed with the ventral nerve chord (VNC) of earthworms (*Lumbricus terrestris*). Its length of around 10 cm allows recording and

---

[2] The term ephaptic coupling may in some cases not be well defined [103].

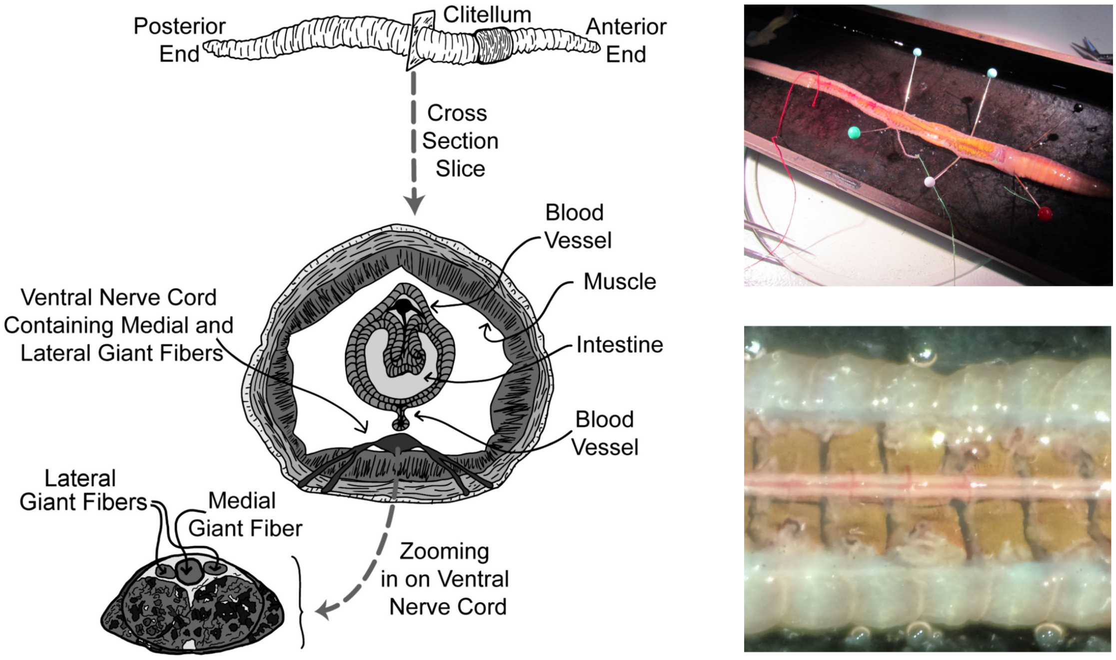

Figure 4.4: (left) Anatomy of an earthworm with zoom on the ventral nerve chord, from [169]. (upper right) Image captured while dissecting the ventral nerve chord, and (lower right) zoom on the nerve chord.

stimulation from multiple well separated sites. Prior to the dissection, the specimen is placed in anesthesia (0.2% butanol in tap water) for 20 min. Then it is pinned in a basin, ventral side facing upwards, and covered with preparation solution (0.04% butanol in saline) (26 mM $NaSO_4$, 25 mM NaCl, 6 mM $CaCl_2$, 4 mM KCl, 1 mM $MgCl_2$, 55 mM sucrose, 2 mM TRIS, pH 7.4 [49]). The dissection starts with a small lateral incision caudally of the clitellum. It is followed by two longitudinal cuts alongside the VNC down to the posterior end. It is important to prevent any intestinal injuries since leakage of digestion enzymes would harm the tissue. Afterwards the middle lappet is removed to lay open about 10 cm of the VNC. Gently pulling up the nerve chord reveals lateral connections which are then cut to disconnect the VNC from the rest of the nervous system. Once completely disconnected, the VNC is placed freely floating in chilled saline and kept at 4 °C for at least 1 h.

Recording chamber

The body of the chamber is made from Polyoxymethylene and contains a row of equidistant silverchloride electrodes (see Figure 4.5, b and c). We used 0.8 mm silver wire, it was abraded, treated with sodium hypochlorite and washed with purified water. The electrodes are placed 8 mm above the bottom of the chamber and separated 5 mm from each other. Before the experiment, all electrodes are stored in saline. The VNC is placed in a recording chamber pre-filled with chilled saline. Then the saline is drained, leaving the VNC resting directly on the electrodes (without touching the side walls or bottom of the chamber). To prevent drying, the chamber is sealed with thin transparent plastic sheets. A small amount of saline is left in the bottom of the chamber in order to maintain a stable humidity. The chamber is encapsulated in a temperature controlled aluminum case, which is connected to a refrigerated circulator set to 12 °C. After the procedure, a VNC can respond for several hours.

Characterization of the sample

The collision experiments (sec. 4.4.2) requires an exact timing of the APs. The VNC incorporates two large nerve fibers, the fast medial giant fiber (MGF) and the coupled lateral giant fibers (LGF). An exact response of both systems is asserted by a strength-latency recording.

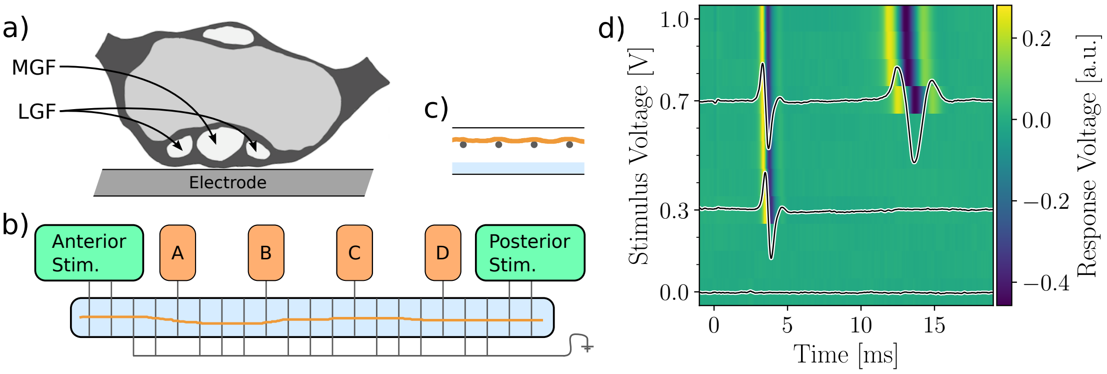

Figure 4.5: Description of the recording scheme. (a) Cross section of an earthworm ventral nerve chord (VNC). The medial and lateral giant fibers (MGF and LGF) are located dorsally and extend from the anterior to the posterior end of the VNC. (b) Top view of a VNC inside the recording chamber. The VNC is supported on parallel electrodes in the chamber. Two stimulators are connected at anterior and posterior ends of the chamber, and four amplifiers (*A* to *D*) are connected to electrodes in between. (c) Side view of the chamber. The specimen is resting on the electrodes without touching the bottom. A small amount of saline keeps the moisture within the chamber. (d) Recordings from a single electrode. The stimulation amplitude was gradually increased from 0 V to 1 V with a fixed pulse width of 0.2 ms. The recorded voltages are color coded and stacked on top of each other, with the corresponding stimulus voltage denoted on the Y-axis. As a visual guide, three individual traces are additionally shown at stimulus amplitudes of 0.0 V, 0.3 V and 0.7 V.

A series of stimulations with increasing amplitude identifies the fibers by their responses shape, threshold, velocity and strength-latency relation (Figure 4.5d). The

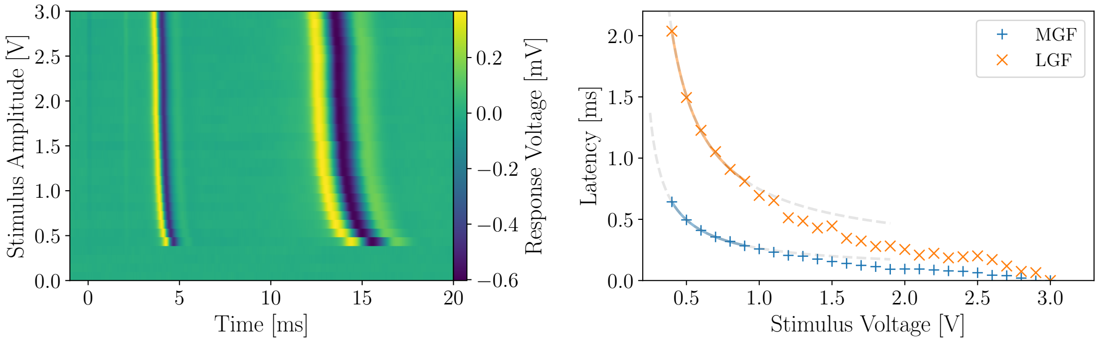

Figure 4.6: Recorded extracellular potential for varying stimulus voltage. In the color coded electric response (left) the two fiber systems can be identified. A short and fast spike from the MGF around 4 ms after stimulation is followed by the slower LGF. The right panel is the latency of the AP as a function of stimulus amplitude. The time of detection is therefore compared to the last therefore fastest response. A fit of equation 4.13 is indicated by the dashed lines.

sharp spike that is detected around 4 ms after the stimuli is the AP on the MGF and the second spike (around 13 ms after stimulation) is the AP on the LGF.

The extracellular stimulus charges up the axon until a certain threshold is reached, then an AP is generated. Once the threshold is reached, the stimulus parameters do not influence the APs shape or propagation, it is said to be *all or nothing*. As a test, single stimuli with a duration of 2 ms are applied with amplitudes ranging from 0 V to 3 V. With a frequency of 0.5 Hz, a total of 31 stimuli are carried out for both sides. Above an amplitude of around 0.3 V both fibers are activated. A recording from electrode C (see Figure 4.5) while stimulating the anterior end is shown in Figure 4.6 left. To compare the signals, their traces are shifted by their latency to coincide. At first 50 Hz noise and its harmonics are removed from raw data by fitting the baseline before and 20 ms after stimulation. Then a first order Savitzki-Golay filter with a window length of 0.2 ms is used for smoothing. Finally the data is interpolated on a GHz grid. The AP from the median fiber has its steepest slope centered between its maximal peak and dip (see Fig. 4.7 top left), this point is chosen as the defined time of arrival. The residual deviation is in the range of a few percent (see Fig. 4.7 bottom). A stimulus amplitude dependent latency is observed. In a simple model, this phenomenon is represented by a charging capacitor [26]. The membrane potential has to reach a certain threshold U_{rh} called rheobase. The time it takes from the onset of the stimulus to the generation of an AP is then

$$t = -\tau \ln\left(1 - U_{rh}/U_0\right) \ , \tag{4.13}$$

with the time time constant τ and the stimulating voltage U_0. A fit of equation 4.13 to the data from stimulations below 1 V (see Fig. 4.6) results in the time constants $\tau_{MGF} = 0.8(1)$ ms and $\tau_{LGF} = 2.0(3)$ ms as well as threshold values $U_{MGF} = 198(19)$ mV

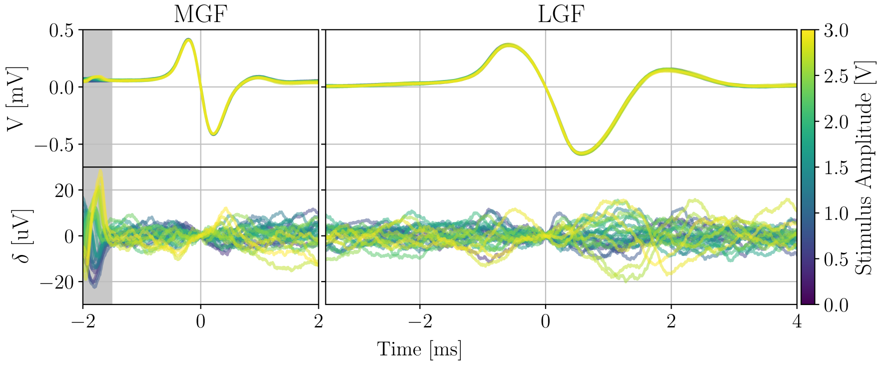

Figure 4.7: The upper panel shows traces of APs after varying the stimulus amplitude from 0.4 V to 3 V. The amplitudes are mapped to trace colors as indicated by the colorbar (right). When corrected for their individual latency, the signals coincide well. Deviations compared to the mean trace are plotted below.

and $U_{LGF} = 240(19)\,\mathrm{mV}$. When stimulating these fibers the crucial difference is the charging time constant, rather than the stimulation threshold. With short stimulation pulses (e.g. 0.2 ms as in Figure 4.5d) the fast charging of the MGF can be utilized to activate the MFG exclusively.

Simulation

The collision experiment is compared to different models of the excitable membrane. The program is written in python, using the versatile and well documented library BRIAN[73, 74]. All models are based on the same multi-compartment cable model with the parameters:

```
diameter = 238.0*2*um
Cm = 1.0*uF/cm**2
Ri = 35.4*ohm*cm
```

The collisions are simulated for a nerve of length 20 cm with 1001 compartments. The axon terminals are 10 cm in length with 1001 compartments. The Hodgkin Huxley model (HH [90]) is used with the classical equations:[3]

```
El = 10.613* mV
ENa = 115*mV
EK = -12*mV
gl = 0.3*msiemens/cm**2
gNa0 = 120*msiemens/cm**2
gK = 36*msiemens/cm**2

eqs = '''
```

---

[3] The HH equations are given in an example at `briansimulator.org`

```
iL = gl * (El-v)              : amp/meter**2
iNa= gNa * m**3 * h * (ENa-v) : amp/meter**2
iK = gK * n**4 * (EK-v)       : amp/meter**2
Im = iL + iNa + iK            : amp/meter**2
I : amp (point current) # applied current
dm/dt = alpham * (1-m) - betam * m : 1
dn/dt = alphan * (1-n) - betan * n : 1
dh/dt = alphah * (1-h) - betah * h : 1
alpham = (0.1/mV) * (-v+25*mV) / (exp((-v+25*mV) / (10*mV)) - 1)/ms : Hz
betam = 4 * exp(-v/(18*mV))/ms : Hz
alphah = 0.07 * exp(-v/(20*mV))/ms : Hz
betah = 1/(exp((-v+30*mV) / (10*mV)) + 1)/ms : Hz
alphan = (0.01/mV) * (-v+10*mV) / (exp((-v+10*mV) / (10*mV)) - 1)/ms : Hz
betan = 0.125*exp(-v/(80*mV))/ms : Hz
gNa : siemens/meter**2
previous_v : volt
'''
```

The variable I is used to apply the stimulus current. Note that here Im is not the total membrane current, but the sum of the resistive currents.

The Tasaki Cable (TC) model is implemented based on [191]:

```
v0 = -100.0*mV
g = 6.8*siemens/m**2

eqs = '''
  I : amp (point current)
  v0 : volt
  g : siemens/meter**2
  Im = g * (v0-v) : amp/meter**2
'''

reset = '''
  v0 = 0.0*mV
  g = 130*siemens/m**2
'''

threshold = 'v > -50.0*mV'
```

If the threshold condition is fulfilled, the reset function is called. Then the axon remains in its excited state. The velocity is matched to the HH model ($13\,\mathrm{m\,s^{-1}}$) by adjusting the conductivity in the active state to $130\,\mathrm{S\,m^{-2}}$. The conductivity in the resting state is set to $6.8\,\mathrm{S\,m^{-2}}$, which is roughly the value that the HH model approaches in the resting state. However, the effect compared to setting it simply to zero is negligible.

I extended the TC model with a relaxation phase that brings the membrane back to the resting potential after excitation. It is referred to as Relaxing Cable (RC) model and implemented via:

```
trelax = 1.4*ms
```

```
v0 = -100.0*mV
gL = 6.8*siemens/m**2

eqs = '''
    I : amp (point current)
    gX = (v0/(100*mV) + 1)**2*(gL1) : siemens/meter**2
    Im = (gL+gX) * (v0-v) : amp/meter**2
    dv0/dt = (-v0-100*mV)/(trelax) : volt
'''
reset = '''
    v0 = 0.0*mV
'''

threshold = 'v > (v0+50.0*mV)'
```

Here the membrane equilibrium potential $v0$ is described by an exponential function. This makes the neuron return to its resting potential after excitation. The increase of the membrane conductivity during the AP is accounted for by adding gX (which is controlled by $v0$) to the membrane conductivity. The extracellular potential is calculated using equation 4.9.

4.4 Results

4.4.1 Annihilation of APs upon collision

Action Potentials can be elicited at different locations along a fiber and propagate in both directions, eventually causing colliding APs. The cable theory (basis of TC, RC, HH, FitzHugh-Nagumo, etc.) requires APs to annihilate when they collide, while other mechanisms (e.g. an acoustic pulse) can allow the penetration of APs [175]. In the first experiments described here, this annihilation is asserted.

In the cable theory (Section 4.2 in particular eq. 4.1), the sharp boundary at the front of the AP drives the propagation. At the boundary, there is an internal electric field E_{axial} that charges up the next section of the axon. Consider a small section dx of the fiber, that is in the resting state, but next to the active state. The internal current charges up the section until a threshold is reached, than the section dx is in the active state and the AP has propagated by dx. Once two boundaries of two opposing Action Potentials merge, there is no boundary along the axon left and therefore there is no internal stimulating current [180] (see figure 4.8). After the collision, the membrane potential at the central point is still close to the peak of the Action Potential, but the spatial distribution of the membrane potential $V_m(x)$ is a smooth function. Therefore, after a collision there is no internal current and no propagation, just relaxation. (It can also be argued that for reasons of symmetry, the internal current must always be zero at the point of collision.)

Thus the cable model can never allow APs to penetrate each other. This annihilation is not at all related to the “refractory period”, however this is still a wide spread misconception [180].

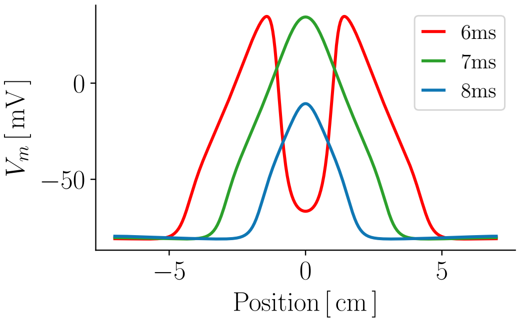

Figure 4.8: Spatial profile of the membrane potential, when APs collide. At $t = 6\,\mathrm{ms}$ the APs are approaching each other. A millisecond later, the steep slopes at the beginning of the APs merged. From this time on, there is no internal stimulating current, therefore no propagation. The APs start to disappear around $t = 8\,\mathrm{ms}$ (calculated with the HH model).

Surprisingly, recent studies claimed that no annihilation takes place [72], reviving discussions about mechanisms of AP propagation [20, 57, 61, 197]. These experiments are linked to fundamentally different theories of nervous signaling, where the AP is described as an acoustic pulse in a thermodynamic framework [10, 83, 175]. Many types of acoustic pulses can of course cross each other, e.g. sound in air. However, it is important to emphasize that acoustic pulses in non-linear media do not necessarily penetrate on collision [175]. The annihilation is not a falsification of the acoustic theory of AP propagation. Some authors explicitly point out the difficulties when working with nerves where more than one axon can be stimulated [57].

In my experiment, the annihilation is verified with an unambiguous experimental procedure. It is ensured that both pulses counter-propagate in the very same nerve fiber. The nerve is connected to two stimulators at its ends and four recording electrodes in between. Action Potentials can travel in both directions along a fiber in the nerve chord and the shape of the spike V_e (as well as the propagation velocity) are almost identical for anterior or posterior stimulation. With an adjusted stimulus intensity and duration, the MGF can be activated while keeping the LGF in resting state (e.g. 0.3 V to 0.6 V, for 0.2 ms as is shown in figure 4.5d). When a fiber is stimulated one-sidedly, the AP propagates along all four recording electrodes and is detected successively (fig. 4.9 left and middle). If both ends are stimulated simultaneously, on each recording site, only the AP arriving first is detected (fig. 4.9 right). The collision itself appears as a sharp spike (on electrode C). There never appears an AP after the collision. This experiment asserts that APs collide and annihilate.

4.4.2 Sweeping the collision

The point of collision can be positioned along the nerve by delaying one of the stimulating pulses with respect to the other. A time delay Δt will displace the point of collision by

$$\Delta x = \frac{v}{2}\Delta t \quad , \tag{4.14}$$

where v is the propagation velocity. A single recording electrode is sufficient to measure the AP at any given distance to the collision. Repeated measurements with varying delay Δt can be visualized as an image where the Y-axis denotes the time delay Δt, see

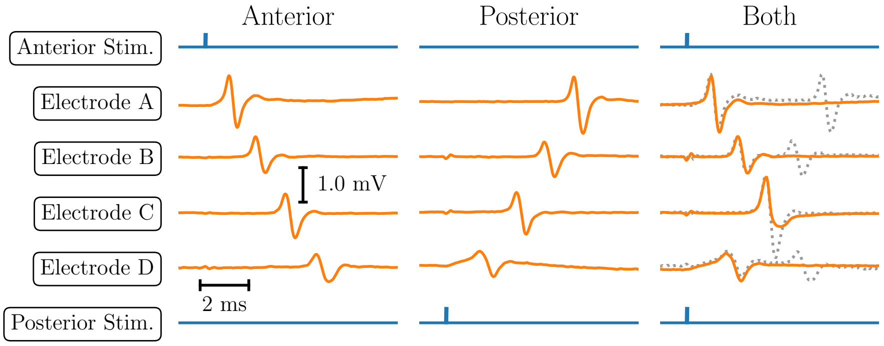

Figure 4.9: Action potentials do not propagate after a collision. Propagation and collision of APs on the medial axon (MGF). The top and bottom line indicate the application of stimuli (0.5 V, scaled by 10^{-3}). (left and middle) Single sided stimulation generates a AP propagating along the medial fiber, which is recorded by the electrodes sequentially depending on the side of stimulation. (right) Stimulating both ends leads to a collision and annihilation of the APs at electrode C. The dashed lines are the sums of the traces in the left and middle panel, that represent the expected signal in case of AP penetration.

figure 4.10. Identification of the fibers based on the delay-sweep images is unambiguous. APs measured in this way also explain how single recordings can be misinterpreted.

In contrast to propagating APs, the collision produces an enhanced peak where the negative phase is considerably diminished. At $\Delta t = 0$ the point of collision is centered on the recording electrode, but when Δt is large, only the AP arriving first is detected on each fiber. When both fibers are activated on both ends, two collisions are detected, at first on the MGF, then on the LGF (figure 4.10 left). Gonzales-Perez et al. claimed APs would penetrate each other[72]. We present the situation, where the LGF was stimulated on both ends, but the MGF stimulation failed on one side. At first glance this may seem like penetrating APs and can easily lead to misinterpretation of the data. Before the APs collide on the LGF, the MGF-AP passes by the oncoming LGF-AP and the external field add up without interacting (figure 4.10 right). This shows that the delay sweep overcomes ambiguities in interpreting the data and provides detailed information about the electric fields along the fibers.

4.4.3 Spatio-temporal shape of the collision

The active phase of the propagating AP is preceded by an internal stimulating current. When those ions can not penetrate a certain position, this current piles up charges inside the fiber. When this happens, the process is no longer stationary and the traveling pair of current source and sink changes. Around the center of the collision, a larger section of the fiber is activated synchronously [180, 188]. As a result the extracellular spike roughly doubles its positive deflection, whereas the negative deflection is smaller but sustained.

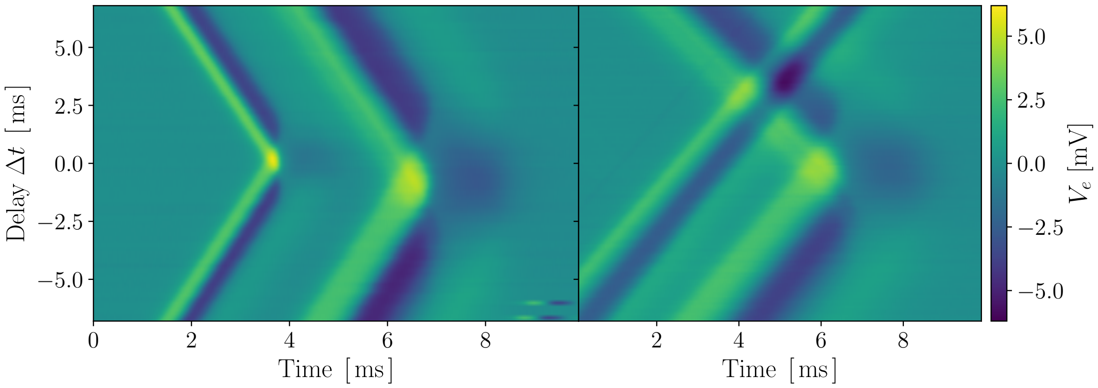

Figure 4.10: A collision experiment in a VNC where both fibers are involved. **(Left) Collision in both, MGF and LGF fibers** The collision at the MGF happens at 3 ms and at the LGF at 6 ms. When the delay Δt is well above 3 ms (or below -3 ms) the collisions are far from the recording electrode and MGF-AP and LGF-AP are detected before they collide. **(Right) Collision in LGF but not in MGF** The image on the right covers the situation where the LGF is stimulated on both ends, but the MGF stimulation failed on one side. The MGF-AP passes by the LGF-AP before it collides. The fact that in the right graph the double sided stimulation failed causes the graph to show a *crossing of APs*. This is solely due to the fact that that the measurement yields the sum of both systems (MFG and LGF). There was no actual crossing within a single nerve fiber.

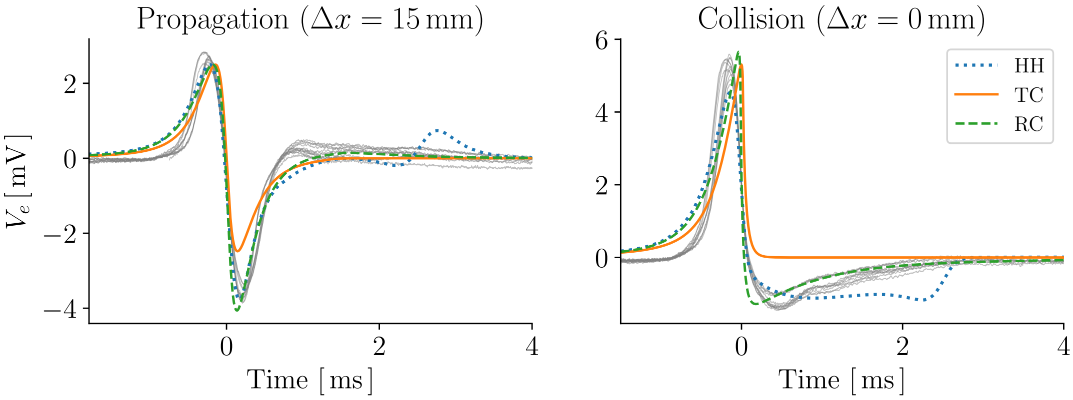

Figure 4.11: Experiment and different simulation models of the extracellular potential V_e for propagating (left) and colliding (right) Action Potentials. The traces are shifted in time to reach the maximal value at $t = 0$ and the amplitude is normalized to the maximal value of the respective propagating AP.

Because of the fact that a larger section of the fiber is in phase, the smoothing effect of the integral in equation 4.9 is decreased heavily. Therefore, the extracellular potential around the collision is a more direct measure of the membrane current. In figure 4.11, the experimental data is compared to simulations. The original form of the TC model does not incorporate the negative deflection of the collision spike [191].

To account for the negative phase, an extension is added to the TC model. The Relaxed Cable (RC) model adds a simple exponential relaxation that brings the membrane properties back to the resting state. A relaxation exponent of 1.4 ms fits well to the experimental trace, as is presented in figure 4.11. Note that the HH model does not fit well at the end of the signal, it shows a superfluous kink.

4.4.4 Quantification of the collision

There is a smooth transformation between the free propagating AP (figure 4.11 left) and the sharp spike of the colliding AP (figure 4.11 right). The shape of the extracellular spike is a function of the distance Δx between the measuring electrode and the point of collision. Both models (HH and TC) show the main features that are observed in the experiment (see figure 4.12). The shape of the AP is quantified by means of the maximal positive V_e^+ and negative V_e^- potential deflection and may be compared to the values of the free propagating AP. In order to quantify the axial spread of the collision, these values (V_e^+ and V_e^-) are plotted against the distance to the collision Δx (see figure 4.13). When the collision is closer than 6 mm to the recording site, a change in the shape is detected. The negative phase is decreased to around 30% for $\Delta x < 3\,\mathrm{mm}$. Closer to the collision, $\Delta x < 2\,\mathrm{mm}$ the positive phase is strongly increased and is maximal at the point of collision. The amplification of the positive deflection V_e^+ as a function of Δx is

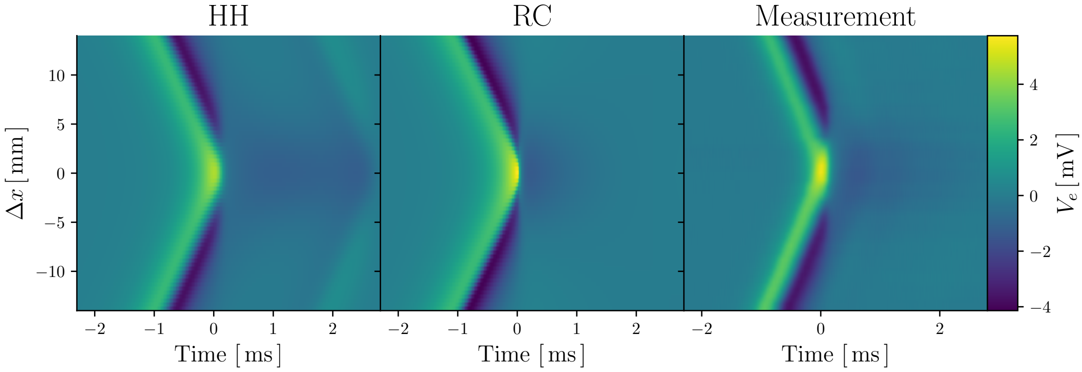

Figure 4.12: Measurement and simulations (HH and TC) of an AP collision. The y-axis denotes the distance between the measuring site and the collision. The X-axis (time) is shifted to the time of collision ($t = 0\,\mathrm{s}$).

roughly gaussian shaped and can be fitted with

$$V_e^+(\Delta x) = V_e^0 + a \exp\left[-4\ln(2)\left(\frac{\Delta x}{\lambda_C}\right)^2\right] , \tag{4.15}$$

where a is the maximal amplification factor, V_e^0 is the maximal value of the propagating AP and λ_c is the full width a half maximum. Equation 4.15 was fitted to the 12 delay sweep experiments shown in figure 4.13. The width of the collision λ_C in an earthworm MGF is thereby found to be

$$\lambda_C = 3.6(3)\,\mathrm{mm} . \tag{4.16}$$

The propagation velocity of the MGF was experimentally determined to be in the range of $13\,\mathrm{m\,s^{-1}}$ to $18\,\mathrm{m\,s^{-1}}$. The TC model was fitted to the data by adjusting just a single parameter. The conductivity of the active membrane $g^\star$ was set to $130\,\mathrm{S/m^2}$ in order to match the propagation velocity of the HH model $v = 13\,\mathrm{m\,s^{-1}}$.[4] The consequent active length constant $\lambda^\star = 4.5\,\mathrm{mm}$ (from eq. 4.3) is well comparable to the here found collision length λ_c.

4.4.5 Ephaptic discharge of colliding APs

Collisions of APs provoke a specific fluctuation in the extracellular potential V_e and may thereby influence neighboring cells. The effect upon the surrounding cells is not a direct consequence of V_e. Based on equations 4.4 and 4.2 the current source density (of the sender) that creates V_e is given by the second spatial derivative, which is the concavity of the membrane potential. In the same way, the concavity of the extracellular potential

---

[4] The HH model has more than 20 parameters, and therefore there are countless possibilities to adjust the propagation velocity. The parameters of the HH model were left unchanged, to enable a direct comparison with other examples in the literature.

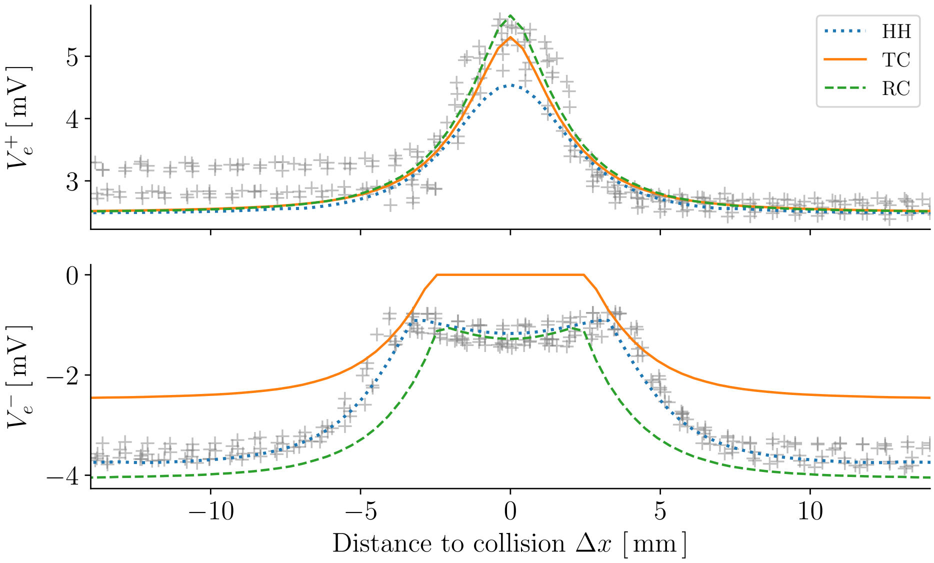

Figure 4.13: The maximal positive (V_e^+, top left) and negative (V_e^- middle left) magnitude of the extracellular potential V_e as a function of the distance to the collision. A “normal” propagating AP (see fig. 4.11, right) is observed for absolute distances $\|\Delta x\| > 10\,\mathrm{mm}$, and at $\Delta x = 0\,\mathrm{mm}$ the APs collide at the point that is the closest to the electrode. The gray crosses are the experimental values, and the simulations are drawn as colored lines, for the Hodgkin Huxley model (HH), the Tasaki Cable (TC) model and the Relaxing Cable (RC) model. At the site of collision, the amplification of the positive peak reaches a factor of around 2 while the negative phase almost vanishes.

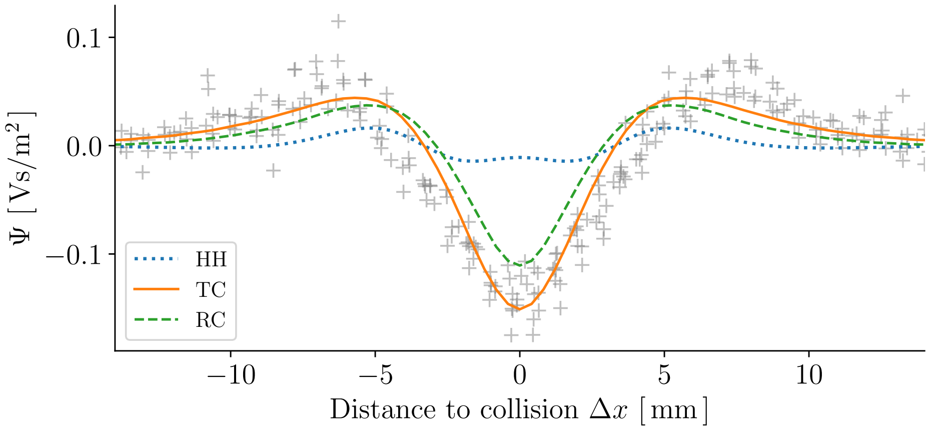

Figure 4.14: Measurement and simulation of the ephaptic discharge Ψ caused by an AP collision and received at a parallel fiber. The x-axis denotes the distance to the collision Δx (which is related to a time delay Δt by eq. 4.14). The discharge Ψ of a propagating AP (e.g. $\|\Delta x\| > 10\,\mathrm{mm}$) is close to zero. A significant ephaptic discharge is observed when the propagation is blocked by a collision. At the point of collision, there is a strong negative discharge (that acts inhibitory) which is surrounded by positive (excitatory) regions. The figure holds experimental data (gray +) as well as simulations using the Hodgkin Huxley (HH) model, the Tasaki Cable (TC) model, and the Relaxing Cable model (the RC model was developed in this thesis).

acts as an ephaptic current source upon the receiver. A positive concavity increases the membrane potential (depolarization), which is excitatory. A negative concavity decreases the membrane potential (hyper-polarization), which is inhibitory [71, 92, 159].

The spatial distribution of V_e is measured by the delay sweep experiment, thus the concavity can be calculated. The transformation from a delay Δt to a spatial coordinate Δx via equation 4.14 requires precise timing of the APs. To calculate the second derivative, the jitter of the AP arrival times must be well below 0.1 ms for dozens of consecutive trigger events and for both APs (anterior and posterior). A precise response is asserted via an strength-latency measurement, as described in the methods Section 4.3. It is important to keep in mind that the concavity of V_e is direction dependent, here the parallel component is accessed (because Δx is the coordinate along the axon). Therefore the result describes the interaction between parallel fibers. The ephaptic discharge of the collision in the MGF is shown in figure 4.14. The ephaptic discharge of the propagating AP (at $\Delta x > 10\,\mathrm{mm}$) is close to zero. For $5\,\mathrm{mm} < \Delta x < 10\,\mathrm{mm}$ there is a small positive ephaptic discharge (which acts excitatory), and for $\Delta x < 2.5\,\mathrm{mm}$ there is a strong negative ephaptic discharge (which acts inhibitory). The ephaptic discharge is in good agreement with the TC and RC models. However, the HH model underestimates the peak of the ephaptic discharge by around one order of magnitude.

4.5 Discussion

Ephaptic effects are often thought to be too weak to have a significant influence in most neuronal systems. However, more and more publications report the opposite [7, 9, 35, 46, 80, 160, 168, 171]. Direct observations of ephaptic coupling go back to at least 1895, and are known to be given by the second derivative of the potential [92, 106].

If the ephaptic discharge of the earthworm MGF is not a rare case, the consequences in other systems would be drastic. Possible implications and consequences are described in the next section. Different geometries are simulated and compared with known biological systems. Finally, a hypothetical relation to higher brain functions is discussed.

4.5.1 Ephaptic discharge at axon terminals

The fibers that grow out of neurons are finite and have a closed terminal. Every AP traveling along such a fiber eventually reaches a terminal. The closed end is a constraint, which forbids intracellular current to leave the segment without crossing the membrane. This situation is similar to a collision.[5] In simulations, the trace of the current density j_m at the point of the collision is identical to the current density at fiber endings. The TC and RC models provide a good match of the ephaptic discharge at the collision, it can be assumed that the predictions at fiber endings are realistic as well.

The ephaptic discharge in the axial projection is intense (fig 4.15 right, and fig. 4.16). Axons often have a thickening at their ends, called the bouton. The effect increases even more when a bouton is included in the simulation (fig. 4.15 and 4.16). The sign and strength of the ephaptic discharge (caused by the axon ending) depends on the position and orientation of a neighboring fiber. If the fibers are parallel and next to each other, the sign of the discharge depends on the position (see fig. 4.15, left). If the fibers are aligned end-to-end, the discharge is excitatory and very strong (see fig. 4.16, right). Excitatory end-to-end connections are common in biological systems. An inhibitory effect is found when the sending axon terminal is at the side of the receiving fiber (see fig. 4.16).

4.5.2 Lateral inhibition

The interaction between neurons is usually described with neurotransmitters.[6] Neurotransmitters are synthesized, stored and released by one cell, another cell that is close by is then somehow affected by these molecules. Some substances act excitatory (e.g. Glutamate), while others act inhibitory (e.g. GABA), the effect is said to depend on the type of receptor [107]. In contrast to these mechanism, ephaptic coupling is derived from first principles [76, 92]. Some phenomena can not be explained by a chemical mechanism. A famous example is the Mauthner cell, an important neuron that coordinates an escape response in fish. It has a contralateral input that causes a fast and strong inhibitory effect and supports the unilateral activation of muscles for the so called "C-start". This

---

[5] Because of symmetry, there can never be an axial current at the point of collision.

[6] Electrical gap junctions are also known [103]. The here proposed hypothesis describes these tight connections in a unified framework of ephaptic coupling.

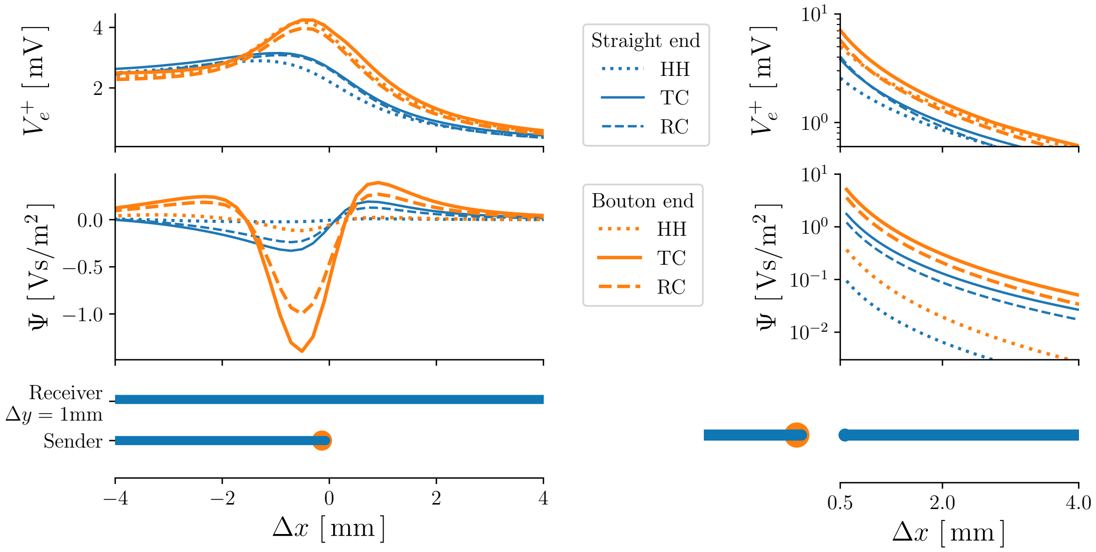

Figure 4.15: Simulation results for the amplification of the positive peak $f^+_{V_e}$ at the axon terminal. The left figure was calculated at a distance $d = 0.2$ mm, whereas in right figure $d = 1$ mm (using equation 4.9). The axon spans from $x = 0$ to $x = -5$ cm and is stimulated at the negative end, so that the AP travels towards the terminal at $x = 0$. A HH (solid lines) and a TC (dashed lines) model were used to generate the AP.

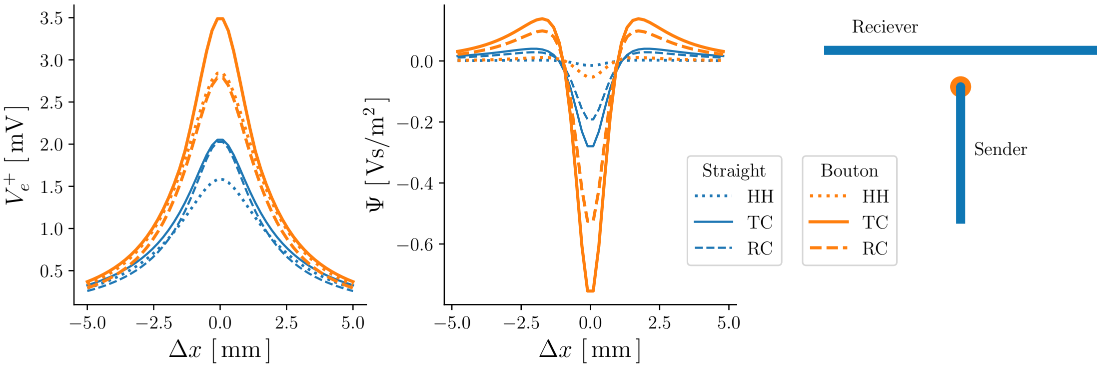

Figure 4.16: Simulation of extracellular potential peak V_e^+ and ephaptic discharge Ψ at an axon-side (axon-shaft) connection. The gap between sending and receiving fiber is 1 mm. This type of connection has an inhibitory ephaptic discharge.

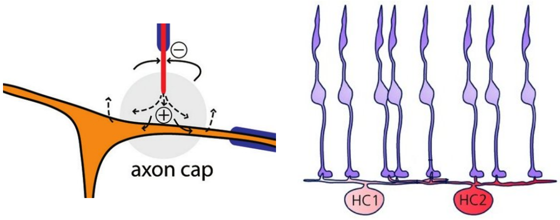

Figure 4.17: Lateral inhibition in biological systems. (**left**) Inhibitory ephaptic connection at the Mauthner cell (orange). The input fiber (red) ends close to the axon shaft. The connection is encapsulated by a highly resistive structure, called the axon cap. The ephaptic discharge of this end-to-side connection is inhibitory, as is shown in figure 4.16. (from [195]). (**right**) Horizontal cells (red) and photoreceptors (purple) in the retina from [33].

effect is known to be of electrical nature [67, 111, 195, 198]. The geometry of this connection is shown in fig. 4.17, left. It is an axon-to-side connection, it's inhibitory discharge is in line with the proposed model (TC and RC in fig.4.16). The connection is embedded in a highly resistive material, called the axon cap. According to equations 4.10 and 4.9, the ephaptic discharge is proportional to the extracellular resistivity. The fact that ephaptic coupling can be drastically increased by increasing the extracellular resistivity is well known [106].

The purkinje cell of the cerebellum (an important brain region for motor control) has a structure called pinceau formation that is similar to the axon cap [100, 194]. Evidence is increasing, that the interaction at this junction can not be of chemical nature [100]. It is also a connection to the shaft of the receiving cell, therefore this fast inhibitory effect can be explained with the proposed framework of ephaptic coupling.

Lateral inhibition is also a so far unexplained mechanism in the very first synapse in the retina of the eye. The output of the retina is inhibited by a layer of so-called horizontal cells which are almost perfectly perpendicular to the photoreceptors (fig. 4.17, right). Despite great efforts, no neurotransmitters have been identified, that could explain this fast inhibitory effect [33, 112]. Again, the geometry explains the observed function in the proposed framework of ephaptic coupling.

4.5.3 The appearance of spines

The observation that end-to-side (axon-shaft) connections are inhibitory and end-to-end (axon-spine) connections are excitatory is very common [22, 29, 108, 110, 117]. Most excitatory synapses in nature are not between an axon end and a straight shaft. Instead, little fibers called spines grow towards the presynaptic neuron resulting in an end-to-end-connection. The ephaptic coupling can explain this geometrical observation. It is independent of the existence of neurotransmitters, it must also act at “chemical” synapses.

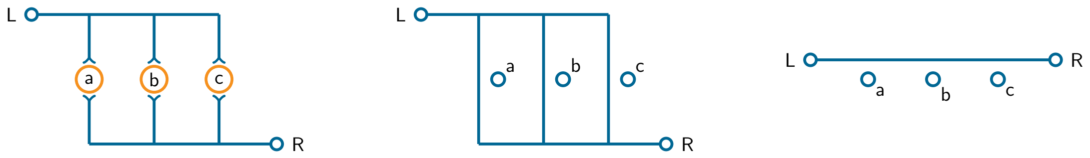

Figure 4.18: Proposed structures to detect time differences between APs. The delay Δt between the input from ears (L, R) is extracted to get the direction to the source. The detector cells (a, b, c) tell if the sound is coming from the left, middle or right direction. (left) The Jeffress Model incorporates special coincidence cells (yellow) that only spike when they are stimulated at two separate sites simultaneously. (middle) By letting the APs collide, the ephaptic discharge on the detector cells depends on Δt. (right) Delay detection using collisions can in principle be achieved within a single branch.

4.5.4 Cross correlation and sound localization

Sound localization in most animals is achieved by measuring differences in arrival times. The two ears detect a sound at different times, t_1 and t_2. The direction to source can be computed from the interaural time difference (ITD) $\Delta t = t_2 - t_1$. E.g. when the sound is coming from straight ahead, the time difference is zero. In mammals, this computation is performed in the superior olivary complex (SOC, a part of the brainstem) which involves the medial superior olive (MSO) and the lateral superior olive (LSO) [60, 77, 193]. This area generates a particularly strong electric field and is often thought to be controlled by ephaptic coupling [13, 71]. The basic concept to “read” Δt is to represent it in a spacial pattern of activation. The location of a collision is nothing else than a direct representation of the time delay, and it provides excitatory as well as inhibitory ephaptic discharge (depending on position, orientation and Δt). Based on the ephaptic discharge around colliding or terminating APs, an interaural time difference (ITD) can be resolved with high precision. The concept of the collision allows the hypothesis of a simplified network structure (see fig 4.18, right), but it is in harmony with all of the proposed structures shown in figure 4.18. Note that collisions are just the most simple possibility to detect the ITD within the proposed framework. The ephaptic discharge at fiber endings is also precisely timed and therefore suitable to detect the ITD between neighboring APs. The difference is that collisions are continuous, while fiber endings represent a discrete ITD.

The most accepted model for sound localization is the Jeffress model, where specialized coincidence cells are only activated when they activated from both ends simultaneously (see fig. 4.18, left). It incorporates only excitatory interaction, which is not the case in real systems [60]. The activity response of cortical neurons in the SOC has been measured as a function of the time delay Δt between APs from different sides. The results often look remarkably similar to figure 4.14 Three characteristic response types

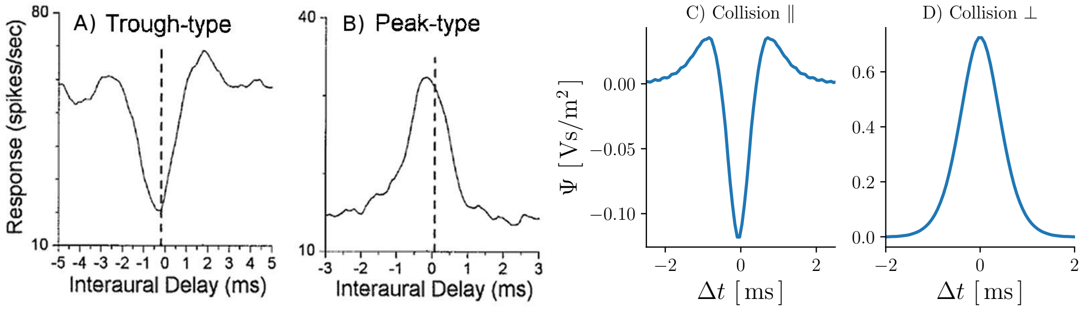

Figure 4.19: (left) Recording from neurons of the auditory cortex of a rabbit (from [60]). A trough-type (A) response is mostly found in the LSO, while a peak-type (B) is common in the MSO. (right) Ephaptic discharge of colliding APs. The receiving fiber is parallel to the sender in (C) and perpendicular in (D).

are observed, peak- trough- and intermediate-type [60, 105, 176]. Peak- and trough-type are symmetric and fit to the discharge of colliding APs. The trough type is similar to figure 4.14, so it fits to a receiver that is parallel to the sender. The peak type is excitatory, and does not show a change of the sign as a function of Δt. Such a response function is found when the receiving fiber is perpendicular to the sender (A shaft-to-end connection[7]). The third type is an asymmetric response, which may be related to a parallel neighboring fiber end (as in figure 4.15 left, in particular the straight end version).

4.5.5 Computation with AP collisions and terminations

An interaction between APs that run along neighboring fibers enables the possibility of computation. These axonal computations have been described by others, but ephaptic discharge or collisions have not been mentioned in these studies [6]. Resolving time differences is the key to perform a cross-correlation of signals. Sound localization is just an arbitrary example for countless very similar computations [105]. One may speculate that AP collision is not an exotic phenomenon. The complex patterns of almost all neurons and the presence of multiple spike initiation zones within one neuron suggest that AP collision is a frequent phenomenon. There are theoretical concept to design a computer based on colliding pulses [2, 102, 157]. The fact that colliding pulses influence neighboring activity makes it possible to postulate a mechanism that performs a discrete computation. Such a mechanism has been proposed for computation in networks of actin filaments [3].

---

[7] The geometry is similar to the one shown in 4.16, but sender and receiver are swapped.

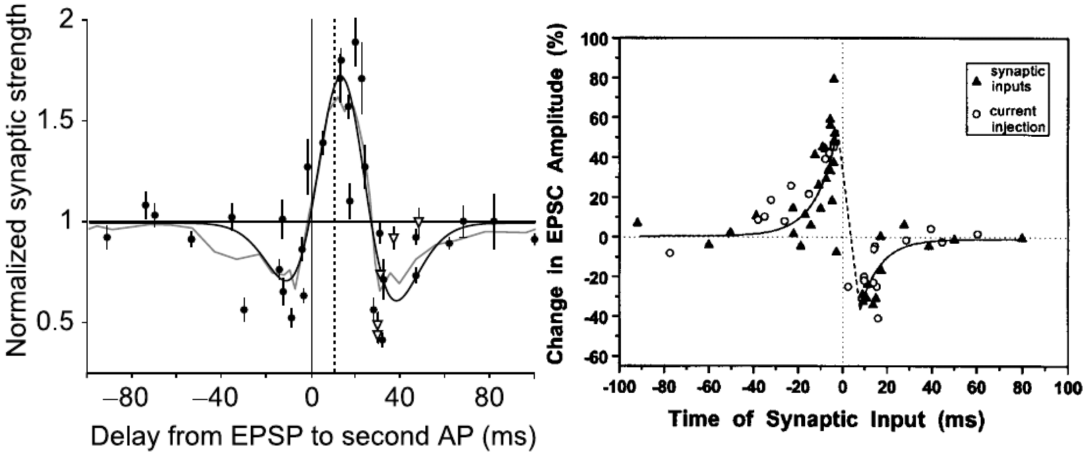

Figure 4.20: The two most prominent types of spike dependent plasticity. A positive y-value means that the synapse increases its strength (potentiation), and a negative value means that the synapse decreases its strength (depression). The x-Axis denotes the time delay between stimulations from opposing sites. EPSP means Excitatory Post-Synaptic Potential, in the left figure it is caused by the first AP. EPSC means Excitatory Post-Synaptic Current, in the right figure it denotes the strength of the synaptic connection. (left from [202], right from [206])

4.5.6 Memory

There are multiple long term effects of extracellular fields that can be interpreted as a structural memory-like mechanism. Extracellular electric fields guide the growth of axons [54, 133], and inhomogeneities of the electric field exert a force upon dipolar or polarizable particles like proteins, enzymes, the centrosome or nucleus [36, 149]. A non zero discharge means that the integral of this force (in time) is not zero. Repeated discharge is therefore expected to act as a sorting mechanism that can influence the morphology of the cell [36].

Structural changes of the connections in a neuronal network are supposed to be the origin of learning and memory. These long term changes are called plasticity, and it is well known that the coincidence of activity has a strong influence on plasticity. More precisely, the plasticity is often found to be a function of the time delay between stimuli from different sides. This is known as spike timing dependent plasticity (STDP) [142, 143, 202, 206]. Again, different response functions (plasticity as a function of the time difference Δt) are observed for different cells. There are two characteristic response functions that are widely observed: An inverted trough-type response (see figure 4.20, left) and an asymmetric response function (see figure 4.20, right) [81].

By comparing fig. 4.20 (left) to fig.4.14 and fig. 4.20 (right) to fig 4.15 (left), one may postulate the following hypothesis: Plasticity is driven by ephaptic discharge. If APs are supposed to collide, this may be seen as a continuous version of hebbian learning. Instead of thinking about discrete coincidence, the collision is a continuous representation of a time delay. At the point of collision, the sending fiber (and surrounding parallel fibers) expire a negative discharge Ψ. This may induce e.g. the formation or potentiation of a perpendicular connection (which is excitatory, see fig. 4.19 right). The symmetry of the response with respect to Δt is a direct representation of the geometrical symmetry of the connection. Analog to Section 4.5.4, the proposed framework does not require collisions. Ephaptic discharge at fiber ending is also a precise representation of a timing. The parallel end-shaft geometry (as in fig. 4.15, left) has an asymmetric discharge $\Psi(\Delta t)$. Such asymmetric spike timing dependent plasticity, are found in biological systems and sometimes is mirrored along the x-axis Δt (e.g. [66]). This can be explained by assuming the alignment of the connection to be mirrored.

4.6 Summary

- Action Potentials annihilate when they collide. This is an intrinsic property of the process of transmission in the non-linear cable equation. The argument that a refractory period is causing the annihilation has been a popular fallacy since the 40s of the last century [180], and it still is until today. Nevertheless, it has been proven wrong [180]. The refractory period refers to a situation where there is a sufficient stimulus, but against the expectation no AP is generated. However, it is the stimulating current itself that vanishes at the collision. There is no reason to expect subsequent generation of an AP anywhere on the fiber. The cable theory is just one way to describe Action Potentials, there are other wave equations that have similar solitary solutions. Those solitons can also annihilate when they collide, even acoustic pulses [173]. Therefore, the observed annihilation does not distinguish between the underlying mechanisms in general.

- The passive length constant λ_0 is often said to be a relevant length scale when APs are investigated. It is a property of a passive liner cable model. However, the AP is a highly non-linear process that is connected to the active length constant $\lambda^\star$ as introduced by Tasaki (TC model) [184, 191]. The propagation velocity of the AP and its length $\lambda^\star$ depend mainly on the resistivity of the membrane in the excited state $g_m^\star$. The passive length λ_0 and the resistivity in the resting state g_m are not essential. This argument is also valid in the HH model, but the HH model does not provide an analytical expression for $\lambda^\star$. The collision sweep experiment provides a way to access the collision length $\lambda_c^\star$ which is a property of the excitation, similar to $\lambda^\star$.

  The measured collision length $\lambda_C^\star$ of the Action Potential in the medial giant axon of the earthworm is 3.6(3) mm. The parameter $g^\star$ in the TC model determines $\lambda_c^\star$ and the propagation velocity.

- Around the site of collision, a comparable large section of the fiber (around $\lambda^\star/2$) is activated simultaneously [180, 188, 190]. In this region, the extracellular measurement is less affected by spatial averaging which enables to observe a roughly mono-exponential relaxation that follows the sharp peak of excitation. The HH model does not resemble a relaxation, but shows a prolonged plateau that ends abruptly (Cole called this aspect of the HH model the *gratuitous bump* [41]).

I extended the TC model with a mono-exponential relaxation function (RC model). The additional parameter τ determines the relaxation time (see fig. 4.11, right) and the depth of the negative extracellular potential at the site of collision ($V_e^-(\Delta x = 0)$ in fig. 4.13). The observed relaxation time and amplitude is reproduced in the RC model with $\tau = 1.4\,\mathrm{ms}$.

The RC model resembles the traces of the potential with more detail. Its purpose is extract a parameter from the experiment, and to demonstrate that this is possible with a simple exponential function. However, it introduces an arbitrary equation into the model and should therefore be avoided if it is not necessary.

- The delay sweep experiments results in a in a high resolution pseudo-spatial potential distribution, recorded with a single electrode. The temporal sum of the second spatial derivative of the potential can be calculated. I call this quantity the ephaptic discharge Ψ and measured a value of around $0.1\,\mathrm{V\,s\,m^{-2}}$. The experimental value is well captured by the TC model (and RC model), while being more than one order of magnitude larger than predicted by the Hodgkin-Huxley model. The consequences of this finding are summarized below.

4.6.1 The impact of the ephaptic discharge

The ephaptic discharge Ψ measures the non-uniformity of the electric field. It is an important quantity because it drives the electric influence upon neighboring cells [44, 92, 106, 159], and it describes a force upon dipolar or polarizable particles (e.g. proteins or enzymes) [36, 148]. Propagating Action Potentials generate negligible or no ephaptic discharge, but the generation or termination (e.g. collision) of APs generates an ephaptic discharge [12]. The magnitude and sign of Ψ depends on position, orientation and timing. It can act positive (excitatory) or negative (inhibitory), a qualitative overview of different geometries is presented in Figure 4.21. I propose the following hypothesis:

1. The strength of Ψ is not limited to the earthworm MGF, but a general property of neuronal activity, as predicted by the TC model. It is relevant especially when fibers are close to each other which is the case at synapses. The geometry of the inhibitory ephaptic discharge matches the synaptic lateral inhibition at the Mauthner cell, Purkinje cell and horizontal cells (fig 4.21, 2a). Also the excitatory effect of axon-spine synapses (fig 4.21, 2c) and the inhibitory effect of axon-shaft (fig 4.21, 2a) fits to this framework (sec. 4.5.2, 4.5.3).

   Besides tight connections, this interaction can be relevant at all length scales up to many millimeters [35, 171].

2. Neuronal tissue uses collisions of APs as a fast and continuous way to transform time difference between APs into a spatial pattern of ephaptic discharge. A fun-

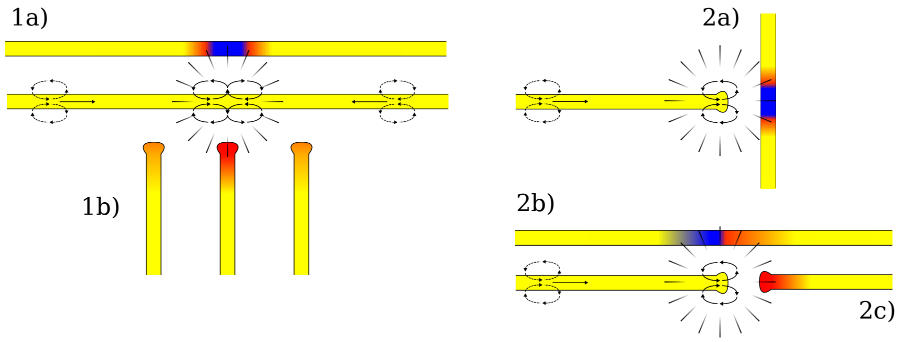

Figure 4.21: Sketch of the ephaptic discharge Ψ around colliding (1, left) and terminating APs (2, right), for parallel and perpendicular geometries. Inhibitory regions are colored blue and excitatory regions are red.

damental way to perform cross-correlation (coincidence detection) and even computing is possible with such a mechanism [2, 3, 102, 157].

Three types of AP timing dependent responses of neuronal activity have been measured in the auditory system (MSO & LSO) [60, 105, 176]. These can be reproduced with different canonical geometries.

3. Repeated discharge induces a sorting of proteins or enzymes that controls the morphology of the membrane. The spike timing dependent plasticity which has been observed [142, 143, 202, 206] can be explained as being controlled by Ψ in the proposed geometries.

4. Ψ can be seen as a magnetic component of neuronal activity, since it is given in T, and value of $0.1\,\mathrm{T}$ is extremely high. An interaction between magnetic and ephaptic effects has been proposed by others [130, 131].

   Especially the neuronal activity in the retina has been shown to be very sensitive to magnetic fields. A functional response has been observed at amplitudes around $10\,\mathrm{mT}$ and at $1\,\mathrm{T\,m^{-1}}$ [122, 129]. The retina is also a possible locus of magnetoreception in certain animals e.g. homing birds [200]. It may be worth to investigate a possible relevance of the strong ephaptic discharge in these systems.

5 Optical signals from lobster nerves

5.1 Introduction

Action Potentials are driven by an excitation of the biological membranes. This process is accompanied by a drastic change in the electrical properties of the membrane [44, 106], as well as thermal [28, 161, 182, 188], mechanical [59, 138, 172, 190] and optical changes [39, 94, 115, 116, 118, 186, 203]. The fast optical changes that accompany the electric AP are referred to as the fast intrinsic optical signal (fIOS) [177]. A better understanding of the optical manifestation of APs is highly desired for diagnostic as well as fundamental scientific purpose. While AP related changes in the optical properties (or fIOS) have been detected with a variety of methods, the origin of these signals remains unclear.

It seems that the strongest signal is measured in the polarization state of transmitted light [14, 15, 32, 39, 62, 63, 186]. The straight-forward approach is a transmission birefringence experiment, where the nerve (aligned at 0°) is placed between two crossed polarizers (aligned at ±45°). The transmitted intensity changes when an Action Potential propagates along the nerve [40, 192]. A nerve chord contains highly anisotropic microscopic structures (e.g. the aligned cell membranes) that cause a considerable static depolarization. The reported relative change of the transmitted intensity is then referred to as the crossed polarized signal (XPS) and is in the order of 10^{-4}. It seems obvious to interpret the XPS as a change in the birefringence [14, 15, 32, 39, 62, 186]. However, more precisely it is a depolarization that can also arise from dichroism, depolarized scattering or geometrical refraction [204].

This section describes a series of laser transmission experiments from electrically stimulated lobster nerve chords, that distinguish possible origins of the fIOS. The theory that underlies classical birefringence experiments is described in Section 2.3. The static optical properties of the lobster nerve chords are characterized with a polarization microscope. The subsequent fast measurements described in this section use a laser as a light source and are based on the detection of modulated light by use of a Lock-In amplifier. When birefringence is measured, the sensitivity of this setup can exceed the straight-forward approach by orders of magnitude (see theory Section 2.3.2). Surprisingly, a fluctuation of the birefringence was never observed. A possible explanation is that the main component of the XPS is not birefringence (which is found in straight transmitted light). Instead the signal may be found in stray light. The central spot of transmitted light is always overlapped and surrounded by a fringe of light that is refracted or scattered at very small angles. In a “normal” birefringence setup, this light is preferably not detected.

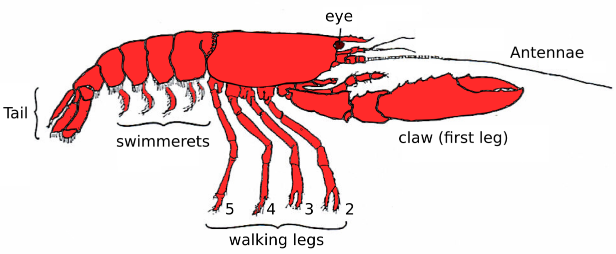

Figure 5.1: Anatomy of a common lobster (*Homarus americanus*). Average specimen are about 30 cm long. Lobsters have five pairs of legs that are around 8 cm long. The first leg holds the large claws. (Figure from [119])

Indeed, an optical signal similar to the XPS was detected in a modified setup, where the unscattered light was blocked. (The modified geometry detects scattering angles from 8° to 0.3°, while the birefringence geometry accepts scattering angles up to only ±0.2°) This rules out birefringence as the cause for the XPS. However, some preparations responded electrically, but no optical signal was observed (even with the modified setup).

5.2 Methods

5.2.1 Electrophysiology

Sample preparation

The anatomy of a lobster (*Homarus americanus*) is depicted in Figure 5.1. The lobster has 4 pairs of walking legs, the leading two end with a movable finger. The first pair of legs holds the large claws. The nerve chords from the second and third leg were used in the experiment described here. Those are roughly 1 mm in diameter. The first leg nerve is around 2 mm in diameter turbid, since the transmitted intensity of the beam decreases exponentially with the thickness of the sample (eq. 2.10). The third leg nerve is thinner that the second nerve and very fragile.

All animals were supplied by the Animal Research Facility (TFA) of the University of Konstanz. The experiments were registered and carried out according to the German animal protection law (TierSchVersV, in particular §39)

Before the dissection, the animals are anesthetized by submerging them in crushed sea ice. After 45 min the lobsters stopped moving and were beheaded with large scissors. The nerves were extracted with the *Furusawa pulling method*[68]. Therefore a leg is removed from its host, close to the body. Then the outermost joint (between carpus and propodus, see Figure 5.2) is broken and the connective tissue (skin and muscle) is cut carefully, while leaving the nerve untouched. The nerve is extracted by gently pulling the propodus apart from the distal part of the leg. The nerve remains connected to the propodus and is thereby pulled out of its shell. After this step, two threads are tied around the endings of the exposed nerve. Finally the sample is removed from the propodus and put in bowl of chilled saline. (The saline is adopted from [63], it contains 525 mM NaCl, 13.3 mM KCl, 12.4 mM CaCl, 24.8 mM MgCl and 5 mM dextrose, after mixing it is adjusted to pH = 7.0 by adding sodium bicarbonate.) After the

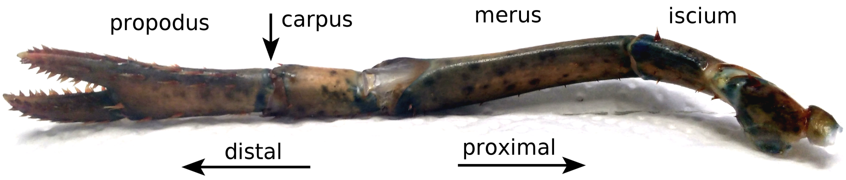

Figure 5.2: The 2nd leg of a lobster, freshly severed from the body. The upper arrow indicates the positions where the joint is broken before pulling the pieces apart.

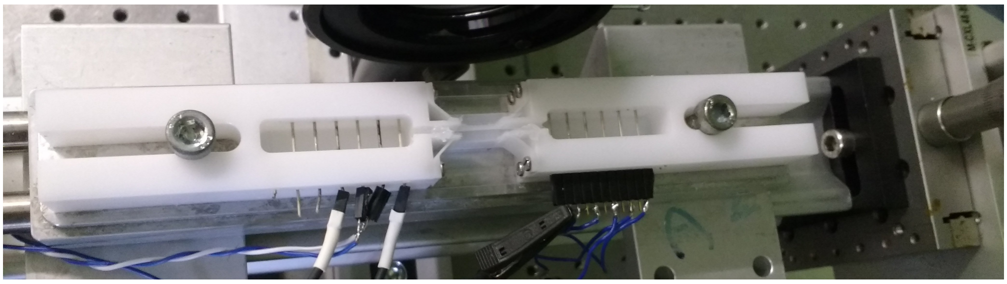

Figure 5.3: The chamber consists of three pieces. Two electrode arrays surround the inner piece, where the nerve chords is in between two cover slips. The pieces are made from Polyoxymethylene (POM) and the chamber can be closed with a lid. It sits on a temperature controlled aluminum base and an aluminum top piece can be used to enclose the whole system, while allowing optical and electrical access.

procedure, the nerve is put in the fridge for one hour.

The nerve chamber

The nerve chamber consists of three pieces, shown in Figure 5.3. The optical properties are observed in the middle, while the outer pieces contain the electrodes for stimulation and recording of the Action Potential. The body of chamber is made from polyoxymethylene (POM) and the two electrode chambers hold 6 electrodes each, spaced by 5 mm. The electrodes are made from silver wire (0.8 mm in diameter around 2 cm long), with a Ag/AgCl surface. In the middle part, the nerve lays in between two microscope cover slips, used as windows. The windows are sealed with petroleum jelly and gently hold in place, to avoid stress birefringence.

Before the nerve is inserted, the Chamber is filled to the top with saline and chilled to 12 °C. Then the nerve is carefully transferred into the Chamber. When the nerve is in position, the section between the glass slides is filled with agarose, to fixate the nerve. To minimize warming and consequent irritation of the specimen, ultra low temperature agarose is used and prepared with saline instead of water. Then a syringe is used to draw the saline from the electrode chambers. When the saline level is well below the

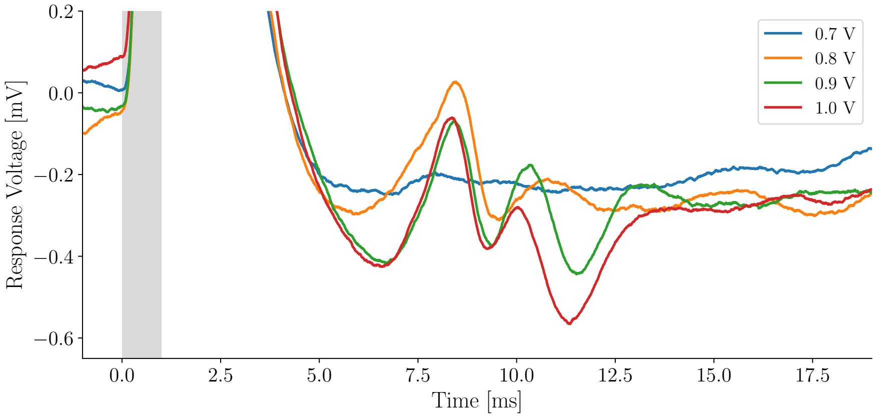

Figure 5.4: Compound Action Potential from lobster nerves with varying stimulus voltage. The first AP is recorded after a stimulus of 0.8 V. More features appear with increasing stimulation amplitude.

electrodes, they are dried with forceps and small pieces of microfiber wipers. Plastic lids and petroleum jelly are used to seal the chamber.

The electric response

The leg nerve of lobsters contains many small, medium and large axons. In general, the stimulation above threshold activates multiple fibers, which is called a compound Action Potential (CAP). With increasing amplitude more fibers join the CAP, as is shown in Figure 5.4. The high salt concentration in the saline can create large stimulation artifacts. Additionally, any residual saline at the recording site diminishes the CAP significantly, by shortening the measuring electrodes. Isolated lobster nerves are very fragile and can only be kept alive for a short time of around 30 min to 90 min. A series of stimulations with increasing amplitude is automated to be run and analyzed in few seconds. This way the characteristic non-linear response caused by the Action Potential can be identified quickly. A successful preparation yields a compound Action Potential with many features. Only few preparations could be electrophysiologically stimulated and recorded long enough to perform meaningful optical measurements. At first, a compound with many features can be seen. Over time the response fades away and after one hour it can hardly be identified at all (see fig. 5.5), which is typical for crustacean nerves [68].

5.2.2 Measuring birefringence with modulated light

The method reported here measures the phase shift $\Delta\varphi$ between the horizontal and vertical components of light. This depolarization is caused by the light transport through the horizontally aligned nerve. The depolarization of unscattered (perfectly straight transmitted) light originates from birefringence, as treated in Section 2.3. The measurement

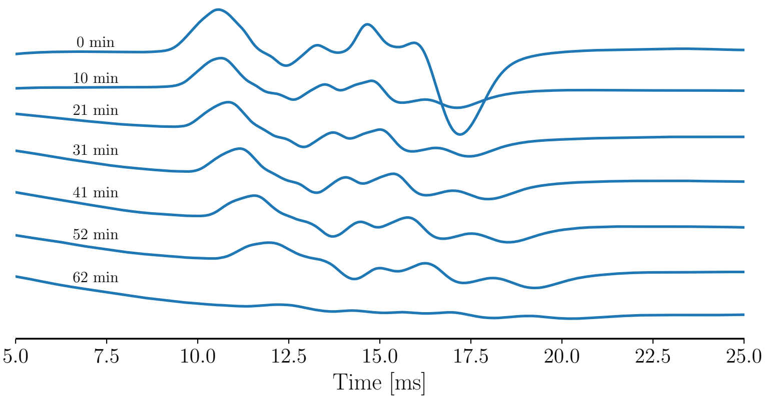

Figure 5.5: Stability of electrophysiological recordings from lobster nerves. The time since the beginning of the experiment is denoted at the beginning of each trace. The top trace was recorded just after transferring the nerve into the recording chamber. The diverse features arise from different axons in the nerve chord. The response weakens with each recording, and after one hour (bottom trace) it is hardly visible.

is based on optical modulation of the phase and consequent demodulation of the signal with a lock-in amplifier (see 5.6). The theory of this method is explained in Section 2.3.2. Light is generated by a Helium-Neon gas laser at 632 nm (from Melles Griot, 10 mW). The beam size and intensity is adjusted with an iris and a neutral density filter. The nerve is resting horizontally and thereby defines the optical axis. Two linear polarization filters (polarizer and analyzer) are crossed at ±45°. In between, there is a photoelastic modulator (*PEM II/FS84* from Hinds Instruments [88]), a Babinet-Soleil compensator and the sample. If the setup is adjusted to sense the straight transmitted light, the detection diode is placed 30 cm away from the sample. The diameter of the diode is around 2 mm and consequently the detected scattering angles are around 0° to 0.2°.

The aim of the experiment is to distinguish birefringence from the depolarization of stray light (scattered or refracted). Therefore, a blocking element is introduced to prevent the straight beam from reaching the detector. The light that is scattered at small angles is focused on the detector instead (see Figure 5.7). This is achieved by placing a lens with a focal length of 75 mm in the middle between the sample and the detector. The unscattered beam is focused into a beam dump with an outer diameter of 0.8 mm. The beam dump is a cannula, coated with carbon black. The so detected light is collected from all angles between 0.3° to 8°.

After placing the nerve in the chamber, the static birefringence of nerve and windows is canceled with the Babinet-Soleil compensator. The lock-In amplifier detects subsequent fluctuations of the birefringence and returns an output voltage

$$U_{LI} = f \cdot \Delta\varphi \; , \tag{5.1}$$

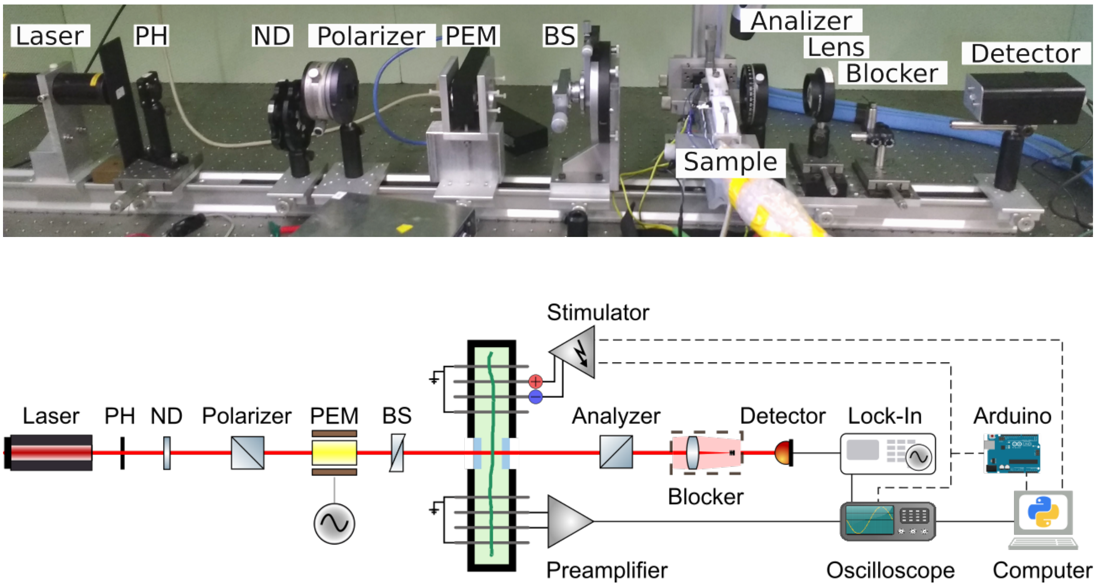

Figure 5.6: The setup for measuring birefringence and depolarized small angle scattering from nerves. A photograph of the setup mounted on the optical table is shown at the top and a sketch of the involved components is drawn below. The parts mounted on the rail are (from left to right): A 10 mW Helium-Neon gas laser followed by a pinhole (**PH**) and a neutral density filter (**ND**) to adjust the beam size and intensity. The light is linear polarized with a Glan-Thompson-**Polarizer** at 45° with respect to the optical axis of the sample, then it passes the Photoelastic Modulator (**PEM**) and Babinet-Soleil Compensator (**BS**). The nerve is enclosed in a temperature controlled nerve chamber which allows electrical and optical access. The nerve chamber can be displaced in x and y, perpendicular to the beam. The **Analyzer** is the second linear polarizer, which is crossed to the first one. When detecting retardance, the light goes directly to the **detector**, a conventional photodiode. When depolarized scattering is measured, an additional blocking element is inserted. It consists of a **lens** and a small beam **blocker** that is positioned in the focal plane of the lens. Then the transmitted light is blocked and only small angle scattered light is focused on the detected. A **Lock-In** amplifier is used to demodulate the optical signal, and a oscilloscope records the electrophysiological and optical data. The experiment is controlled with a python program that runs on the main **Computer**, it interactively controls the stimulation and data acquisition. The triggering is realized with an **Arduino** microcontroller.

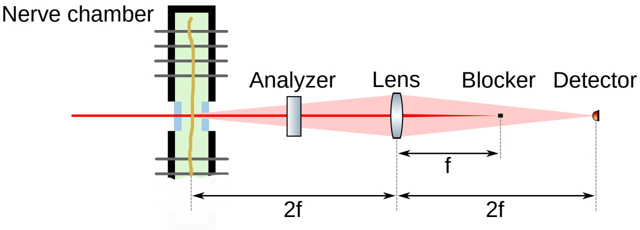

Figure 5.7: The detection optic for measuring depolarized scattering. The Lens focuses the transmitted light into the beam blocker and the scattered light to the diode.

where f is a calibration factor, that depends mainly on the incident intensity, the modulation amplitude and the detection optic. The calibration of f is done with the Babinet-Soleil compensator, and it needs to be repeated when any optical parameters change.

Optimal modulation amplitude

The next section provides an estimation of the optimal modulation amplitude a. It is important to adjust a in order to maximize the signal to noise ratio. The intensity is demodulated by the Lock-In amplifier using a reference signal at a frequency ω. We assume the reference signal to be adjusted in phase with the measured signal. Then the component I_ω can be expressed as

$$I_\omega = \frac{1}{2}\int_0^{2\pi/\omega} \sin(\omega t)\sin^2(\Delta\phi_S + a\sin(\omega t))\,dt\ . \tag{5.2}$$

The measurement sensitivity can be addressed through

$$I_{\Delta\phi} = \frac{1}{2}\frac{\partial I_\omega}{\partial \Delta\phi_S}\bigg|_{\Delta\phi_S=0} = \int_0^{2\pi/\omega} \sin(\omega t)\sin(a\sin(\omega t))\,dt\ . \tag{5.3}$$

Analog to I_ω, the dominating component $I_{2\omega}$ can be measured e.g. to precisely detect or account for fluctuations in the absorption or laser power

$$I_{2\omega} = \frac{1}{2}\int_0^{2\pi/\omega} \sin^2(\Delta\phi_S + a\sin(\omega t))\cos(2\omega t)\,dt\ . \tag{5.4}$$

As long as higher harmonics can be neglected, $I_{2\omega}$ is a good measure of the overall intensity. When prefactors are neglected, the functions $I_{\Delta\phi_S}$ and $I_{2\omega}$ are well known as the Bessel functions of the first kind J_1 and J_2. They are visualized in figure 5.8 (left). In the experiment, the peak of the detected signal I_{Peak} is limited by the range of the detector. The optimal settings result from a trade off between laser power and modulation amplitude. Therefore, the relative signal strength is expressed via

$$\hat{I} = \frac{I_{\Delta\phi_S}}{I_{Peak} + I_{Bg}} = \frac{\int_0^{2\pi/\omega} \sin(\omega t)\sin(a\sin(\omega t))\,dt}{2I_{Bg} + 2\sin^2\left(\frac{a}{2}\right)}\ , \tag{5.5}$$

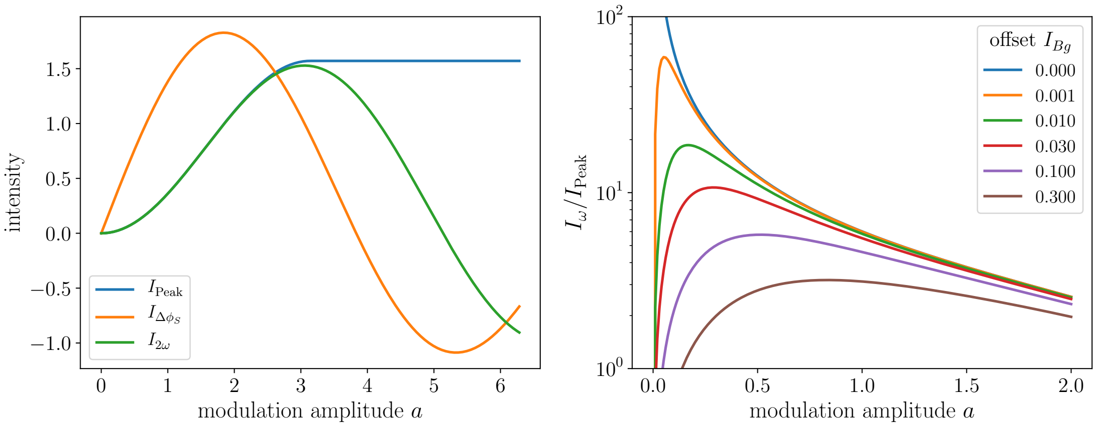

Figure 5.8: (left) The retardance signal strength $I_{\Delta\phi_S}$, the main intensity component $I_{2\omega}$ and the peak amplitude I_{Peak}. (right) The relative signal strength for various offset values.

where I_{Bg} is an offset that accounts for any kind of noise or laser power driven artifacts. Its exact value may not be well determined, however it enables to visualize how the noise I_{Bg} influences the optimal value of a, see 5.8 (right). If the limit of the detector is neglected, the optimal modulation amplitude is at 1.85 rad or 106°, which is the maximum of $I_{\delta\phi_S}$. In the following experiments, an amplitude of $a = 60°$ is chosen.

5.3 Results

Static depolarization

The lobster nerve chord contains many fibers of diverse sizes. These are long structures that are all aligned parallel to each other. This anisotropy of microscopic structures gives rise to a static birefringence. A quantitative measurement of the birefringence is possible by compensation. Therefore the nerve is positioned just below the laser beam, and the signal from the lock-in amplifier is set to zero with the Babinet Soleil compensator. Then the nerve is placed in the beam and the birefringence is compensated again, which yields the birefringence of the sample. For the second leg nerve of the lobster (about 1 mm in diameter) the birefringence is thereby determined to be in the range of 0.1 rad. This strong static birefringence can also be imaged with a polarization sensitive microscope. The commercially available LC-PolScope is a system that measures the alignment of the optical axis and the magnitude of birefringence [145, 146]. The LC-PolScope uses two liquid crystal compensator, tilted by 45° with respect to each other. The software generates birefringence images from a series of light intensity images with varying compensator settings. Figure 5.9 shows the generated birefringence images of lobster nerves (walking leg nerve and small side nerve). As explained in Section 2.3 (eq. 2.49), the retardance is the product of length and birefringence (Δn). The orientation of the optical slow axis is

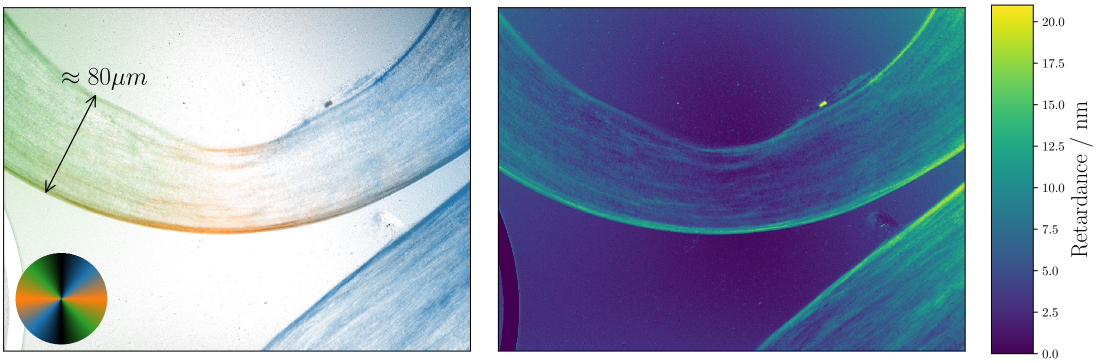

Figure 5.9: Polarization microscopy of a lobster nerve chord. (right) The magnitude of the retardance, where 10 nm corresponds to a phase shift of 0.1 rad. (left) The orientation of the slow axis, where the color is weighted with the magnitude of the retardance. Weakly birefringent pixels appear bright. It can be seen that the slow axis of the optical index is aligned parallel to the nerve chord.

parallel to the nerve chord, and the retardance is in agreement with the value obtained via Babinet-Soleil compensation.

Transient depolarization

The depolarization of the straight transmitted light is caused by birefringence. In this straight geometry, the detector area corresponds to a scattering angle of ±0.2°. A transient depolarization of this light was not detected (see figure 5.11).

The blocking element focuses only the scattered light from the angles 8° to 0.3° to the detector. This geometry detects depolarized small angle light scattering (XSALS). Upon electrical stimulation of the nerve, a phase shift of around 20 µrad is observed (see Figure 5.10). A direct comparison of birefringence and depolarized small angle scattering is shown in Figure 5.11. Therefore, the blocking element was by turns positioned and removed from the beam line. Clearly, the signal is only observed in the scattered light. Each trace in Figure 5.10 and 5.11 is an average of 200 measurements, that were taken with a repetition rate of 1 Hz. Within the total time of around 3 min, the electric signal vanished considerably more quickly than the optical signature of the Action Potential. Therefore only the first electrical recording is shown in Figures 5.10 and 5.11. In consequent experiments, the electric AP was barely recognizable.

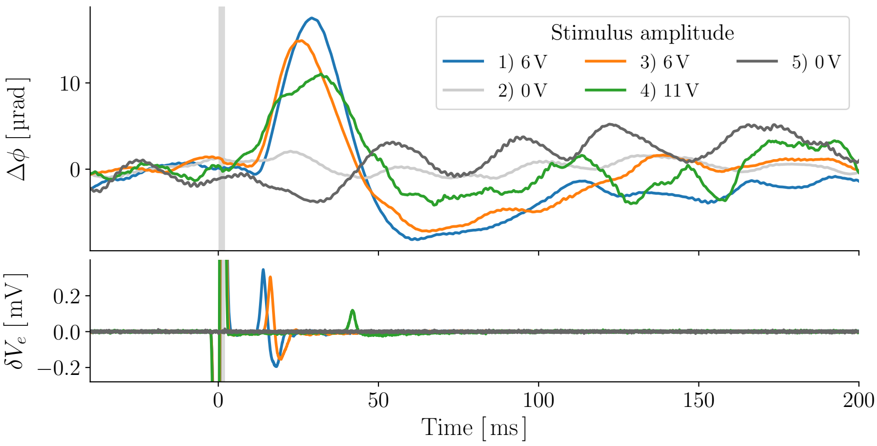

Figure 5.10: (upper panel) A transient fast intrinsic optical signal (fIOS), measured with depolarized small angle scattering (XSALS). The gray bar indicates the time of the electric stimulation. The legend denotes the order in which the measurements were taken, as well as the applied stimulus voltage. The control experiments (line 2 and 5) were performed without electrical stimuli. Each trace is an average of 200 single measurements. (lower panel) The electric recording of the first run (corresponding to line 1).

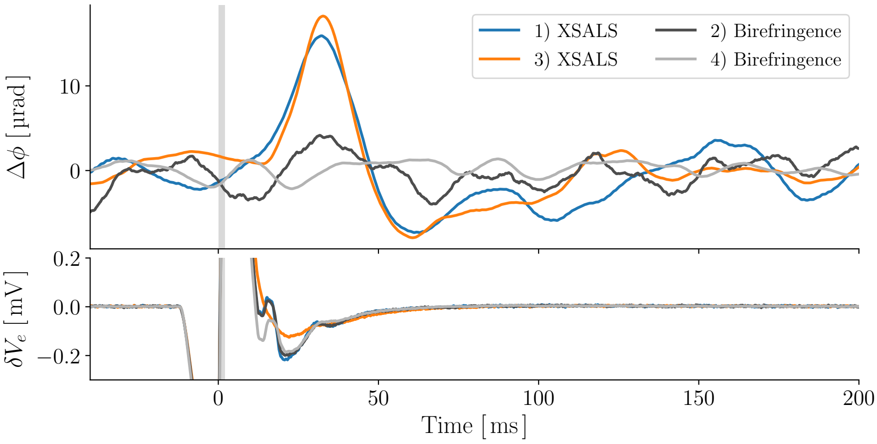

Figure 5.11: (upper panel) Consecutive measurements of depolarized small angle scattering (XSALS) and birefringence. The detection scheme was swapped while keeping other parameter untouched. A fIOS is not detected in birefringence. The legend denotes the order in which the measurements were taken, as well as the detection geometry. Each trace is an average of 200 single measurements. (lower panel) The electric recording of the first run (corresponding to line 1).

5.4 Discussion

Static depolarization

The spatially resolved static birefringence of a nerve chord is presented in Figure 5.9. The retardance is great at the edges of the nerve, but rather weak in the middle of the sample. One might assume that the birefringence is homogeneous and the thickness of the nerve is maximal in the middle. Then the retardance that is caused by the nerve fibers should also be maximal in the middle of the nerve chord. The observation of maximal retardance near the edges of the nerve chord suggests that the nerves fibers themselves are not the main cause for the static retardation. Instead, the outer sheath (epineurium) that surrounds the nerve chord may cause the predominant part of the retardation.

Transient depolarization, the fIOS

The XPS is reported by many as a relative change of transmission in the order of 10^{-4} [14, 15, 32, 39, 62, 63, 186]. If the XPS was caused by birefringence, which is often assumed, it would have been detected in our experiment. The sensitivity (to birefringence) of the method described in this section is by far sufficient. However, a change of the birefringence as part of the XPS has not been detected. [1] In contrast, our data shows that the XPS arises due to AP related changes in the depolarized small angle scattering.

A closer look at the measuring systems can explain the differences of the measured quantities. The transmitted intensity through crossed polarizers can also arise from dichroism, depolarized scattering or refraction. In any transmission experiment, the detector always accepts photons from finite scattering angles. The extend of this effect depends on the ratio of scattered and unscattered photons that are detected. The nervous tissue of lobsters is particularly transparent, because the fibers do not contain myelin. The axons of crustacean nerve fibers are many microns in diameter. This is in the Mie scattering regime and will consequently give rise to very strong forward scattering (see theory Section 2.2.2). The intensity of the resulting speckle pattern is maximal at 0° scattering angle. A small but bright fringe of scattered light surrounds the central spot, it is visible to the eye up to scattering angles around 2°.

The fact that no birefringence was observed is consistent with the observation by Akkin et al. [5], they also reported scattering changes, but no change in the retardance. The observed depolarization may therefore occur as a consequence of a change in the formfactor, which is complicated to calculate for a nerve fiber bundle. However, it

---

[1] If we neglect the fact that birefringence is not the source of the signal, we may compare the measured depolarization with the values reported by others. A crude estimation of the XPS may be given by

$$\frac{T(0.1\,\mathrm{rad} + 20\,\mu\mathrm{rad})}{T(0.1\,\mathrm{rad})} - 1 \approx 4 \cdot 10^{-4}, \tag{5.6}$$

which yields the correct order of magnitude, and is well above the noise of the method described in this section. Note that this approach is invalid in the sense of our interpretation. It would only be correct if the signal was caused by birefringence.

has been suggested to describe the light emitted from the nerve by means of simple geometrical refraction [204]. In the geometrical model, the components of the detected light are calculated via the Fresnel equations. In this model, the swelling of lobster nerves, as for example reported by [5, 101, 188], directly provokes a depolarization. When the straight transmitted light is detected, the scattering signal is consequently compromised by unscattered background light [204].

5.5 Summary

Our experiments suggest that the swelling of a nerve is the most likely cause for an intrinsic optical signal that accompanies the Action Potential. The upper limit for changes in birefringence, is estimated to around 5 µrad. In addition, it may be worth mentioning that we observed a biphasic change in the fluctuation of the depolarization, while most groups reported a monophasic deflection of the XPS [14, 15, 32, 62, 63, 118, 186] (A biphasic shape of the XPS is also seen in [39]). The origin of the XPS or fIOS remains unclear. However, actual changes in the birefringence must be extremely small (or considerably slower than the XSALS), if they exist. These results motivate further studies that are focused on detecting minute changes in light scattering.

6 Cavity amplified speckle spectroscopy from nerve chords

6.1 Introduction

In turbid materials like white paint, milk or nervous tissue, a photon is scattered many times before it leaves the sample and is eventually detected. Such materials appear white, if the absorption is low. Inside the sample, the photons perform a random walk with a step length of $l^\star$. The many paths through the sample add up at the detector, or eye. When coherent light is used, the phase of all paths can add up constructive or destructive. A grainy pattern of random dark and bright spots is observed at the outside, called a speckle pattern. When the scattering particles move, the phase changes and the detected intensity fluctuates. In the same way a change of the index n affects the optical path length. By analyzing the intensity autocorrelation function, microscopic displacements are detected. This method is referred to as Diffusing Wave Spectroscopy (DWS, see Section2.2.4) [124]. The phase of a path is determined by all scattering events along a path. With increasing path length and number of scattering events $\langle N \rangle$, the phase fluctuates faster and faster. The inherent sensitivity of DWS originates from the fact that the sample size L is large compared to the transport mean free path $l^\star$.

The same principle can also be applied to small or transparent samples, where $L/l^\star$ is small. Surrounding the sample with a white material will reflect the light back into the sample and thereby increase the path length. By doing so, the photons accumulate many scattering events before they are detected. This principle of cavity amplified speckle spectroscopy (CASS) has recently been introduced by F. Amblard [75]. The interference of the many reflections increase the sensitivity similar to a Fabry-Perot interferometer. However, in contrast to the classical interferometer, CASS is a random interferometer that is based on the maximal disorder of the light. In this context it is unessential, to have a specific design of the cavity or position of the injection and detection fibers. In a perfect diffuse cavity, the light field is homogeneous and all positions are equivalent, so also the position of the sample is irrelevant. When working with biological samples this is particularly convenient.

The following chapter describes the observation of neuronal activity in a CASS experiment. Therefore, the ventral nerve chord of an earth worm is placed in a optical cavity and the speckle fluctuations are analyzed. The nerve is stimulated electrically, to observe the intrinsic optical signal (IOS) which accommodates neuronal activity. First, the design and fabrication of the cavity is described, and the cavity is characterized with colloidal dispersions (see Figure6.1). Then the ventral nerve chord (VNC) of an earth worm is observed in the cavity while it is stimulated electrically. The VNC is easy to

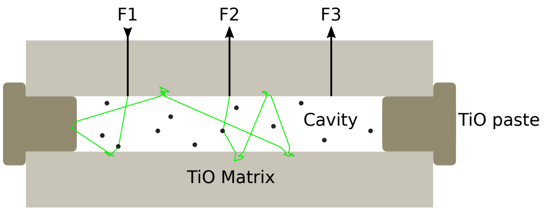

Figure 6.1: A sketch of the cavity filled with a colloidal polystyrene dispersion. The sample is surrounded by the TiO matrix and the ends of the tube are closed with TiO paste. The mono mode fibers F1-F3 are embedded in the matrix and used for the injection and detection of light.

handle, can be kept alive for a long time (typically from many hours to days) and allows the generation and detection of single APs. With a multimode detection scheme, a final fast recording of the IOS is achieved.

6.2 Design of the cavity experiment

A tubular cavity was fabricated inside the nerve chamber to combine electrophysiology with the CASS setup (see fig.6.2). The cavity has a cylindrical hole of diameter 1.5 mm or 0.5 mm, respectively. A nerve can be pulled through the hole and rests on electrodes to record or stimulate on both ends. The cavity is made out of epoxy resin mixed with titania particles at a mass ratio of 2:1. We call this highly scattering material the TiO matrix, it has a mean free path of only a few micron[1]. The body of the nerve cavity is around 14 mm long, 10 mm in width and 8 mm in height. Three optical mono-mode fibers (F1-F3) are integrated in the cavity body and end close to the hole. After insertion of the sample, the cavity is closed with TiO paste (petroleum jelly mixed with titania particles 2:1). The scattering power of the TiO paste is comparable to the TiO matrix material. Light from a green laser ($\lambda = 532\,\mathrm{nm}$ model: torus from Laser Quantum) is injected through fiber F1. The typical laser power is in the range of 250 mW and we estimate the coupling efficacy to around 10%. The intensity is observed through fiber F2 or F3 using a single photon detector (Perkin Elmer SPCM AQR-15-FC) and the autocorrelation function is computed with a hardware correlator (Flex02-12D/C from correlator.com)

6.2.1 Data analysis

There is no model yet to describe the path length distribution of the light inside the cavity. To analyze the experimental data, a stretched exponential function is used in the form

$$G_2(\tau) = \exp\left(-(\Gamma_{str}\tau)^{\alpha}\right) \ . \tag{6.1}$$

---

[1] The transport mean free path of the material was determined by measuring the coherent backscattering cone. From the width of the cone, $l^{\star}$ is calculated. The details of this procedure are given in [4].

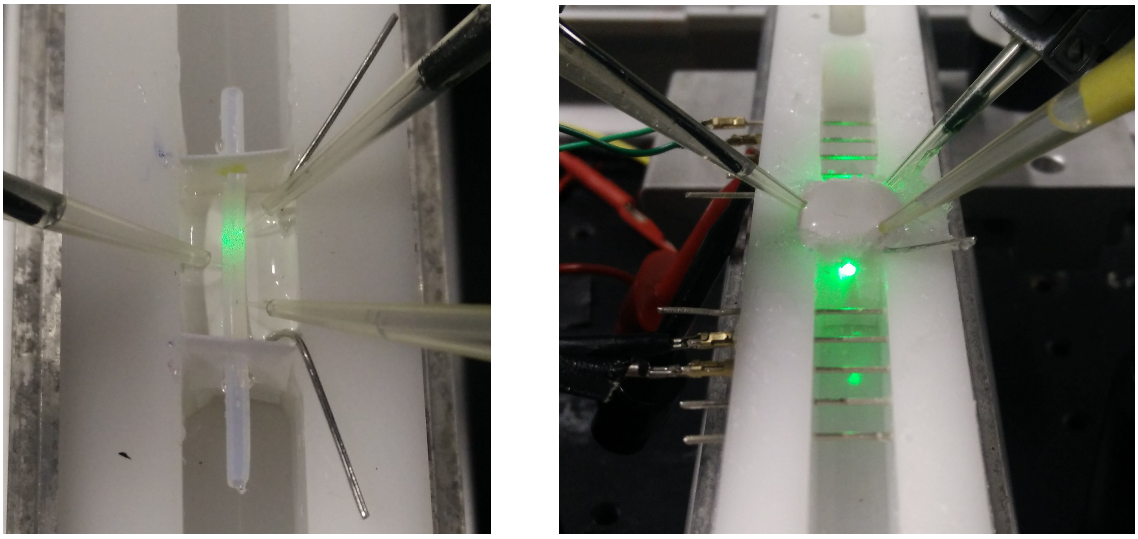

Figure 6.2: Fabrication of the cavity. The 3 optical fibers are guided in pipette tips. The fibers and a plastic tube are embedded in epoxy resin mixed with titanium dioxide particles. After hardening, the tube is removed and the sample is placed in the cavity. The cavity is fabricated inside the nerve chamber that includes electrodes for the stimulation and detection of Action Potentials.

The decorrelation rate Γ is the inverse of the decorrelation time, $\Gamma = \tau_0^{-1}$. The effect of the exponent α is a stretching ($\alpha < 1$) or a compression ($\alpha > 1$) of the distribution of decorrelation times. For a mathematical description of this function see e.g. [53]. The average decorrelation rate is given by

$$\langle\Gamma\rangle = \Gamma_{str}\frac{\alpha}{\Gamma_f(\alpha^{-1})} , \tag{6.2}$$

where Γ_f is the *gamma function*. The error propagation for $\langle\Gamma\rangle$ results in

$$\delta\langle\Gamma\rangle = \frac{\alpha}{\Gamma_f(\alpha^{-1})}\delta\Gamma_{str} + \Gamma_{str}\frac{\Psi(\alpha^{-1}) + \alpha}{\Gamma_f(\alpha^{-1})\alpha}\delta\alpha , \tag{6.3}$$

where Ψ is the *digamma function*, or *polygamma function of zeroth order*. The experimental Data is normalized to and fitted with

$$\hat{G}_2 = (g_2 - 1)/\beta = g_1^2 . \tag{6.4}$$

6.3 Optical properties of the cavity

In the following section the cavity is characterized with polystyrene dispersions as reference samples. First, G_2 of the empty cavity is measured and G_2 of the reference samples

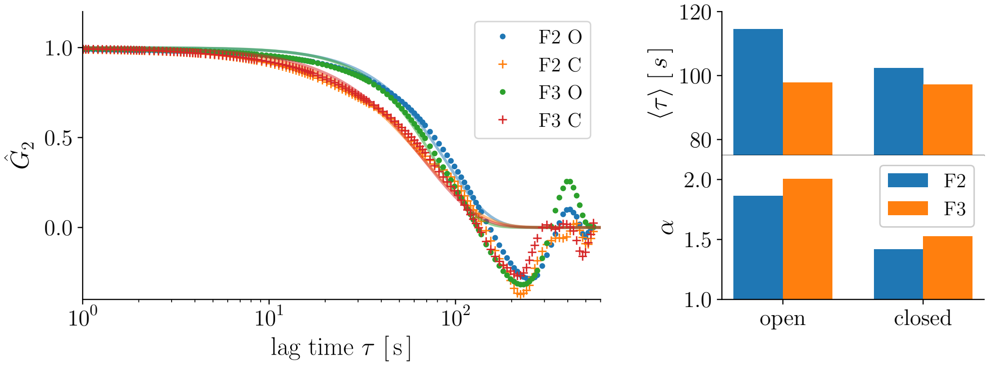

Figure 6.3: Characterization of the empty cavity with diameter 1.5 mm. The correlation functions before (O) and after (C) closing the ends of the cavity with TiO paste are shown on the left. The right panel displays the parameters obtained from fitting the data with stretched exponential functions (where $\langle\tau\rangle = \langle\Gamma\rangle^{-1}$).

is measured in a classical dynamic light scattering experiment. This provides τ_0 of the reference samples. Then the samples are measured in the cavity and the enhancement is defined and calculated for different geometries and concentrations of the reference sample.

6.3.1 Empty cavity

The correlation function is recorded before and after closing the holes with TiO paste. The normalized correlation functions $\hat{G}_2$ are shown in Figure 6.3. Residual motions of the titania particles in the matrix lead to a decorrelation time in the range of 10 s to 100 s. This inherent decorrelation was found to depend strongly on the age of the cavity. Just after the preparation, the decorrelation time $\langle\tau_0\rangle$ is less that a second. Within a couple of days $\langle\tau_0\rangle$ increases to a few minutes. For measurement times longer than $\langle\tau_0\rangle$, the phase is randomized, even if the dynamic of the sample itself is not sufficient to completely decorrelate the phase. This is very convenient, because it ensures the ergodicity of the measurement with non-ergodic samples, like a nerve chord. The decorrelation was measured at two positions (F2 and F3). With a longer distance between injection and detection (F1-F3), $\langle\tau_0\rangle$ decreases, as is expected from a longer path length. Closing the cavity with the TiO paste is expected to increase the occurrence of longer paths and therefore accelerate the decorrelation (as is observed in fig. 6.3). So far, there is no explanation for the compression ($\alpha > 1$) of the decorrelation time distribution measured in the empty cavity.

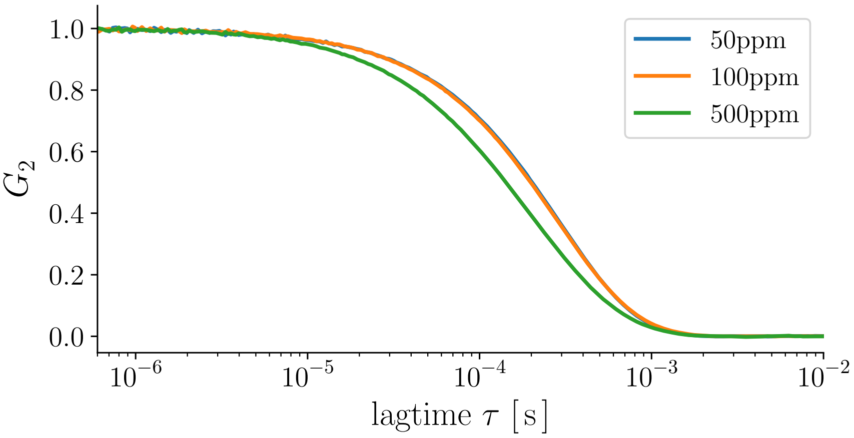

Figure 6.4: Correlation functions $\hat{G}_2$ obtained from the reference samples by dynamic light scattering at a scattering angle of $\vartheta = 90°$. The lower concentrated samples (volume fraction 50ppm and 100ppm) are in the single scattering regime and yield almost identical results. The higher concentrated sample, with a volume fraction of 500ppm, is slightly turbid and therefore multiply scattering but only with few scattering events. Therefore the correlation function of the 500ppm sample is faster and slightly stretched.

6.3.2 Single scattering from reference samples

The reference samples were characterized in a classical dynamic light scattering experiment. Aqueous dispersions of polystyrene colloids with a diameter of 127 nm were used at volume concentrations of 50 ppm, 100 ppm and 500 ppm. The sample was filled in a standard $4 \times 1 \times 1$ cm cuvette and the scattered light was detected at the angle $\vartheta = 90°$. The classical equations 2.31 and 2.32 were used to analyze the correlation functions. For the single scattering samples, the fitted values[2] of the particle radius $r_{50ppm} = 63.8(6)$ nm and $r_{100ppm} = 62.9(7)$ nm are very close to the nominal radius of 63.5 nm. These values correspond to a decorrelation rate of $\Gamma_{DLS} = 1.7$ kHz (and $\alpha = 1$) when fitted with a stretched exponential (eq. 6.2). The higher concentrated sample (500 ppm) is slightly turbid. As a consequence, we measured a faster $\langle \Gamma \rangle = 2$ kHz and slightly stretched $\alpha = 0.9$ decorrelation. From these measurements it is deduced, that $l^\star \gg 1$ cm for the concentrations 50ppm and 100ppm, and $l^\star \approx 1$ cm for the concentration of 500ppm.

6.3.3 Cavity with reference sample

The samples were first observed in classical dynamic light scattering at 90° as discussed in Section 6.3.2. The optically thin samples ensure single scattering in the DLS experi-

---

[2] The uncertainties are calculated with $\delta r = \frac{\partial}{\partial \Gamma}\delta\Gamma + \frac{\partial}{\partial \vartheta}\delta\vartheta$. The estimated standard deviation of the fit parameter $\delta\Gamma$ corresponds to around ± 0.1 nm, and the uncertainty of the scattering angle is estimated with $\delta\vartheta = \pm 0.5°$.

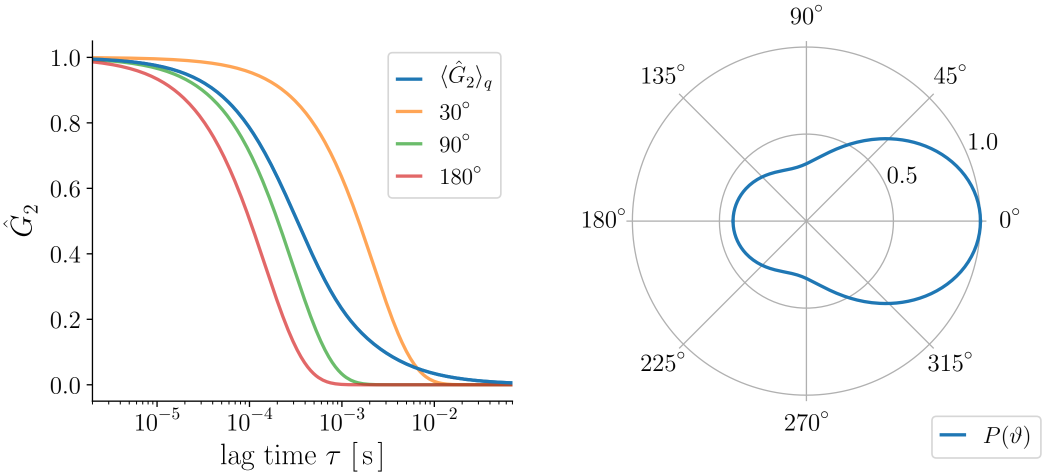

Figure 6.5: Calculated correlation functions $\hat{G}_2$ (left) and Mie form factor (right) for the reference particles with $r = 62.5\,\mathrm{nm}$ (the wavelength is $\lambda = 532\,\mathrm{nm}$). The Mie weighted correlation function $\langle\hat{G}_2\rangle_q$ is the average over all scattering angles, weighted with the form factor $P(\vartheta)$. For comparison, the single scattering correlation functions for $\vartheta = 30°, 90°$ and $180°$ are also shown.

ment and remain in the single scattering regime, even if they are in the cavity. However, all scattering angles can occur in the cavity. Because of the q^2 dependence of the decorrelation time for single scattering, the distribution of decorrelation times is stretched. If it is assumed that the only effect of the cavity is to completely randomize the angle of illumination, than the resulting correlation function

$$\langle g_1(\tau)\rangle_q = \frac{1}{\pi}\int_0^\pi d\vartheta P(\vartheta) e^{-q(\vartheta)^2 D\tau} \tag{6.5}$$

is the superposition of all scattering angles ϑ, weighted with the formfactor $P(\vartheta)$ of the particles. The formfactor is calculated using Mie scattering as described in Section 2.2.2 (see Figure 6.5, right). Note that $P(\vartheta)$ is the unpolarized formfactor, because the orientation of the polarization is also randomized by the cavity. The resulting intensity correlation function $\langle\hat{G}_2\rangle_q = \langle g_1\rangle_q{}^2$ is a non-exponential decay with amplified slow contributions because of the increased forward scattering at low q (see Figure 6.5, right). In the following analysis the calculated function $\langle\hat{G}_2\rangle_q$ is fitted with a stretched exponential[3] (eq. 6.2) to extract the reference decorrelation rate $\langle\,\Gamma\,\rangle_q$. We compare the decorrelation rates from the cavity with the angle averaged $\langle\,\Gamma\,\rangle_q$ and call the ratio

$$\frac{\langle\,\Gamma_{Cavity}\,\rangle}{\langle\,\Gamma\,\rangle_q} \tag{6.6}$$

the enhancement (in decorrelation rate). A selection of the data recorded in the 1.5 mm cavity is presented in Figure 6.6. Even for the strongly diluted sample (50 ppm) the

---

[3] Note that the shape of this function can also be fitted rather well with $G_2(\tau) \propto 1/(1+\Gamma\tau)$.

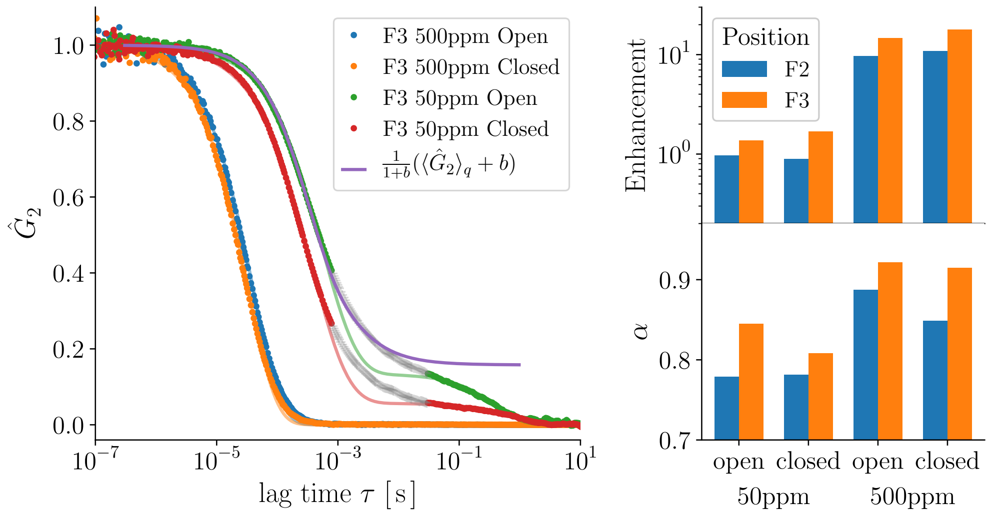

Figure 6.6: Characterization of the cavity with diameter 1.5 mm using the reference sample at concentrations 50 ppm and 500 ppm. The correlation functions and the fitted curves (eq. 6.7) are shown in the left figure. The gray segments of the curves are neglected in the fit because of the non-exponential stretching as is discussed in the text. The omitted stretching is well explained with the angle averaged function $\langle \hat{G}_2 \rangle_q$ (eq. 6.5), as is shown. The right panel presents the parameters obtained from the fit.

decorrelation is dominated by the fast dynamic of the diffusing polystyrene particles, but a slow contribution of the cavity is also present, seen as a shoulder at times greater than 10^{-2} s. Since the timescales are well separated, a combined fit of the data can be performed with

$$\hat{G}_2 = \left(\frac{G_{1,a} + b\, G_{1,b}}{1+b} \right)^2 . \tag{6.7}$$

This means that a part of the light diffuses through the cavity without encountering a scattering event with a particle, while most of the light is scattered at least once. The fit results displayed in the right panel of Figure 6.6 correspond to the fast decorrelation of the PS colloids. For the strongly diluted sample (50 ppm) the enhancement is close to unity and slightly bigger for the longer distance from the same injection fiber F1 to the detection fiber F3. Closing the ends of the cavity with TiO paste does not improve the enhancement significantly. This indicates that the main light losses are not from the open endings of the cavity. The majority of the photons are probably leaving the cavity through the plastic pipette tips that hold the fibers in place[4], and the absorption of the matrix material might also contribute. The sample with a concentration of 500 ppm increases the enhancement drastically and the decorrelation becomes almost mono exponential ($\alpha \approx 1$). This is due to the DWS acceleration, which originates from consecutive scattering events (PS-PS or PS-cavity-PS etc.). With more scattering events, the effective scattering angle is averaged within each path. In the DWS limit a single average scattering angle dictates the decorrelation and G_2 decays close to exponential as observed (see DWS theory Section 2.2.4).

The same samples were used to characterize the 0.5 mm diameter cavity. The data is shown in Figure 6.7. The intrinsic cavity decorrelation is in the same range than the cavity with the bigger bore, again this is optimal for the ergodisation of the measurement. The contribution of the cavity in the correlation function is stronger that in the larger cavity, which is expected because the probability for a photon to be scattered from wall to wall without encountering a particle is larger. Closing the 0.5 mm cavity has slightly larger effect on the enhancement, shown in Figure 6.8. In this cavity the fibers were guided in thin steel capillaries, that ended a few millimeters above the hole. The fibers protruded the capillary ends and ended very close to the hole. Thereby the light losses near the fiber tips should be reduced, which may explain the increased effect of closing the holes.

In conclusion, the enhancement of the cavity for optically thin samples is measurable but not drastic. Light losses may arise from the finite albedo of the matrix material, which needs to be quantified in further experiments. The calculation of the shape of G_2 is difficult, but can probably be done in simulations.

---

[4] Plastic pipette tips were used to fixate the fibers in the 1.5 mm cavity. Optimized fiber guides were used in the 0.5 mm cavity, as discussed below.

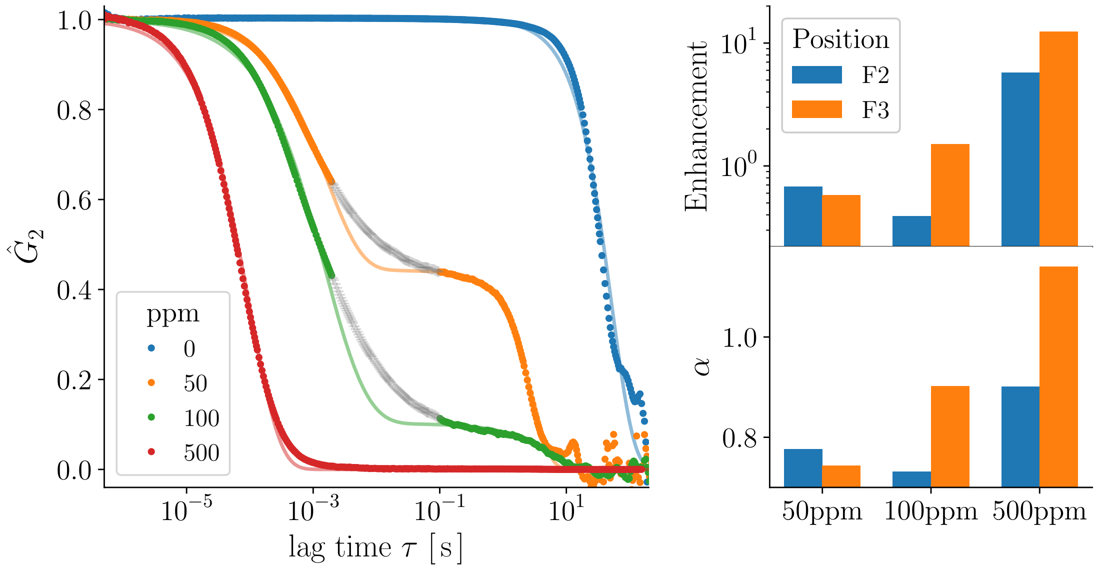

Figure 6.7: Characterization of the 0.5 mm diameter cavity. The correlation function was recorded for the empty cavity and 3 concentrations of the reference sample. Light was injected through fiber F1. The correlation functions and fitted curves for position F2 are shown in the left panel. The gray section are neglected for the fit, and the parameters from the resulting fitted curves are shown on the right.

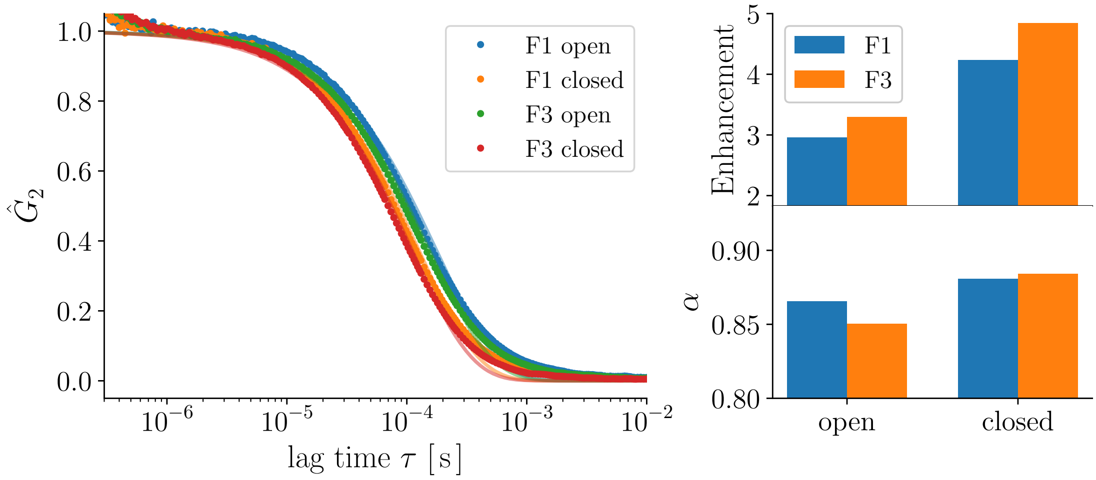

Figure 6.8: Effect of closing the 0.5 mm diameter cavity with the TiO paste. These measurements were performed with the 500 ppm reference dispersion. The middle fiber (F2) was used to shine light into the cavity. The correlation functions and fitted exponential functions are shown on the left. The parameters that are obtained from the fit are shown in the right panel.

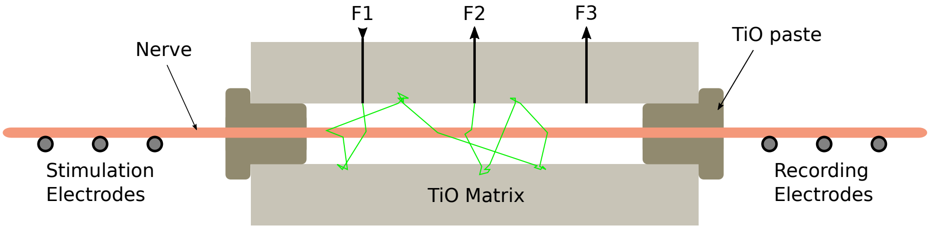

Figure 6.9: Sketch of a nerve chord in the cavity. The nerve chord is resting on electrodes outside the cavity, which are used for the stimulation and detection of Action Potentials. After insertion of the specimen, the holes are closed with TiO paste. Then the complete nerve chamber is closed, in order to prevent the nerve from drying. The optically observed length inside the cavity is about 1 cm.

6.4 Cavity spectroscopy from nerve chords

The ventral nerve chord of an earthworm was placed in the cavity with diameter 1.5 mm, see Figure 6.9. Correlation functions were integrated with a hardware correlator for 60 sec each. The nerve was either resting or stimulated with pulses of 1 V and 1 ms at a repetition rate of 10 Hz. Since the tissue is alive, it is of course not static. In the resting state, the decorrelation is in the order of $3\,\mathrm{s}^{-1}$. Upon electric stimulation, the average dynamic is accelerated by more that a factor of 2 (see Figure 6.10). However, the actual duration of the optical activity of the Action Potential is unknown. If the optical activity is estimated to last for 1 ms to 10 ms, the effective duty cycle would be 1 % to 10 %. Hence, the acceleration is surprisingly strong. The convincing signal to noise ratio demonstrates that this method is well suited to study the dynamics of nerves and to quantify the intrinsic optical changes upon electric stimulation.

6.5 Multi mode cavity spectroscopy

The study of fast temporal changes in the dynamic is limited in a mono-mode setup. The hardware correlator integrates the intensity autocorrelation function for a finite time T which needs to be large compared to the total decorrelation time τ_0 of the phase (e.g. $T = 60\,\mathrm{s}$ in Figure 6.10) Changes that are faster then the integration time contribute to the decorrelation but are not resolved in real time. By detecting many uncorrelated speckles the averaging is not only performed in time, but also in space [37, 99]. To explore a faster optical activity we integrated a multi-mode detection scheme. We placed a multi mode fiber alongside the nerve into the hole of the 0.5 mm cavity. The many hundred independent speckle spots are detected with a camera (Basler acA1300-200um). Afterwards, the correlation functions are generated from the movie.

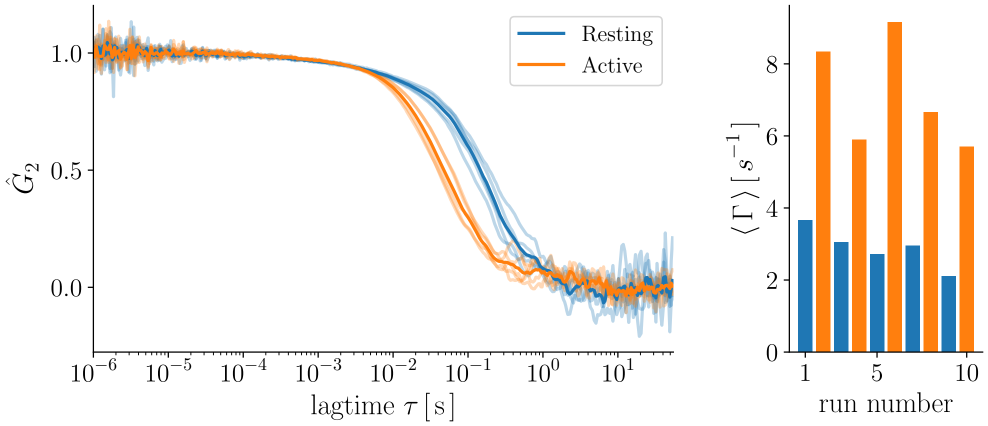

Figure 6.10: Autocorrelation functions $\hat{G}_2$ of an earthworm nerve cord in the 1.5 mm diameter cavity without and with electric stimulation. Each measurement was integrated for 60 s, and the stimulation (pulses of 1 V, 1 ms with 10 Hz) was applied every second run. The solid lines are the average over the single measurements. The panel on the right shows the average decorrelation rates $\langle \Gamma \rangle$ obtained from fitting a stretched exponential function to each single measurement.

6.5.1 The fIOS

The VNC has only two giant axons, it allows to have a precise control and detection of single APs. This is required, when the fast IOS and its correlation with the phase of the electric AP is of interest. Crustacean nerves like the ones used in Section 5 contain many fibers that have different propagation velocities and thereby prohibit a direct correlation with the phase of the electric signal.

To detect the fast signal, a camera with the framerate set to 1 kHz was used. The AP was generated with a repetition rate of 10 Hz and 1000 records were averaged. The experiment was repeated with the stimulus trigger shifted by 5 ms. Correlation of the images was calculated for the lagtimes 1 ms to 6 ms. The results are shown in Figure 6.11. In this preliminary design, the high framerate lead to a considerable reduction of the signal to noise ratio. To minimize the noise, all lagtimes are averaged to a single correlation curve in an additional panel in Figure6.11 on the right.

So far we can not detect the direct manifestation of the electric AP ($\approx$ 1 ms) in the fIOS. A slower process on the timescale of $\approx$ 10 ms is observed. To our knowledge this is the first detection of a fIOS in myelinated nerves.

6.5.2 The sIOS

When looking at the speckle, we noticed bursts of movement that lasted for a few seconds. To observe this phenomena, we set the camera to a framerate of 100 Hz and recorded

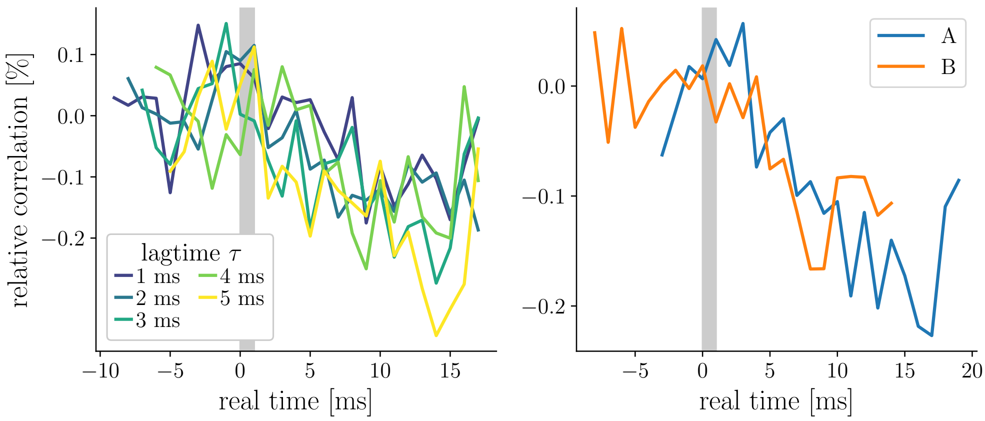

Figure 6.11: Fast time resolved speckle decorrelation of a nerve chord after electric stimulation. The left panel shows the relative change of correlation for each lagtime (1 ms to 5 ms) from measurement A. The correlation curves for all lagtimes are averaged, and shown in the right panel. In measurement B, the timing of the stimulus pulse was delayed by another 5 ms. All curves are averages over 1000 records each, and are aligned at the time of the stimulus pulse at $t = 0\,\mathrm{ms}$

continuously for minutes. To stimulate we applied pulses of 1 V and 1 ms at at rate of 10 Hz. The complete measurement (a to f) is presented in figure 6.12. The stimulation was applied for a duration of 5 s followed by a resting time of 25 s in measurement a and b. A stimulation period of 10 s with a resting time of 30 s was chosen in measurement c to f. The shorter stimulation period (5 s in a and b) sometimes lead to a faster dynamic, but this was not always the case. A stronger response and also overall activity was observed when the stimulus period was set to 10 s. The nerve was kept dry by completely enclosing it in the cavity and the electrode chamber. On the following day, no APs were detected upon electric stimulation. The measurements e and f were performed analogously with the *dead* specimen, and showed a very slow decorrelation ($\tau \gg 1\,\mathrm{s}$) and no correlation with the electrical stimulus. These insights are discussed in the next section.

6.6 Summary

From the characterization of the cavity it is shown that the enhancement effect depends on the turbidity of the sample. In optically thin samples the cavity produces angular averaging of the single scattering decorrelation and ensures ergodization. The latter is the key feature for measurements from biological samples.

The VNC is quite turbid, we estimate the mean free path to be in the order of 100 µm. However, it does not fill the cavity, but leaves a considerable empty volume. In a perfect cavity, the light field is homogeneous and therefore the filling fraction is irrelevant. Since the enhancement of optically thin samples is close to unity, it is assumed that this limit

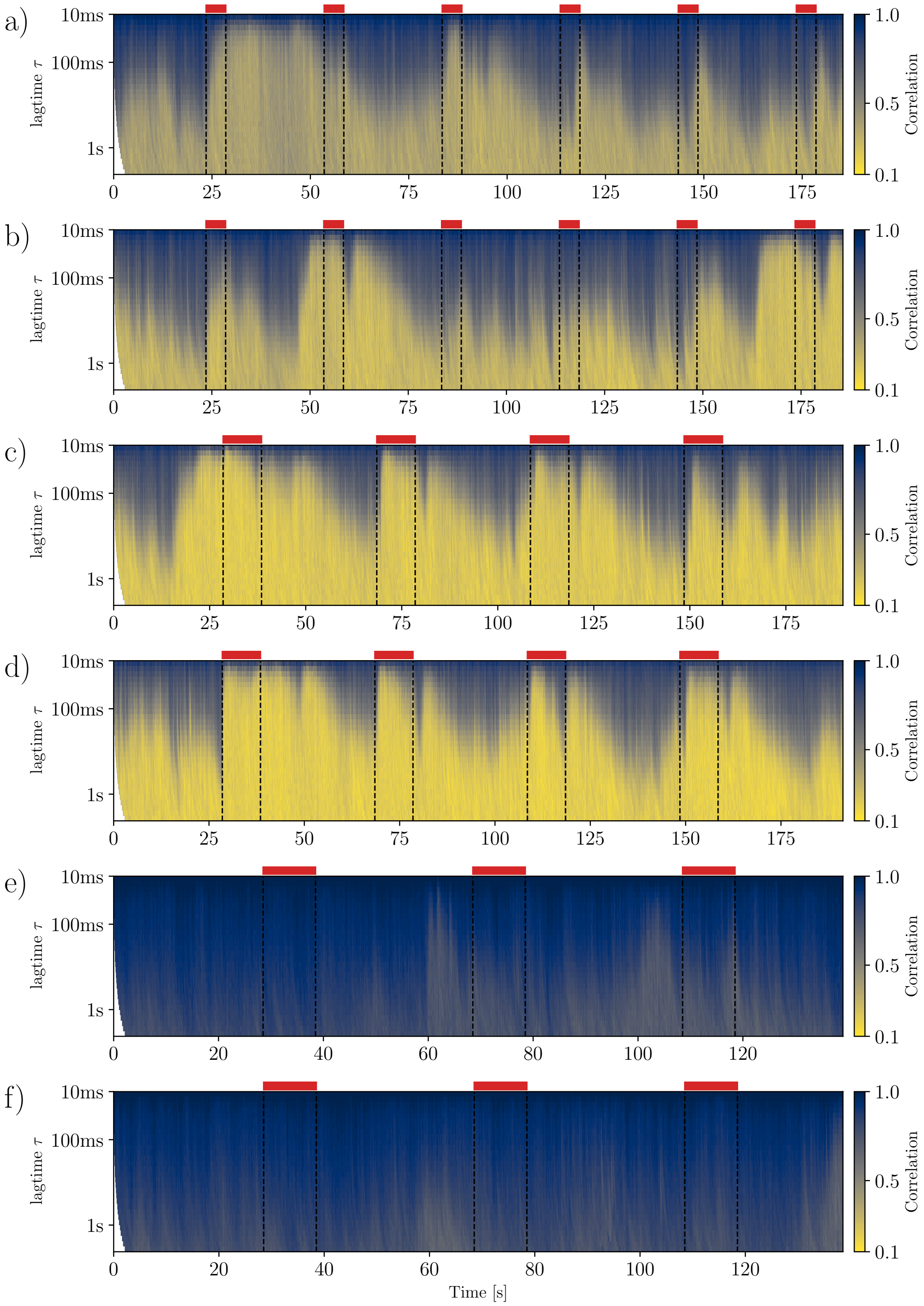

Figure 6.12: The slow intrinsic optical activity of a nerve chord. The red bars and dashed vertical lines indicate the stimulus period. Measurements a-d were recorded while the nerve was electrically responding, e and f were recorded from a *dead* specimen (Details in Section6.5.2).

is far away. More testing and numerical simulations will presumably provide important insights to this regime of the cavity and enable significant optimization.

In the preliminary multi-mode experiments that are presented in Section 6.5, the limiting factor was merely the detected intensity. A dedicated design of a multi-mode cavity can probably increase the intensity by an order of magnitude or more, then a framerate of around 3 kHz and a huge improvement in signal to noise ratio is feasible without further modification of the setup. Even without an optimized detection the almost real time acquisition of the correlation function reveals surprising features and timescales of the optical activity. The slow bursts of activity occur upon electrical stimulation, but are also observed without stimulation. In some measurements, it seems that stopping the stimulus may also activate this process. Clearly, the sIOS reveals a different process and yields information that are complementary to the electric observation.

As a final note, it should be mentioned, that future attempts to measure the fIOS can crucially benefit from observing the sIOS. The minute fIOS is easily buried in the drastic bursts of the sIOS. However, if the sIOS is observed simultaneously, the fIOS can be accessed in pauses of the sIOS.

7 Conclusion

I investigated optical and electrical manifestations of neuronal activity in nerve fibers. Action Potentials Annihilate when they collide in a nerve fiber. The electrical recordings from the collision experiment enable access to otherwise hidden properties of APs: the collision length $\lambda_c^\star$, the relaxation time τ and the ephaptic discharge Ψ. The ephaptic discharge is a particularly important property because it describes the electric influence of APs upon neighboring cells, and electric forces upon dipolar or dielectric particles, proteins or enzymes.

The HH model spectacularly underestimates the ephaptic discharge by more than one order of magnitude. To capture the results, the Relaxing Cable (RC) model is developed in this thesis. It is based on a simplistic model proposed by Tasaki [191], which i refer to as TC model. The RC model fits well to the observed relaxation period, which is neglected in the TC model, and not well captured in the HH model despite it's more than 20 parameters. The TC is adjusted to the experimental velocity with a single free parameter, and the RC model adds a relaxation time, which is directly extracted from the collision experiment. The TC and RC models provide an excellent fit to the experimentally determined ephaptic discharge, which describes a versatile interaction between Action Potentials and their surroundings based on classical electrodynamics. The effect can be excitatory or inhibitory, depending on position, orientation *and* timing. Ephaptic discharge can explain various forms of interactions. It further allows to formulate a hypothesis about collisions as a mechanism of information processing. Collisions transform a correlation of signals (in time) into a spatial pattern of ephaptic discharge. This is similar to a coincidence detection which is required in sound localization. It is further hypothesized that even learning and memory can result from this mechanism, because the ephaptic discharge is a field inhomogeneity that is expected to cause structural changes in the cell [36]. However, structural changes like changes in synaptic connectivity are non-electrical processes and require a non-electrical method of observation.

Such processes of Neuronal activity cause a minute intrinsic optical signal. It can be detected by various methods, where either the scattered or the transmitted light is detected. Those yield fundamentally different information. The transmitted light is subject to birefringence and there have been some publications that report changes in birefringence accompanied by the Action Potential. This is referred to as the fast intrinsic optical signal (fIOS). These experiments use crustacean nerves, because they rely on the detection of transmitted light, and crustacean nerve fibers are particularly transparent. Most nerves in nature, especially mammalian nerves are too turbid to be observed with this approach.

We initially employed a very sensitive method to detect birefringence from lobster nerves. The method's sensitivity to birefringence exceeds the instruments that have been reported to detect a signal so far. Surprisingly, no optical signature of the Action Potential was found. However, with a specific modification of the setup, we tested the hypothesis that the optical signal is actually found in light that is *scattered* at very small angles. When no particular care is taken, this fraction of scattered light can therefore reach the detector in a transmission experiment. Indeed, a fast optical fluctuation has been detected as a change in the light that is scattered at very small angles. This contradicts the sometimes presented interpretation of the fIOS as being caused by changes in birefringence.

The aim of this thesis is to explore this optical signature. The time dependence and strength of the signal we observed are in agreement with the suspected birefringence changes that have been reported by others. This leads us to believe that the signals previously interpreted as birefringence were, in fact, signatures of scattering.

To amplify the minute fluctuation of the scattered light, the nerve is surrounded by a white, diffuse, and highly-reflecting material. The effect of this optical cavity is a randomization of scattering angles and an increase of scattering events. This method is referred to as Cavity Amplified Speckle Spectroscopy, or CASS [75]. In addition to changing the detection scheme, we replaced the lobster nerve with the ventral nerve chord of an earthworm. The advantages of the latter are that one has a well-controlled, single axon which can easily be kept alive for many hours. On continuous stimulation of the specimen, we saw an acceleration of the measured optical decorrelation time. This is the first observation of intrinsic optical activity caused by a single axon, which is even myelinated and embedded in a nerve fiber.

We extended the CASS experiment with a multi-speckle detection scheme (MS-CASS). This improves the time resolution from minutes to milliseconds. Additionally to the fast, pulse-by-pulse signature (fIOS) of propagating Action Potentials, we discovered a signature of neuronal activity that corresponds to a considerably slower process. This slow intrinsic optical signal (sIOS) is somehow influenced by Action Potentials. It is not clear what the origin of the sIOS is. It might be metabolic activity to keep the active cells in their non-equilibrium resting state. Intriguingly, we may also speculate that axons adapt to activity patterns with structural changes, early stages of what is known as plasticity.

Bibliography

[1] B. C. Abbott, A. V. Hill, and J. V. Howarth. "The Positive and Negative Heat Production Associated with a Nerve Impulse". *Proc Royal Soc B* 148.931 (1958). DOI: `10.1098/rspb.1958.0012`.

[2] A. Adamatzky and J. Durand-Lose. "Collision-Based Computing". In: *Handbook of Natural Computing, Section VII: Broader Perspective — Alternative Models of Computation.* Ed. by G. Rozenberg, T. Bäck, and J. N. Kok. Springer, 2012. DOI: `10.1007/978-3-540-92910-9_58`.

[3] A. Adamatzky, F. Huber, and J. Schnauß. "Computing on Actin Bundles Network". *Sci. Rep.* 9.1 (2019). DOI: `10.1038/s41598-019-51354-y`.

[4] E. Akkermans, P. E. Wolf, and R. Maynard. "Coherent Backscattering of Light by Disordered Media: Analysis of the Peak Line Shape". *Phys. Rev. Lett.* 56.14 (1986). DOI: `10.1103/PhysRevLett.56.1471`.

[5] T. Akkin et al. "Detection of Neural Activity Using Phase-Sensitive Optical Low-Coherence Reflectometry". *Opt. Express, OE* 12.11 (2004). DOI: `10.1364/OPEX.12.002377`.

[6] P. Alcami and A. El Hady. "Axonal Computations". *Front. Cell. Neurosci.* 13 (2019). DOI: `10.3389/fncel.2019.00413`.

[7] C. A. Anastassiou and C. Koch. "Ephaptic Coupling to Endogenous Electric Field Activity: Why Bother?" *Current Opinion in Neurobiology* 31 (2015). DOI: `10.1016/j.conb.2014.09.002`.

[8] C. A. Anastassiou et al. "The Effect of Spatially Inhomogeneous Extracellular Electric Fields on Neurons". *J Neurosci* 30.5 (2010). DOI: `10.1523/JNEUROSCI.3635-09.2010`.

[9] C. A. Anastassiou et al. "Ephaptic Coupling of Cortical Neurons". *Nat. Neurosci.* 14.2 (2011). DOI: `10.1038/nn.2727`.

[10] S. S. L. Andersen, A. D. Jackson, and T. Heimburg. "Towards a Thermodynamic Theory of Nerve Pulse Propagation". *Progress in Neurobiology* 88.2 (2009). DOI: `10.1016/j.pneurobio.2009.03.002`.

[11] C. M. Armstrong and B. Hille. "Voltage-Gated Ion Channels and Electrical Excitability". *Neuron* 20.3 (1998). DOI: `10.1016/s0896-6273(00)80981-2`.

[12] A. Arvanitaki. "Effects Evoked in an Axon by the Activity of a Contiguous One". *J Neurophysiol* 5.2 (1942). DOI: `10.1152/jn.1942.5.2.89`.

[13] G. Ashida and C. E. Carr. "Sound Localization: Jeffress and Beyond". *Current Opinion in Neurobiology* 21.5 (2011). DOI: `10.1016/j.conb.2011.05.008`.

[14] A. H. Badreddine, T. Jordan, and I. J. Bigio. "Real-Time Imaging of Action Potentials in Nerves Using Changes in Birefringence". *Biomed Opt Express* 7.5 (2016). DOI: `10.1364/BOE.7.001966`.

[15] A. H. Badreddine, K. J. Schoener, and I. J. Bigio. "Elucidating the Temporal Dynamics of Optical Birefringence Changes in Crustacean Nerves". *Biomed Opt Express* 6.10 (2015). DOI: `10.1364/BOE.6.004165`.

[16] L. A. Bagatolli. "To See or Not to See: Lateral Organization of Biological Membranes and Fluorescence Microscopy". *Biochim. Biophys. Acta - Biomembranes* 1758.10 (2006). DOI: `10.1016/j.bbamem.2006.05.019`.

[17] G. Baranauskas and M. Martina. “Sodium Currents Activate without a Hodgkin and Huxley-Type Delay in Central Mammalian Neurons”. *J. Neurosci.* 26.2 (2006). DOI: `10.1523/JNEUROSCI.2283-05.2006`.

[18] B. Barbour. “Only Negligible Deviations from Electroneutrality Are Expected in Dendritic Spines”. *Nat Rev Neurosci* 21.1 (2020). DOI: `10.1038/s41583-019-0238-x`.

[19] C. Bédard, H. Kröger, and A. Destexhe. “Modeling Extracellular Field Potentials and the Frequency - Filtering Properties of Extracellular Space”. *Biophys J* 86.3 (2004). DOI: `10.1016/S0006-3495(04)74250-2`.

[20] R. W. Berg et al. “Comment on ‘Penetration of Action Potentials During Collision in the Median and Lateral Giant Axons of Invertebrates’ ”. *Phys. Rev. X* 7.2 (2017). DOI: `10.1103/PhysRevX.7.028001`.

[21] B. J. Berne and R. Pecora. *Dynamic Light Scattering: With Applications to Chemistry, Biology, and Physics.* Dover ed. Dover Publications, 2000. ISBN: 978-0-486-41155-2.

[22] K. P. Berry and E. Nedivi. “Spine Dynamics: Are They All the Same?” *Neuron* 96.1 (2017). DOI: `10.1016/j.neuron.2017.08.008`.

[23] M. Bestehorn. *Hydrodynamik und Strukturbildung: Mit einer kurzen Einführung in die Kontinuumsmechanik.* Springer-Verlag, 2006. ISBN: 978-3-540-33797-3.

[24] F. Bezanilla. “Gating Currents”. *J. Gen. Physiol.* 150.7 (2018). DOI: `10.1085/jgp.201812090`.

[25] C. F. Bohren and D. Huffman. *Absorption and Scattering of Light by Small Particles.* John Wiley & Sons, 1983. ISBN: 978-3-527-61816-3.

[26] D. Boinagrov, J. Loudin, and D. Palanker. “Strength–Duration Relationship for Extracellular Neural Stimulation: Numerical and Analytical Models”. *J Neurophysiol* 104.4 (2010). DOI: `10.1152/jn.00343.2010`.

[27] M. Born. *Principles of Optics, Seventh Edition.* Cambridge University Press, 1999.

[28] B. Bozorg, M. A. Lomholt, and H. Khandelia. “Thermodynamic Investigation of the Mechanism of Heat Production During Membrane Depolarization”. *J. Phys. Chem. B* 124.14 (2020). DOI: `10.1021/acs.jpcb.9b11456`.

[29] A. G. Brown. *Nerve Cells and Nervous Systems: An Introduction to Neuroscience.* Springer Science & Business Media, 2012. ISBN: 978-1-4471-3345-2.

[30] W. Brown, ed. *Dynamic Light Scattering: The Method and Some Applications.* 49. Clarendon Press ; Oxford University Press, 1993. ISBN: 978-0-19-853942-1.

[31] G. Buzsáki, C. A. Anastassiou, and C. Koch. “The Origin of Extracellular Fields and Currents — EEG, ECoG, LFP and Spikes”. *Nat Rev Neurosci* 13.6 (2012). DOI: `10.1038/nrn3241`.

[32] K. M. Carter, J. S. George, and D. M. Rector. “Simultaneous Birefringence and Scattered Light Measurements Reveal Anatomical Features in Isolated Crustacean Nerve”. *J. Neurosci. Methods* 135.1-2 (2004). DOI: `10.1016/j.jneumeth.2003.11.010`.

[33] C. A. Chapot, T. Euler, and T. Schubert. “How Do Horizontal Cells ‘Talk’ to Cone Photoreceptors? Different Levels of Complexity at the Cone–Horizontal Cell Synapse”. *J Physiol* 595.16 (2017). DOI: `10.1113/JP274177`.

[34] G. Chartier. *Introduction to Optics.* Springer-Verlag, 2005. ISBN: 978-0-387-40346-5. DOI: `10.1007/b106780`.

[35] C.-C. Chiang et al. “Slow Periodic Activity in the Longitudinal Hippocampal Slice Can Self-Propagate Non-Synaptically by a Mechanism Consistent with Ephaptic Coupling”. *J Physiol* 597.1 (2019). DOI: `10.1113/JP276904`.

[36] M. Cifra. “Electrodynamic Eigenmodes in Cellular Morphology”. *Biosystems* 109.3 (2012). DOI: `10.1016/j.biosystems.2012.06.003`.

[37] L. Cipelletti and D. A. Weitz. “Ultralow-Angle Dynamic Light Scattering with a Charge Coupled Device Camera Based Multispeckle, Multitau Correlator”. *Rev. Sci. Instrum.* 70.8 (1999). DOI: `10.1063/1.1149894`.

[38] J. Clark and R. Plonsey. “The Extracellular Potential Field of the Single Active Nerve Fiber in a Volume Conductor”. *Biophys J* 8.7 (1968).

[39] L. B. Cohen, B. Hille, and R. D. Keynes. “Changes in Axon Birefringence during the Action Potential”. *J Physiol* 211.2 (1970). DOI: `10.1113/jphysiol.1970.sp009289`.

[40] L. Cohen, R. Keynes, and B. Hille. “Light Scattering and Birefringence Changes During Nerve Activity”. *Nature* 218.5140 (1968). DOI: `10.1038/218438a0`.

[41] K. S. Cole. *Membranes, Ions and Impulses: A Chapter of Classical Biophysics.* University of California Press, 1972. ISBN: 978-0-520-00251-7.

[42] K. S. Cole. “Mostly Membranes”. *Annu. Rev. Physiol.* 41.1 (1979). DOI: `10.1146/annurev.ph.41.030179.000245`.

[43] K. S. Cole. “Neuromembranes: Paths of Ions”. In: *The Neurosciences: Paths of Discovery, I.* Ed. by F. G. Worden, J. P. Swazey, and G. Adelman. Boston, MA: Birkhäuser, 1992. ISBN: 978-1-4684-6817-5. DOI: `10.1007/978-1-4684-6817-5_8`.

[44] K. S. Cole and H. J. Curtis. “Electric Impedance of the Squid Giant Axon during Activity”. *J Gen Physiol* 22.5 (1939). DOI: `10.1085/jgp.22.5.649`.

[45] K. S. Cole and J. W. Moore. “Potassium Ion Current in the Squid Giant Axon: Dynamic Characteristic”. *Biophys J* 1.1 (1960). DOI: `10.1016/S0006-3495(60)86871-3`.

[46] B. W. Connors. “Synchrony and so Much More: Diverse Roles for Electrical Synapses in Neural Circuits”. *Dev. Neurobiol.* 77.5 (2017). DOI: `10.1002/dneu.22493`.

[47] C. F. Craver. “Physical Law and Mechanistic Explanation in the Hodgkin and Huxley Model of the Action Potential”. *Philosophy of Science* 75.5 (2008). DOI: `10.1086/594543`.

[48] W. Demtröder. *Experimentalphysik2: Elektrizität und Optik.* Springer-Verlag, 2013. ISBN: 978-3-662-06967-7.

[49] C. D. Drewes and R. A. Pax. “Neuromuscular Physiology of the Longitudinal Muscle of the Earthworm, Lumbricus Terrestris”. *J. Exp. Biol.* 60.2 (1974).

[50] B. Drukarch et al. “Thinking about the Nerve Impulse: A Critical Analysis of the Electricity-Centered Conception of Nerve Excitability”. *Prog Neurobiol* 169 (2018). DOI: `10.1016/j.pneurobio.2018.06.009`.

[51] J. C. Eccles. “The Synapse: From Electrical to Chemical Transmission”. *Annu. Rev. Neurosci.* 5.1 (1982). DOI: `10.1146/annurev.ne.05.030182.001545`.

[52] J. Eccles. “Evolution of Consciousness”. *Proc. Natl. Acad. Sci. U. S. A.* 89.16 (1992). DOI: `10.1073/pnas.89.16.7320`.

[53] D. C. Elton. “Stretched Exponential Relaxation”. *ArXiv180800881 Cond-Mat* (2018).

[54] L. Erskine and C. D. McCaig. “Growth Cone Neurotransmitter Receptor Activation Modulates Electric Field-Guided Nerve Growth”. *Developmental Biology* 171.2 (1995). DOI: `10.1006/dbio.1995.1285`.

[55] D. J. Evans, D. J. Searles, and E. Mittag. “Fluctuation Theorem for Hamiltonian Systems: Le Chatelier’s Principle”. *Phys. Rev. E* 63.5 (2001). DOI: `10.1103/PhysRevE.63.051105`.

[56] R. P. Feynman, R. B. Leighton, and M. Sands. *The Feynman Lectures on Physics, Vol. II: The New Millennium Edition: Mainly Electromagnetism and Matter.* Basic Books, 2011. ISBN: 978-0-465-02494-0.

[57] C. Fillafer, A. Paeger, and M. F. Schneider. “Collision of Two Action Potentials in a Single Excitable Cell”. *Biochim. Biophys. Acta - General Subjects* 1861.12 (2017). DOI: `10.1016/j.bbagen.2017.09.020`.

[58] C. Fillafer and M. F. Schneider. “On the Temperature Behavior of Pulse Propagation and Relaxation in Worms, Nerves and Gels”. *PLOS ONE* 8.6 (2013). DOI: `10.1371/journal.pone.0066773`.

[59] C. Fillafer et al. “Cell Surface Deformation during an Action Potential”. *Biophys J* 114.2 (2018). DOI: `10.1016/j.bpj.2017.11.3776`.

[60] D. C. Fitzpatrick, S. Kuwada, and R. Batra. “Neural Sensitivity to Interaural Time Differences: Beyond the Jeffress Model”. *J. Neurosci.* 20.4 (2000).

[61] R. Follmann, E. Rosa, and W. Stein. “Dynamics of Signal Propagation and Collision in Axons”. *Phys. Rev. E* 92.3 (2015). DOI: `10.1103/PhysRevE.92.032707`.

[62] A. J. Foust, R. M. Beiu, and D. M. Rector. “Optimized Birefringence Changes during Isolated Nerve Activation.” *Appl Opt* 44.11 (2005). DOI: `10.1364/AO.44.002008`.

[63] A. J. Foust and D. M. Rector. “Optically Teasing Apart Neural Swelling and Depolarization”. *Neuroscience* 145.3 (2007). DOI: `10.1016/j.neuroscience.2006.12.068`.

[64] J. M. Freyssinet et al. “Fibrinogen and Fibrin Structure and Fibrin Formation Measured by Using Magnetic Orientation.” *Proc Natl Acad Sci USA* 80.6 (1983).

[65] B. Frka-Petesic et al. “Negative Diamagnetic Anisotropy and Birefringence of Cellulose Nanocrystals”. *Macromolecules* 48 (2015). DOI: `10.1021/acs.macromol.5b02201`.

[66] R. C. Froemke and Y. Dan. “Spike-Timing-Dependent Synaptic Modification Induced by Natural Spike Trains”. *Nature* 416.6879 (2002). DOI: `10.1038/416433a`.

[67] T. Furukawa, Y. Fukami, and Y. Asada. “A Third Type of Inhibition in the Mauthner Cell of Goldfish”. *J Neurophysiol* 26.5 (1963). DOI: `10.1152/jn.1963.26.5.759`.

[68] K. Furusawa. “The Depolarization of Crustacean Nerve by Stimulation or Oxygen Want”. *J Physiol* 67.4 (1929). DOI: `10.1113/jphysiol.1929.sp002573`.

[69] W. J. Gardner. “Cross Talk—The Paradoxical Transmission of a Nerve Impulse”. *Arch Neurol* 14.2 (1966). DOI: `10.1001/archneur.1966.00470080033005`.

[70] L. R. Gavrilov and E. M. Tsirulnikov. “Focused Ultrasound as a Tool to Input Sensory Information to Humans (Review)”. *Acoust. Phys.* 58.1 (2012). DOI: `10.1134/S1063771012010083`.

[71] J. H. Goldwyn and J. Rinzel. “Neuronal Coupling by Endogenous Electric Fields: Cable Theory and Applications to Coincidence Detector Neurons in the Auditory Brain Stem”. *J Neurophysiol* 115.4 (2016). DOI: `10.1152/jn.00780.2015`.

[72] A. Gonzalez-Perez et al. “Penetration of Action Potentials During Collision in the Median and Lateral Giant Axons of Invertebrates”. *Phys. Rev. X* 4.3 (2014). DOI: `10.1103/PhysRevX.4.031047`.

[73] D. F. M. Goodman and R. Brette. “Brian: A Simulator for Spiking Neural Networks in Python”. *Front. Neuroinform.* 2 (2008). DOI: `10.3389/neuro.11.005.2008`.

[74] D. F. M. Goodman, R. Brette, and M. Stimberg. *Brian2*. `briansimulator.org`, source code availible at `github.com/brian-team/brian2` (version 2.3, accessed Dec. 22, 2019).

[75] G. Graciani and F. Amblard. “Random Dynamic Interferometer: Cavity Amplified Speckle Spectroscopy Using a Highly Symmetric Coherent Field Created inside a Closed Lambertian Optical Cavity”. *Applied Optical Metrology III.* SPIE, 2019. DOI: `10.1117/12.2530775`.

[76] S. L. Gratiy et al. “From Maxwell’s Equations to the Theory of Current-Source Density Analysis”. *Eur. J. Neurosci.* 45.8 (2017). DOI: `10.1111/ejn.13534`.

[77] B. Grothe, M. Pecka, and D. McAlpine. “Mechanisms of Sound Localization in Mammals”. *Physiol. Rev.* 90.3 (2010). DOI: `10.1152/physrev.00026.2009`.

[78] A. E. Hady and B. B. Machta. “Mechanical Surface Waves Accompany Action Potential Propagation”. *Nat. Commun.* 6 (2015). DOI: `10.1038/ncomms7697`.

[79] T. C. Hamilton and D. Osborn. “Measurements of Contraction Latencies to Mechanical and Electrical Stimulation of the Protozoan, Spirostomum Ambiguum”. *J. Cell. Physiol.* 91.3 (1977). DOI: `10.1002/jcp.1040910310`.

[80] K.-S. Han et al. “Ephaptic Coupling Promotes Synchronous Firing of Cerebellar Purkinje Cells”. *Neuron* 100.3 (2018). DOI: `10.1016/j.neuron.2018.09.018`.

[81] M. Hartley, N. Taylor, and J. Taylor. “Understanding Spike-Time-Dependent Plasticity: A Biologically Motivated Computational Model”. *Neurocomputing* 69.16 (2006). DOI: `10.1016/j.neucom.2005.11.021`.

[82] R. B. Hawkes and D. V. Holberton. “Myonemal Contraction of Spirostomum I. Kinetics of Contraction and Relaxation”. *J. Cell. Physiol.* 84.2 (1974). DOI: `10.1002/jcp.1040840209`.

[83] T. Heimburg and A. D. Jackson. “On Soliton Propagation in Biomembranes and Nerves”. *Proc Natl Acad Sci USA* 102.28 (2005). DOI: `10.1073/pnas.0503823102`.

[84] O. Herreras. “Local Field Potentials: Myths and Misunderstandings”. *Front Neural Circuits* 10 (2016). DOI: `10.3389/fncir.2016.00101`.

[85] B. C. Hill et al. “Laser Interferometer Measurement of Changes in Crayfish Axon Diameter Concurrent with Action Potential”. *Science* 196.4288 (1977). DOI: `10.1126/science.850785`.

[86] D. K. Hill. “The Volume Change Resulting from Stimulation of a Giant Nerve Fibre”. *J Physiol* 111.3-4 (1950). DOI: `10.1113/jphysiol.1950.sp004481`.

[87] B. Hille. *Ionic Channels of Excitable Membranes.* Sinauer, 2001. ISBN: 978-0-87893-321-1.

[88] *Hinds Instruments, Inc.* `www.hindsinstruments.com` (2018). 97124 Oregon, USA.

[89] A. L. Hodgkin and A. F. Huxley. “Action Potentials Recorded from Inside a Nerve Fibre”. *Nature* 144.3651 (1939). DOI: `10.1038/144710a0`.

[90] A. L. Hodgkin and A. F. Huxley. “A Quantitative Description of Membrane Current and Its Application to Conduction and Excitation in Nerve”. *J Physiol* 117.4 (1952).

[91] A. L. Hodgkin and A. F. Huxley. “Movement of Sodium and Potassium Ions During Nervous Activity”. *Cold Spring Harbor Symp. Quant. Biol.* 17 (1952). DOI: `10.1101/SQB.1952.017.01.007`.

[92] G. R. Holt and C. Koch. “Electrical Interactions via the Extracellular Potential near Cell Bodies”. *J Comput Neurosci* 6.2 (1999). DOI: `10.1023/a:1008832702585`.

[93] T. Hoshi and C. M. Armstrong. “The Cole-Moore Effect: Still Unexplained?” *Biophys J* 109.7 (2015). DOI: `10.1016/j.bpj.2015.07.052`.

[94] C. Hu and G. Popescu. “Quantitative Phase Imaging (QPI) in Neuroscience”. *IEEE J. Sel. Top. Quantum Electron.* 25.1 (2019). DOI: `10.1109/JSTQE.2018.2869613`.

[95] H. C. van de Hulst. *Light Scattering by Small Particles.* Courier Corporation, 1957. ISBN: 978-0-486-64228-4.

[96] A. Huxley. “Kenneth Stewart Cole: July 10, 1900 - April 18, 1984”. *Biogr Mem Natl Acad Sci* 70 (1996).

[97] A. Huxley. “The Quantitative Analysis of Excitation and Conduction in Nerve”. *Nobel Prize Physiol. Med. 1963* (1963).

[98] I. Inoue, Y. Kobatake, and I. Tasaki. “Excitability, Instability and Phase Transitions in Squid Axon Membrane under Internal Perfusion with Dilute Salt Solutions”. *Biochim. Biophys. Acta - Biomembranes* 307.3 (1973). DOI: `10.1016/0005-2736(73)90294-0`.

[99] N. Isert, G. Maret, and C. M. Aegerter. “Studying Foam Dynamics in Levitated, Dry and Wet Foams Using Diffusing Wave Spectroscopy”. *Colloids and Surfaces A* 473 (2015). DOI: `10.1016/j.colsurfa.2014.11.028`.

[100] A. Iwakura et al. “Lack of Molecular–Anatomical Evidence for GABAergic Influence on Axon Initial Segment of Cerebellar Purkinje Cells by the Pinceau Formation”. *J. Neurosci.* 32.27 (2012). DOI: `10.1523/JNEUROSCI.1651-12.2012`.

[101] K. Iwasa, I. Tasaki, and R. C. Gibbons. “Swelling of Nerve Fibers Associated with Action Potentials”. *Science* 210.4467 (1980). DOI: `10.1126/science.7423196`.

[102] M. H. Jakubowski, K. Steiglitz, and R. Squier. “Computing with Classical Soliton Collisions”. In: *Advances in Unconventional Computing.* Ed. by A. Adamatzky. Vol. 23. Cham: Springer International Publishing, 2017. ISBN: 978-3-319-33921-4. DOI: `10.1007/978-3-319-33921-4_12`.

[103] J. G. Jefferys. “Nonsynaptic Modulation of Neuronal Activity in the Brain: Electric Currents and Extracellular Ions”. *Physiol. Rev.* 75.4 (1995). DOI: `10.1152/physrev.1995.75.4.689`.

[104] P. Joos and G. Serrien. “The Principle of Braun—Le Châtelier at Surfaces”. *J. Colloid Interface Sci.* 145.1 (1991). DOI: `10.1016/0021-9797(91)90123-P`.

[105] P. X. Joris, P. H. Smith, and T. C. T. Yin. “Coincidence Detection in the Auditory System: 50 Years after Jeffress”. *Neuron* 21.6 (1998). DOI: `10.1016/S0896-6273(00)80643-1`.

[106] B. Katz and O. H. Schmitt. “Electric Interaction between Two Adjacent Nerve Fibres”. *J Physiol* 97.4 (1940).

[107] E. T. Kavalali. “The Mechanisms and Functions of Spontaneous Neurotransmitter Release”. *Nat. Rev. Neurosci.* 16.1 (2015). DOI: `10.1038/nrn3875`.

[108] D. J. Keith and A. El-Husseini. “Excitation Control: Balancing PSD-95 Function at the Synapse”. *Front. Mol. Neurosci.* 1 (2008). DOI: `10.3389/neuro.02.004.2008`.

[109] N. D. Kim. *Photon Self-Identity Issues.* `scienceandink.com` (2019), used by permission.

[110] C. Koch. *Biophysics of Computation: Information Processing in Single Neurons.* Oxford University Press, 2004. ISBN: 978-0-19-518199-9.

[111] H. Korn and D. S. Faber. “The Mauthner Cell Half a Century Later: A Neurobiological Model for Decision-Making?” *Neuron* 47.1 (2005). DOI: `10.1016/j.neuron.2005.05.019`.

[112] R. H. Kramer and C. M. Davenport. “Lateral Inhibition in the Vertebrate Retina: The Case of the Missing Neurotransmitter”. *PLOS Biology* 13.12 (2015). DOI: `10.1371/journal.pbio.1002322`.

[113] B. Krasovitski et al. “Intramembrane Cavitation as a Unifying Mechanism for Ultrasound-Induced Bioeffects.” *Proc Natl Acad Sci USA* 108.8 (2011). DOI: `10.1073/pnas.1015771108`.

[114] B. Lautrup, A. D. Jackson, and T. Heimburg. “The Stability of Solitons in Biomembranes and Nerves”. *arXiv:physics/0510106* (2005).

[115] H. J. Lee, Y. Jiang, and J.-X. Cheng. “Label-Free Optical Imaging of Membrane Potential”. *Current Opinion in Biomedical Engineering* 12 (2019). DOI: `10.1016/j.cobme.2019.11.001`.

[116] H. J. Lee et al. “Label-Free Vibrational Spectroscopic Imaging of Neuronal Membrane Potential”. *J. Phys. Chem. Lett.* 8.9 (2017). DOI: `10.1021/acs.jpclett.7b00575`.

[117] Y. Lee et al. “Excitatory and Inhibitory Synaptic Dysfunction in Mania: An Emerging Hypothesis from Animal Model Studies”. *Exp. Mol. Med.* 50.4 (2018). DOI: `10.1038/s12276-018-0028-y`.

[118] T. Ling et al. “Full-Field Interferometric Imaging of Propagating Action Potentials”. *Light Sci Appl* 7.1 (2018). DOI: `10.1038/s41377-018-0107-9`.

[119] *Lobster Anatomy.* The National Lobster Hatchery (Padstow, England) `nationallobsterhatchery.co.uk` (accessed May 1, 2019), used by permission. 2019.

[120] R. Lorente de No. “Analysis of the Distribution of the Action Currents of Nerve in Volume Conductors.” *Stud. Rockefeller Inst. Med. Res. Repr. Rockefeller Inst. Med. Res.* 132 (1947).

[121] R. Lorente de No and V. Honrubia. “Continuous Conduction of Action Potentials by Peripheral Myelinated Fibers”. *Proc Natl Acad Sci USA* 52 (1964). DOI: `10.1073/pnas.52.2.305`.

[122] P. Lövsund et al. “Magnetophosphenes: A Quantitative Analysis of Thresholds”. *Med. Biol. Eng. Comput.* 18.3 (1980). DOI: `10.1007/BF02443387`.

[123] S. Mack et al. *Principles of Neural Science, Fifth Edition*. McGraw Hill Professional, 2013. ISBN: 978-0-07-139011-8.

[124] G. Maret. “Diffusing-Wave Spectroscopy”. *Curr. Opin. Colloid Interface Sci.* 2.3 (1997). DOI: `10.1016/S1359-0294(97)80032-5`.

[125] G. Maret and K. Dransfeld. “Macromolecules and Membranes in High Magnetic Fields”. *Physica B+C* 86-88 (1977). DOI: `10.1016/0378-4363(77)90800-2`.

[126] G. Maret and G. Weill. “Magnetic Birefringence Study of the Electrostatic and Intrinsic Persistence Length of DNA”. *Biopolymers* 22.12 (1983). DOI: `10.1002/bip.360221215`.

[127] G. Maret and P. E. Wolf. “Multiple Light Scattering from Disordered Media. The Effect of Brownian Motion of Scatterers”. *Z. Physik B - Condensed Matter* 65.4 (1987). DOI: `10.1007/BF01303762`.

[128] G. Maret and K. Dransfeld. “Biomolecules and Polymers in High Steady Magnetic Fields”. In: *Strong and Ultrastrong Magnetic Fields and Their Applications*. Ed. by P. D. F. Herlach. 57. Springer Berlin Heidelberg, 1985. ISBN: 978-3-540-13504-3. DOI: `10.1007/3-540-13504-9_10`.

[129] M. S. Markov. “Biological Effects of Extremely Low Frequency Magnetic Fields”. In: *Biomagnetic Stimulation*. Ed. by S. Ueno. Boston, MA: Springer US, 1994. ISBN: 978-1-4757-9507-3. DOI: `10.1007/978-1-4757-9507-3_7`.

[130] M. Martinez-Banaclocha. “Ephaptic Coupling of Cortical Neurons: Possible Contribution of Astroglial Magnetic Fields?” *Neuroscience* 370 (2018). DOI: `10.1016/j.neuroscience.2017.07.072`.

[131] M. Martinez-Banaclocha. “Astroglial Isopotentiality and Calcium-Associated Biomagnetic Field Effects on Cortical Neuronal Coupling”. *Cells* 9.2 (2020). DOI: `10.3390/cells9020439`.

[132] A. J. T. M. Mathijssen et al. “Collective Intercellular Communication through Ultra-Fast Hydrodynamic Trigger Waves”. *Nature* 571.7766 (2019). DOI: `10.1038/s41586-019-1387-9`.

[133] C. D. McCaig, L. Sangster, and R. Stewart. “Neurotrophins Enhance Electric Field-Directed Growth Cone Guidance and Directed Nerve Branching”. *Dev. Dyn.* 217.3 (2000). DOI: `10.1002/(SICI)1097-0177(200003)217:3<299::AID-DVDY8>3.0.CO;2-G`.

[134] D. A. McCormick, Y. Shu, and Y. Yu. “Hodgkin and Huxley Model — Still Standing?” *Nature* 445.7123 (2007). DOI: `10.1038/nature05523`.

[135] D. R. McNeal. “Analysis of a Model for Excitation of Myelinated Nerve”. *IEEE Trans. Biomed. Eng.* BME-23.4 (1976). DOI: `10.1109/TBME.1976.324593`.

[136] J. W. Moore. “Enhancing the Hodgkin-Huxley Equations: Simulations Based on the First Publication in the Biophysical Journal”. *Biophys J* 109.7 (2015). DOI: `10.1016/j.bpj.2015.08.008`.

[137] M. Mussel, P. J. Basser, and F. Horkay. “Effects of Mono- and Divalent Cations on the Structure and Thermodynamic Properties of Polyelectrolyte Gels”. *Soft Matter* 15.20 (2019). DOI: `10.1039/C9SM00464E`.

[138] M. Mussel and M. F. Schneider. “It Sounds like an Action Potential: Unification of Electrical, Chemical and Mechanical Aspects of Acoustic Pulses in Lipids”. *J. R. Soc. Interface* 16.151 (2019). DOI: `10.1098/rsif.2018.0743`.

[139] M. Mussel and M. F. Schneider. “Similarities between Action Potentials and Acoustic Pulses in a van Der Waals Fluid”. *Sci. Rep.* 9.1 (2019). DOI: `10.1038/s41598-019-38826-x`.

[140] R. J. Nap and I. Szleifer. “Effect of Calcium Ions on the Interactions between Surfaces End-Grafted with Weak Polyelectrolytes”. *J. Chem. Phys.* 149.16 (2018). DOI: `10.1063/1.5029377`.

[141] P. Nelson. *Biological Physics: With New Art by David Goodsell*. W. H. Freeman, 2013. ISBN: 978-0-7167-9897-2.

[142] T. Nevian and B. Sakmann. "Spine Ca2+ Signaling in Spike-Timing-Dependent Plasticity". *J. Neurosci.* 26.43 (2006). DOI: `10.1523/JNEUROSCI.1749-06.2006`.

[143] M. Nishiyama et al. "Calcium Stores Regulate the Polarity and Input Specificity of Synaptic Modification". *Nature* 408.6812 (2000). DOI: `10.1038/35046067`.

[144] F. Offner, A. Weinberg, and G. Young. "Nerve Conduction Theory: Some Mathematical Consequences of Bernstein's Model". *Bulletin of Mathematical Biophysics* 2.2 (1940). DOI: `10.1007/BF02478173`.

[145] R. Oldenbourg. "A New View on Polarization Microscopy". *Nature* 381.6585 (1996). DOI: `10.1038/381811a0`.

[146] R. Oldenbourg. "Polarization Microscopy with the LC-PolScope". In: *Live Cell Imaging: A Laboratory Manual*. Ed. by R. D. Goldman and D. Spector. Cold Spring Harbor Laboratory, 2004. ISBN: 978-0-87969-683-2.

[147] Y. Oono and M. Paniconi. "Steady State Thermodynamics". *Prog Theor Phys* 130 (1998). DOI: `10.1143/PTPS.130.29`.

[148] R. Pethig. "Review Article—Dielectrophoresis: Status of the Theory, Technology, and Applications". *Biomicrofluidics* 4.2 (2010). DOI: `10.1063/1.3456626`.

[149] R. Pethig et al. *Dielectrophoresis: A Review of Applications for Stem Cell Research*. Review Article. 2010. DOI: `10.1155/2010/182581`.

[150] A. G. Petrov and V. S. Sokolov. "Curvature-Electric Effect in Black Lipid Membranes". *Eur Biophys J* 13.3 (1986). DOI: `10.1007/BF00542559`.

[151] A. G. Petrov. "Flexoelectricity in Lyotropics and in Living Liquid Crystals". In: *Flexoelectricity in Liquid Crystals*. Imperial College Press, 2011. ISBN: 978-1-84816-799-5. DOI: `10.1142/9781848168008_0007`.

[152] D. J. Pine et al. "Dynamical Correlations of Multiply Scattered Light". In: *Scattering and Localization of Classical Waves in Random Media*. Ed. by P. Sheng. Vol. 8. World Scientific, 1990. ISBN: 978-9971-5-0539-4. DOI: `10.1142/9789814340687_0006`.

[153] M. Plaksin, S. Shoham, and E. Kimmel. "Intramembrane Cavitation as a Predictive Bio - Piezoelectric Mechanism for Ultrasonic Brain Stimulation". *Phys. Rev. X* 4.1 (2014). DOI: `10.1103/PhysRevX.4.011004`.

[154] S. Prahl. *Miepython*. `github.com/scottprahl/miepython` (version 1.3.1, accessed Dec. 22, 2019).

[155] P. N. Pusey and W. Van Megen. "Dynamic Light Scattering by Non-Ergodic Media". *Physica A* 157.2 (1989). DOI: `10.1016/0378-4371(89)90063-0`.

[156] S. R. Raghavan and J. F. Douglas. "The Conundrum of Gel Formation by Molecular Nanofibers, Wormlike Micelles, and Filamentous Proteins: Gelation without Cross-Links?" *Soft Matter* 8.33 (2012). DOI: `10.1039/c2sm25107h`.

[157] D. Rand and K. Steiglitz. "Computing with Solitons". In: *Unconventional Computing: A Volume in the Encyclopedia of Complexity and Systems Science, Second Edition*. Ed. by A. Adamatzky. New York, NY: Springer US, 2018. ISBN: 978-1-4939-6883-1. DOI: `10.1007/978-1-4939-6883-1_92`.

[158] F. Rattay. "Analysis of Models for Extracellular Fiber Stimulation". *IEEE Trans. Biomed. Eng.* 36.7 (1989). DOI: `10.1109/10.32099`.

[159] F. Rattay. "The Basic Mechanism for the Electrical Stimulation of the Nervous System". *Neuroscience* 89.2 (1999). DOI: `10.1016/S0306-4522(98)00330-3`.

[160] M. W. Reimann et al. "A Biophysically Detailed Model of Neocortical Local Field Potentials Predicts the Critical Role of Active Membrane Currents". *Neuron* 79.2 (2013). DOI: `10.1016/j.neuron.2013.05.023`.

[161] J. M. Ritchie and R. D. Keynes. “The Production and Absorption of Heat Associated with Electrical Activity in Nerve and Electric Organ”. *Q. Rev. Biophys.* 18.4 (1985). DOI: `10.1017/S0033583500005382`.

[162] W. a. H. Rushton. “A Theory of the Effects of Fibre Size in Medullated Nerve”. *J Physiol* 115.1 (1951). DOI: `10.1113/jphysiol.1951.sp004655`.

[163] M. M. Rvachev. “On Axoplasmic Pressure Waves and Their Possible Role in Nerve Impulse Propagation”. *Biophys. Rev. Lett.* 05.02 (2010). DOI: `10.1142/S1793048010001147`.

[164] E. Sassaroli and N. Vykhodtseva. “Acoustic Neuromodulation from a Basic Science Prospective”. *J Ther Ultrasound* 4 (2016). DOI: `10.1186/s40349-016-0061-z`.

[165] R. M. Sattigeri. “Action Potential: A Vortex Phenomena; Driving Membrane Oscillations”. *Front. Comput. Neurosci.* 14 (2020). DOI: `10.3389/fncom.2020.00021`.

[166] W. Schärtl. *Light Scattering from Polymer Solutions and Nanoparticle Dispersions*. Springer Science & Business Media, 2007. ISBN: 978-3-540-71951-9.

[167] F. Scheffold. “Particle Sizing with Diffusing Wave Spectroscopy”. *J. Dispers. Sci. Technol.* 23.5 (2002). DOI: `10.1081/DIS-120015365`.

[168] H. Schmidt et al. *Ephaptic Coupling in White Matter Fibre Bundles Modulates Axonal Transmission Delays*. Preprint. Neuroscience, 2020. DOI: `10.1101/2020.04.08.031641`.

[169] K. M. Shannon et al. “Portable Conduction Velocity Experiments Using Earthworms for the College and High School Neuroscience Teaching Laboratory”. *Adv Physiol Educ* 38.1 (2014). DOI: `10.1152/advan.00088.2013`.

[170] H. Sheheitli and V. K. Jirsa. “A Mathematical Model of Ephaptic Interactions in Neuronal Fiber Pathways: Could There Be More than Transmission along the Tracts?” *Netw. Neurosci.* (2020). DOI: `10.1162/netn_a_00134`.

[171] R. S. Shivacharan et al. “Self-Propagating, Non-Synaptic Epileptiform Activity Recruits Neurons by Endogenous Electric Fields”. *Exp. Neurol.* 317 (2019). DOI: `10.1016/j.expneurol.2019.02.005`.

[172] S. Shrivastava. “Detonation of Shock-Waves and Action Potentials in Lipid Interfaces”. *Proc. Mtgs. Acoust.* 34.1 (2018). DOI: `10.1121/2.0000906`.

[173] S. Shrivastava, K. H. Kang, and M. F. Schneider. “Collision and Annihilation of Nonlinear Sound Waves and Action Potentials in Interfaces”. *J. R. Soc. Interface* 15.143 (2018). DOI: `10.1098/rsif.2017.0803`.

[174] S. Shrivastava and M. F. Schneider. “Opto-Mechanical Coupling in Interfaces under Static and Propagative Conditions and Its Biological Implications”. *PLOS ONE* 8.7 (2013). DOI: `10.1371/journal.pone.0067524`.

[175] S. Shrivastava and M. F. Schneider. “Evidence for Two - Dimensional Solitary Sound Waves in a Lipid Controlled Interface and Its Implications for Biological Signalling”. *J Royal Soc Interface* 11.97 (2014). DOI: `10.1098/rsif.2014.0098`.

[176] I. Siveke et al. “Binaural Response Properties of Low-Frequency Neurons in the Gerbil Dorsal Nucleus of the Lateral Lemniscus”. *J Neurophysiol* 96.3 (2006). DOI: `10.1152/jn.00713.2005`.

[177] J. Steinbrink et al. “The Fast Optical Signal - Robust or Elusive When Non-Invasively Measured in the Human Adult?” *NeuroImage* 26 (2005). DOI: `10.1016/j.neuroimage.2005.03.006`.

[178] T. C. Südhof. “Neurotransmitter Release: The Last Millisecond in the Life of a Synaptic Vesicle”. *Neuron* 80.3 (2013). DOI: `10.1016/j.neuron.2013.10.022`.

[179] H. Tamagawa and K. Ikeda. “Another Interpretation of the Goldman-Hodgkin-Katz Equation Based on Ling’s Adsorption Theory”. *Eur Biophys J* 47.8 (2018). DOI: `10.1007/s00249-018-1332-0`.

[180] I. Tasaki. “Collision of Two Nerve Impulses in the Nerve Fibre”. *Biochim. Biophys. Acta* 3 (1949). DOI: `10.1016/0006-3002(49)90121-3`.

[181] I. Tasaki. “New Measurements of the Capacity and the Resistance of the Myelin Sheath and the Nodal Membrane of the Isolated Frog Nerve Fiber”. *Am. J. Physiol. – Leg. Content* 181.3 (1955).

[182] I. Tasaki. “Evidence for Phase Transition in Nerve Fibers, Cells and Synapses”. *Ferroelectrics* 220.1 (1999). DOI: `10.1080/00150199908216221`.

[183] I. Tasaki. “Spread of Discrete Structural Changes in Synthetic Polyanionic Gel: A Model of Propagation of a Nerve Impulse”. *J. Theor. Biol.* 218.4 (2002). DOI: `10.1006/jtbi.2002.3095`.

[184] I. Tasaki. “A Note on the Local Current Associated with the Rising Phase of a Propagating Impulse in Nonmyelinated Nerve Fibers”. *Bull. Math. Biol.* 68.2 (2006). DOI: `10.1007/s11538-005-9012-5`.

[185] I. Tasaki. *Physiology and Electrochemistry of Nerve Fibers*. Elsevier, 2012. ISBN: 978-0-323-15407-9.

[186] I. Tasaki and P. M. Byrne. “The Origin of Rapid Changes in Birefringence, Light Scattering and Dye Absorbance Associated with Excitation of Nerve Fibers”. *Jpn. J. Physiol.* 43 Suppl 1 (1993).

[187] I. Tasaki and P. M. Byrne. “Temperature Changes Associated with Excitation of the Electric Organ in the African Electric Catfish”. *Biochem. Biophys. Res. Commun.* 200.2 (1994). DOI: `10.1006/bbrc.1994.1507`.

[188] I. Tasaki, K. Kusano, and P. M. Byrne. “Rapid Mechanical and Thermal Changes in the Garfish Olfactory Nerve Associated with a Propagated Impulse”. *Biophys J* 55.6 (1989). DOI: `10.1016/S0006-3495(89)82902-9`.

[189] I. Tasaki and T. Takenaka. “Resting and Action Potential of Squid Giant Axons Intracellularly Perfused with Sodium-Rich Solutions”. *PNAS* 50.4 (1963). DOI: `10.1073/pnas.50.4.619`.

[190] I. Tasaki and K. Iwasa. “Rapid Pressure Changes and Surface Displacements in the Squid Giant Axon Associated with Production of Action Potentials”. *Jpn. J. Physiol.* 32.1 (1982). DOI: `10.2170/jjphysiol.32.69`.

[191] I. Tasaki and G. Matsumoto. “On the Cable Theory of Nerve Conduction”. *Bull. Math. Biol.* 64.6 (2002). DOI: `10.1006/bulm.2002.0310`.

[192] I. Tasaki et al. “Changes in Fluorescence Turbidity and Birefringence Associated with Nerve Excitation”. *Proc Natl Acad Sci USA* 61.3 (1968). DOI: `10.1073/pnas.61.3.883`.

[193] S. Tolnai and G. M. Klump. “Evidence for the Origin of the Binaural Interaction Component of the Auditory Brainstem Response”. *Eur. J. Neurosci.* 51.2 (2020). DOI: `10.1111/ejn.14571`.

[194] A. Triller and H. Korn. “Glio-Axonic Junctional like Complexes at the Mauthner Cell’s Axon Cap of Teleosts: A Possible Morphological Basis for Field Effect Inhibitions”. *Neuroscience Letters* 18.3 (1980). DOI: `10.1016/0304-3940(80)90297-9`.

[195] W. Van der Goes van Naters. “Inhibition among Olfactory Receptor Neurons”. *Front. Hum. Neurosci.* 7 (2013). DOI: `10.3389/fnhum.2013.00690`.

[196] F. J. Vidal-Iglesias et al. “Do You Really Understand the Electrochemical Nernst Equation?” *Electrocatalysis* 4.1 (2013). DOI: `10.1007/s12678-012-0115-0`.

[197] T. Wang et al. “Reply to “Comment on ‘Penetration of Action Potentials During Collision in the Median and Lateral Giant Axons of Invertebrates”’”. *Phys. Rev. X* 7.2 (2017). DOI: `10.1103/PhysRevX.7.028002`.

[198] S. A. Weiss and D. S. Faber. “Field Effects in the CNS Play Functional Roles”. *Front Neural Circuits* 4 (2010). DOI: `10.3389/fncir.2010.00015`.

[199] D. A. Weitz et al. “Diffusing-Wave Spectroscopy: The Technique and Some Applications”. *Phys. Scr.* 1993.T49B (1993). DOI: `10.1088/0031-8949/1993/T49B/040`.

[200] R. Wiltschko. *Magnetic Orientation in Animals*. Springer Science & Business Media, 2012. ISBN: 978-3-642-79749-1.

[201] W. J. Wiscombe. “Improved Mie Scattering Algorithms”. *Appl. Opt., AO* 19.9 (1980). DOI: `10.1364/AO.19.001505`.

[202] G. M. Wittenberg and S. S.-H. Wang. “Malleability of Spike-Timing-Dependent Plasticity at the CA3–CA1 Synapse”. *J. Neurosci.* 26.24 (2006). DOI: `10.1523/JNEUROSCI.5388-05.2006`.

[203] Y. Yang et al. “Imaging Action Potential in Single Mammalian Neurons by Tracking the Accompanying Sub-Nanometer Mechanical Motion”. *ACS Nano* 12.5 (2018). DOI: `10.1021/acsnano.8b00867`.

[204] X.-C. Yao et al. “Cross-Polarized Reflected Light Measurement of Fast Optical Responses Associated with Neural Activation”. *Biophys J* 88.6 (2005). DOI: `10.1529/biophysj.104.052506`.

[205] T. Zemb and P. Lindner. *Neutrons, X-Rays and Light: Scattering Methods Applied to Soft Condensed Matter*. Elsevier, 2002. ISBN: 978-0-444-51122-5.

[206] L. I. Zhang et al. “A Critical Window for Cooperation and Competition among Developing Retinotectal Synapses”. *Nature* 395.6697 (1998). DOI: `10.1038/25665`.